



Norwegian University of
Science and Technology

Differentiation and Bone Deposition of Bone Marrow Derived Stem Cells on Additive Manufactured Porous Ti-6Al-4V Scaffolds

Timothy Jøraholmen

Master of Science in Mechanical Engineering

Submission date: June 2017

Supervisor: Jan Torgersen, MTP

Co-supervisor: Marita Westhrin, IKM

Norwegian University of Science and Technology
Department of Mechanical and Industrial Engineering

Acknowledgements

First and foremost, I would like to thank my Supervisor Professor Jan Torgersen and my Co-Supervisor Postdoc Marita Westhrin.

Jan, since the day I walked in to your office you have believed in me and urged me to go pursue my ideas. You have offered me tremendous support and your door has always been open when I needed it the most. You have given me the opportunity to bounce ideas off of you more than once, which is amazing given the tight schedule you keep. The directions you gave me during this work have been invaluable. Without your input I would not have been able to complete such an in-depth study.

Marita, during the months we have known each other you have always been supportive and incredibly patient. You have provided me with invaluable knowledge regarding everything from cell culturing to technical writing. You have literally taught me everything I know in the lab, in a record time! Thank you for the all the trust and countless hours you have put into to guiding a, formerly completely green, future mechanical engineer through a jungle of cell processes, theory and practise. Without you, most of this work would not have been possible. The input you provided during my writing has always been spot-on and really helpful.

I would like to thank Professor Therese Standal for supporting and believing in my project and for giving me the opportunity to work in the lab together with Marita. I know you are working on many projects and I'm grateful for having been given the chance to be part of one of them.

I also would like to thank my colleagues in the office, for always keeping an incredibly high work pressure throughout the year. We have been sitting together in the office for long hours and early mornings (maybe a little too often lately). Thanks for keeping a light atmosphere with a lot of fun activities during the all too few breaks. A big thanks also to all my friends. You have always managed to keep my mind on other topics, when i needed to unwind after long days and weeks.

I am grateful for everything my parents have given me. Either it be moral support during this stressful time, a helping hand when the account dried up or all the happy times we have spent together during my years on this earth. Mom and dad, you have always been there for me in good and bad. For that, I am sincerely thankful. Thank you Vivi, for always taking the time lately to read through and correct my, at times, incomprehensible English.

Last, but definitely not least, i would like to thank my Panda, ehm, I mean Kari for the amazing support and trust. It has been wonderful to get to know you and i can't wait to see what the future holds!

Abstract

The number of arthroplasty surgeries, or joint replacing surgeries, being performed each year is increasing worldwide. Younger patients are also being increasingly introduced to this kind of surgery, which means that the implants manufactured in the future need to last for an increased time span. Today, massive metal implants are commonly used. These are capable of causing an onset of stress shielding, lying at the basis of osteopenia: a painful condition where the bone in contact with the implant disappears, causing numerous costly and painful resurgeries.

By introducing additive manufacturing (AM) in the production of implants, porous structures can be manufactured thus lowering the stiffness characteristics of the implant. A factor that proves to reduce the onset of osteopenia.

Osteoblast precursors, i.e. bone marrow derived stromal cells (BMSCs), prove to be influenced by the surface roughness and porosity of the extracellular matrix. In fact, these cells can be influenced into osteoblast differentiation by the sole action of the surrounding implant structure. Having the knowledge on how surface topography induces cell fate is key to the fabrication of next generation implants.

In this Master's Thesis, the osteoconductive and the osteoinductive traits of additive manufactured Ti-6Al-4V porous structures was investigated. A porous scaffold design was developed and fabricated. The structures were then seeded with bone marrow derived mesenchymal stromal cells (BMSCs) to conduct a selection of *in vitro* studies. The seeded scaffolds were cultured in osteogenic medium (OM) and in non-osteogenic growth medium (GM) before the BMSC differentiation was assessed by a variety of experiments:

Adhesion of cells cultured in GM showed a widely spread cell morphology, when characterised by confocal microscopy. As expected, the amount of adhered cells seemed to increase over the course of 48 hours. Multiple alamarBlue® stainings, showed a BMSC activity increment within the first five days of culturing in OM. This trend was also observed by BMSCs cultured in GM, as the activity level caught up to the OM cultured cells by day 9. Alkaline phosphatase (ALP) staining at day 10 showed an extensive ALP expression by OM cultured cells and partial staining of GM cultured cells, suggesting the onset of BMSC differentiation into osteoblasts. Experiments using real-time PCR analysis showed a slight upregulation of RUNX2 and osteocalcin after 21 day of culture, possibly suggesting an onset of differentiation. Alizarin red stainings, provided indications of mineralisation for BMSCs cultured in both mediums, although more mineralisation was found in OM cultured cells. Scaffolds are found to have good osteoconductive properties, but moderate osteoinductive tendencies.

This study sets the foundation for understanding surface topography effects on BMSC differentiation in 3D porous scaffolds and might lead to a new area to be explored in future implant design.

Sammendrag

Hvert år øker antallet av utførte protesekirurgier verden over. Også yngre pasienter blir i økende grad introdusert til denne typen operasjon, noe som vil kreve en økt levetid av morgendagens implantater. De fleste ortopediske implantatene som er i bruk idag, blir produsert i massive metalllegeringer. Disse er i stand til å forårsake stressskjerming, som igjen ligger til grunn for osteopeni: en smertefull tilstand der beinmassen rundt protesen forsvinner og som videre fører til at mange pasienter trenger en kostbar gjenoperasjon.

Det å oppnå kunnskap om hvordan overflatestruktur inducerer celleprosesser er nøkkelen til utvikle neste generasjons implantater. Introduksjonen av additiv tilvirkning i produksjonen av ortopediske implantater baner vei for fremstillingen av porøse strukturer, noe som bidrar til å redusere implantatets stivhetskarakteristikker. Dette viser seg å redusere faren for tilgang til osteopeni.

Osteoblastforløpere, i.e. stromale beinmargceller, viser seg å bli påvirket av overflateruheten og porøsiteten til underlaget de fester seg på (ECM). Disse cellene kan faktisk bli påvirket til å begynne osteoblastdifferensieringen kun ved å tilrettelegge ECM ruheten. Ved å inkorporere slike egenskaper i fremtidige implantater, vil en potensielt forkorte rekonvalesenstiden for pasientene som mottar slike implantater.

I denne masteroppgaven ble de osteokonduktive og de osteoinduktive egenskapene til porøse, additivt tilvirkede, Ti-6Al-4V strukturer undersøkt. En porøs, trabekulær struktur ble utviklet og senere utsådde med stromale beinmargceller (BMSCer) for utførelsen av en serie *in vitro* studier. Skaffoldene ble dyrket i både osteogent medium (OM) og i ikke-osteogent vekstmedium (GM) før BMSC-differensieringen ble undersøkt ved en rekke eksperimenter:

Adhesjon av BMSCer dyrket i GM viste en bredt spredt cellemorfologi ved avbildning i konfokal mikroskop. Som forventet, så mengden celler ut til å øke i løpet av 48 timer dyrking. Gjentatte forsøk der cellene ble farget med alamarBlue®, viste en rask aktivitetsøkning iløpet av de fem første dagene for OM dyrkede celler. Aktivitetsnivået til GM dyrkede celler tok igjen aktivitetsnivået til OM dyrkede celler i løpet av dag ni. ALP-farging etter ti dagers dyrking viser et høy ALP konsentrasjon i OM-dyrkede celler og til dels også i GM-dyrkede celler, hvilket tydet på at BMSC-differensiering til osteoblaster var påbegynt. Eksperimenter ved bruk av sanntids PCR-analyse viste en økning i osterix og sclerostin ved dag 21 for OM-dyrkede celler, hvilket tydet på en moden osteogeneringsfase. For GM-dyrkede celler antydte en oppregulering av RUNX2 og osteocalcin ved dag 21 en begynnelse av differensiering. Avsluttende eksperimenter der alizarin rød ble brukt til å farge cellene gav faste bevis for mineralisering av BMSC'er dyrket i begge medium, selv om høyere grad av mineralisering ble funnet i OM dyrkede celler. Skaffoldene ble vurdert til inneha gode osteokonduktive egenskaper, men relativt lave tendenser til osteoinduktivitet.

Denne studien danner grunnlaget for å forstå innflytelsen til overflatetopografi på differensieringen av BMSCer dyrket i 3D skaffold. Dette vil muligens lede videre forskning inn på et nytt område, innen fremtidens utvikling av proteser.

Abbreviations and symbols

Symbol	=	definition
ARS	=	Alizarin red stain
BM	=	Basic medium
BMSC	=	Bone marrow derived mesenchymal stromal cell
CAD	=	Computer aided design
DEX	=	Dexamethasone
OM	=	Osteogenic medium
DMSO	=	Dimethyl sulfoxide (cell freezing medium)
DMP1	=	Dentin matrix acidic phosphoprotein 1
DPBS	=	Dulbeccos phosphate buffered saline
DPSCs	=	Dental pulp derived stromal cells
ELISA	=	Enzyme-linked immunosorbent assay
EB	=	Electron beam
ECM	=	Extracellular matrix
EIGA	=	Electrode induction melting gas atomization
EG	=	Electron gun
FA	=	Focal adhesion
FAK	=	Focal adhesion kinase
FBS	=	Foetal bovine serum
GARA	=	Garamycin
GLU	=	Glutamine
GM	=	Growth medium
HA	=	Hydroxyapatite
HBSS	=	Hanks' balanced salt solution
HEP	=	Heparin
HLA-DR	=	Human Leukocyte Antigen - antigen D Related
IL-1 β	=	Human interleukin
LAL	=	Limulus ameocyte lysate
MEM- α	=	Minimum Essential media Eagle
MSC	=	Mesenchymal stromal cell
NOM	=	Non osteogenic medium
OM	=	Osteogenic medium
PBF	=	Powder bed fusion
PBS	=	Phosphate buffer solution
PCR	=	Polymerase Chain Reaction
P#	=	Passage number
PL	=	Platelet lysate
PLA	=	Poly-lactic acid
RPMI	=	Roswell Park Memorial Institute media

RT	=	Room temperature
RUNX2	=	Runt-related transcription factor 2
SEM	=	Scanning electron microscope
SS	=	Stainless steel
TNF- α	=	Tumor necrosis factor alpha

Contents

Acknowledgements	iii
Abstract	v
Sammendrag	vii
Abbreviations and symbols	ix
Table of Contents	xiii
List of Tables	xv
List of Figures	xviii
1 Introduction	1
1.1 Biomedical background	2
1.1.1 Implants	4
1.1.2 Specific cell processes	6
1.1.3 BMSCs	9
1.2 Platelet lysate	10
1.2.1 Biomedical challenges	10
1.3 Mechanical background	13
1.3.1 Selective laser melting (SLM)	13
1.3.2 Electron beam melting (EBM)	13
1.3.3 Production and characteristics of PBF powders	14
1.3.4 SLM and EBM post print material characteristics	15
1.3.5 SLM and EBM process related challenges	16
1.4 Topology optimisation	18
1.5 State of the art	20
1.5.1 2D scaffolds	21
1.5.2 3D scaffolds	21
1.5.3 Main challenges	23

2	Aim of the thesis	25
2.1	Outline	25
2.2	Previous work	26
3	Experimental methods	27
3.1	Scaffold design and manufacturing	27
3.1.1	Experimental	27
3.2	LAL and cleaning procedure	31
3.2.1	Experimental	31
3.3	Mediums and BMSCs preparations	31
3.3.1	Experimental	32
3.4	Confocal microscopy and adhesion	32
3.4.1	Experimental	34
3.5	AlamarBlue® and BMSC activity	34
3.5.1	Experimental	34
3.6	ALP staining	35
3.6.1	Experimental	35
3.7	PCR analysis	36
3.7.1	Experimental	36
3.8	Alizarin red staining (ARS)	37
4	Results	39
4.1	Scaffold characteristics	39
4.1.1	Surface characteristics	39
4.1.2	Mechanical characteristics	39
4.2	Adhesion	41
4.3	BMSC activity over the course of 9 days	44
4.4	ALP expression	44
4.5	PCR analysis	44
4.5.1	Generally higher gene expression for 2D cultured cells	48
4.6	Calcium deposition	50
5	Discussion	55
5.1	Osteoconductivity of structures	55
5.2	Osteoinductive traits of scaffolds	58
5.3	Challenges	60
5.3.1	Geometrical considerations	61
5.3.2	Large porosity dimensions	61
5.3.3	Consistency of seeding	61
5.3.4	Computer capacity and scaffold design	62
5.3.5	Reliability of compression results	62
5.3.6	Microscopy challenges	63
5.4	Future work	64

6	Conclusions	65
	Bibliography	67
	Appendix A - Articles	I
.1	Scandinavian society for biomaterials- (SCSB-) abstract submission	I
.2	SCSB poster	V
.3	CIRP manuscript	IX
	Appendix B - Procedures and extra forms	XVII
.4	PCR amplification and run-outs	XIX
.5	Automatically generated FEA report of static compression analysis.	XXIII
.6	Risk assessment	XXXIII

List of Tables

1.1	AM processes	12
3.1	EBM settings	29
3.2	FEA settings	30
3.3	PCR amplification cycle	37
4.1	RNA concentrations	48

List of Figures

1.1	Currently available AM implants	3
1.2	The bone remodelling process	4
1.3	Total knee arthroplasty	5
1.4	The osteointegration process	6
1.5	Cell's focal adhesion	7
1.6	Cell's proliferation	8
1.7	BMSC differentiation lineages	9
1.8	Stress shielding	11
1.9	The SLM and EBM machines	14
1.10	PBF process limitations	19
1.11	Force propagation in lattices	20
3.1	Tilted lattice	28
3.2	3D porous scaffold geometry	28
3.3	Compression test	30
3.4	The confocal microscopy principle	33
4.1	Surface characterisation by SEM	40
4.2	Grains close-up	41
4.3	FEA static compression setup	42
4.4	Young's modulus of the scaffolds	42
4.5	Surface contact area reduction	43
4.6	8 h and 16 h adhesion results	45
4.7	24 h and 48 h adhesion results	46
4.8	alamarBlue® results	47
4.9	ALP staining	47
4.10	Collagen type 1 expression	49
4.11	Runt related transcription factor 2 expression	50
4.12	Osteocalcin expression	51
4.13	Osterix expression	51
4.14	Sclerostin expression	52

LIST OF FIGURES

4.15 Alizarin red 53

5.1 In-focus range during microscopy 63

5.2 Proposed compression test scaffolds 64

Introduction

Total arthroplasty, or joint replacing surgery, is one of the most successful surgical intervention performed today. Implants are used as joint substitutes, relieving patients of pain further enabling them to resume a normal life style. In 2003, 220 000 arthroplasties were performed in the United States (Lee and Goodman (2008)), almost the same number of arthroplasties were performed in the United Kingdom alone during 2015 according to the National Joint Registry (NJR) (NJR 2016). This number is expected to increase over the next years, as the expected lifetime of the general population is increasing. It is estimated that by 2030 over 500 000 of these kind of interventions will be performed in USA each year. Over the last years this number is increasing steadily also in the U.K., a trend observed also for other kind of implants, as described by Williams SN (2015).

We live in an era of extremes where obesity/overweight is at an all-time high and, at the same time, a large part of the population is over-exercising. These factors increase the strain applied to our joints which, over time, will lead to an increasing rate of joint replacements. Salih et. al. (2013) studied the relationship between obesity and success rate of total knee arthroplasties and concluded that higher risk of complications post-operation and premature implant failure is associated with arthroplasties performed in overweight patients. The average knee and hip implant today has a lifespan of 12 years (NJR (2016)) before revision or replacement surgery is needed. This was a reasonable mechanical lifetime earlier, when the majority of patients receiving these implants were among the older generations, having a remaining life expectancy often lower than these figures. Younger generations are introduced to these types of surgeries at an increasing rate and the mean time to failure (MTTF) for these implants needs to be expanded to fulfill the requirements of the users. The data from the NJR, also show an increased risk for resurgeries among the younger patients (under 55 years). Introducing implants with an extended MTTF will save society for enormous expenses associated with revisions and resurgeries. From the patient perspective this will lower experienced pain, increase life quality and minimise time spent in care facilities. Progress in this field is urgently needed, as the potential savings and prevention of discomfort are enormous.

Evidence can be found proving that for centuries orthopaedic surgeons have tried to find ways of relieving pain and restoring mobility to their patient's affected joints. This being said, we only need to look back 70 years to find the first reliable arthroplasty implants finding their ways to the surgical tables (Trebše and Miheli (2012)). These were often surgically installed using a cementing method, which is still widely used today. Since the fifties, however, many advances have been

made in orthopaedic field, seeing the emergence of porous, non-cemented implants. These are placed in direct contact with living bone, where the patient's inherent bone regeneration process will integrate the implant by generating bony material onto the implant surfaces.

In later years, the biomedical field has branched out and created a new field commonly referred to as *tissue engineering*; where a combination of cell studies, bacterial research, classical engineering, material science and manufacturing methods are studied in order to produce scaffolds able to support the culturing of biological tissues. In this field, many studies have been conducted aimed at investigating the cell processes leading to bone formation.

A promising manufacturing field currently being introduced to the biomaterial field, is additive (layer-)manufacturing (AM). A common term for a variety of different building processes performed in apposite machines, utilising one or more out of a variety of materials (Tran et al. (2017)). Almost four decades ago, this technology was introduced as a revolutionary manufacturing technology (Levy et al. (2003)). Since then, it has opened the doors to a whole new series of possibilities regarding the design of complex, customised parts, leading companies to rethink the way they develop their products. As the name suggests, the technology manufactures components using a layer based approach. This results in an efficient manufacturing method from a material perspective, as less material is wasted with respect to conventional manufacturing methods. Since less (or none) subtractive post-processing is needed in AM, the manufacturing of components in expensive and difficult-to-form materials is possible. The increased geometrical flexibility with regards to the manufacturing of complex (internal) geometries is directly the result of the employment of this layer based technique.

By implementing AM in tissue engineering, scaffolds with increasing complexity, resembling biological structures and having high geometrical tolerances can be manufactured. Scientists are hence enabled to study *in vitro* how cells function in an environment resembling the specific *in-vivo* conditions of joint implants. In the biomedical industry, AM is currently being used to produce different implants, which require a high degree of customisation (Figure 1.1). By combining AM with the knowledge gathered in the laboratory by different biological studies, it is believed that a new generation of better implants can be developed. Some *in vivo* studies have been conducted where different AM porous materials have been implanted into humans and animals with varying results (Sidambe (2014)). The surface properties and their effect on the biological processes following surgery is still a debated field.

1.1 Biomedical background

Bone is a highly active tissue consisting of 35% organic components such as collagen, γ -carboxyl-glutamic acid-rich protein, osteocalcin, lipids, proteoglycans and glycosaminoglycans. The remaining 65% are composed of inorganic connections mainly in the form of hydroxyapatite crystals (Martin et al. (1988)).

As in all vertebrates, the human skeleton forms a rigid structure responsible for carrying the body and protecting internal organs, in addition to serving as a storage facility for minerals such as calcium, sodium and magnesium. These tissues are continuously being replaced in adulthood by a process known as endochondral ossification, or bone remodelling (Martin et al. (1988, 2013)). Figure 1.2, provides a graphical overview. Two main constituents carry out this process, namely



Figure 1.1: Currently available AM implants

Pictures depicting a jaw implant from LayerWise ¹(left) and a cranial implant by Arcam ¹ (right), both manufactured using AM.

the osteoclast responsible for the process of resorption (removing old bone material), and the osteoblasts responsible for the deposition of new bone material (osteoid).

Bone resorption results in the formation of resorption pits which, as the name suggests, are small cavities on the bone surface generated by the removal of old bone. In a healthy person, these resorption pits immediately see the appearance of bone marrow derived mesenchymal stromal cells (BMSCs) which will differentiate into mature osteoblasts and begin the process of depositing osteoid, thus filling the resorption pits with new bone material. During the bone remodelling process, osteoblasts may become enclosed in the newly formed bone differentiating into osteocytes. Other cells may undergo apoptosis (a form of programmed cell death), or become bone lining cells. Osteocytes will communicate with each other, with osteoblasts, osteoclasts, bone lining cells and other cells through complex series of micro processes in the canaliculae of the bone (small passage ways or channels inherent in bones). Osteocytes are placed in the bone at locations which are ideal in order for them to respond to mechanical loads input. It is believed that they are responsible for controlling the bone remodelling processes (Martin et al. (2013); Bayliss et al. (2012)). Bone lining cells lose their ability to synthesise osteoid, becoming flattened and having limited cytoplasm. These are basically acting as a thin film separating the bone from the bone marrow and from the action of osteoclasts (Martin et al. (1988)).

Julius Wolff, among others, realised by 1892 a connection between the strength of bones and the input mechanical forces. Bone strength increases with an increased loading. Reciprocally, a lower mechanical loading will result in less bone strength (Frost (2004)).

¹<http://www.zmescience.com/research/studies/3d-printed-titanium-jaw-replaced-30755/>
<http://www.arcam.com/solutions/orthopedic-implants/>, both accessed: 04.06.2017

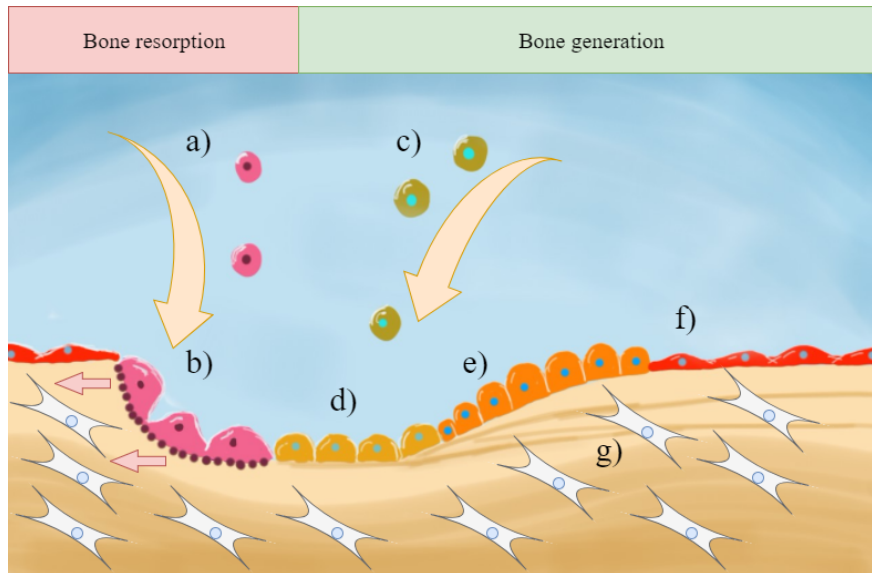


Figure 1.2: The bone remodelling process

Osteoclast precursors (a) arrive at the resorption site and differentiate to mature osteoclasts (b), before starting the bone resorption process. Simultaneously, osteoblast precursors such as BMSCs (c) arrive at the same site and differentiate to pre-osteoblasts (d) before becoming mature osteoblasts (e) finally starting the bone deposition. When their duty is fulfilled they end up either becoming bone lining cells (f) or enclosed osteocytes (g). The process moves towards the left of the image (pink arrows).

1.1.1 Implants

Normally, when injuries occur, the body responds immediately to repair the damages. a large standard deviation among duplicates or by the failed expression of the gene itself. If the bone damage is small the body is able to heal itself, using either direct or indirect bone-healing (Little et al. (2011)). Direct healing refers to the direct deposition of osteoid in the injured area, occurring only if no strain is applied post-injury. If, however, strain and micromovements are present in the injured zone, indirect bone healing occurs where a fracture callus is formed prior to the formation of osteoid. The fracture callus is a heterogenous tissue consisting of woven bone produced by osteoblasts and cartilage produced by fibroblasts. In fractures where the damage magnitude is too large for self healing, or if the patient has a medical condition like osteoporosis or arthritis, an implant is needed.

Osteoarthritis is a joint disease connected to the breakdown of cartilage between joints. The increased friction generated when bone to bone contact occurs causes swelling, pain and mobility restrictions. By the use of specific implants, mobility and loading of affected joints may be regained together with a substantial reduction in pain.

Medical implants are defined as products used for medical purposes in patients, in connection with diagnosis and/or treatment (van Eck et al. (2009)). in today's market today one can find a large variety of implants, ranging from cosmetic products to osteointegrating joint replacements. The most commonly used implants are the fragment implants such as wires, nails, pins, screws, plates and other instruments needed for orthopaedic surgery. These are often used to fixate bone fragments to allow the onset of direct bone healing. Joint replacing implants are larger mechanical

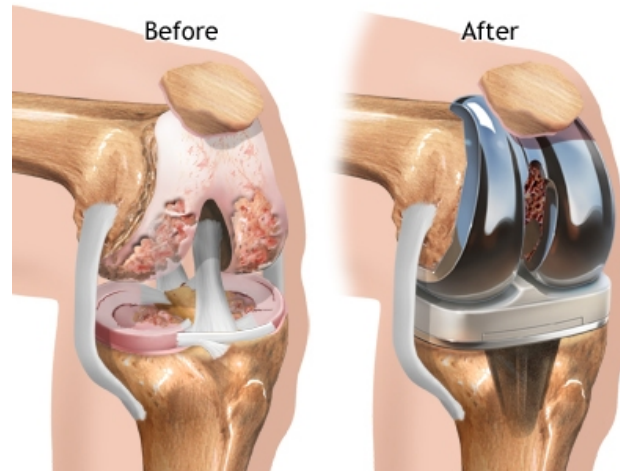


Figure 1.3: Total knee arthroplasty

Image depicting a knee before and after a total knee arthroplasty².

joints that are able to help the patient regain mobility and loading of a worn out or injured joint. The latter implant family comprise implants such as, e.g., knee implants and hip implants. These are also referred to as arthroplasty implants, deriving from the name of the surgical procedure used to fit them. As such, we have the *total knee arthroplasty*; where the knee joint is completely remodeled (Figure 1.3).

The U.S. Food and Drug administration (FDA) classifies implants in three categories, where orthopaedic implants are found under class-II, Special control (FDA (2016)). The classification is based on the intended use of the medical product, with special regards to the use-associated risks. Class II are not subject to pre-market approval applications, as orthopaedic implants have already been classified. A 510k application may however be needed, giving the FDA 90 days to classify the product before its market introduction.

After an arthroplasty surgery in the case of non-cemented implants, migratory BMSCs are immediately recruited to the surgical site. These cells will differentiate into osteoblasts thanks to the activation of adhesion and proliferation phases. This enables the bone deposition process (Naddeo et al. (2015)). This osteoid deposition taking place on the implant surface is comparable to the last part of the endochondral ossification process, where osteoblasts are induced to produce osteoid. The formation of interlocking bone, in the micro-spacing between the pre-existing skeletal structures and the newly introduced implant, is paramount to achieve an abundant mechanical fixation and is commonly termed osteointegration (Figure 1.4). Initially defined by Albrektsson et al. (1981) as *direct contact between living bone and implant*, osteointegration is paramount in the successful outcome of an implant surgery. In order to ensure direct bone deposition without callous formation it is imperative to avoid micro movements between the implant and the bone. Callous formation in the *bone-to-implant* interface is unwanted during this phase of osteointegration (Albrektsson et al. (1981)).

If the implant material is capable of promoting the differentiation of BMSCs, the bone implant integration time will decrease, allowing for a swift patient recovery. Such an osteointegrative-

²<http://www.jointimplantsurgeons.com/knee-replacement/> accessed 04.06.2017

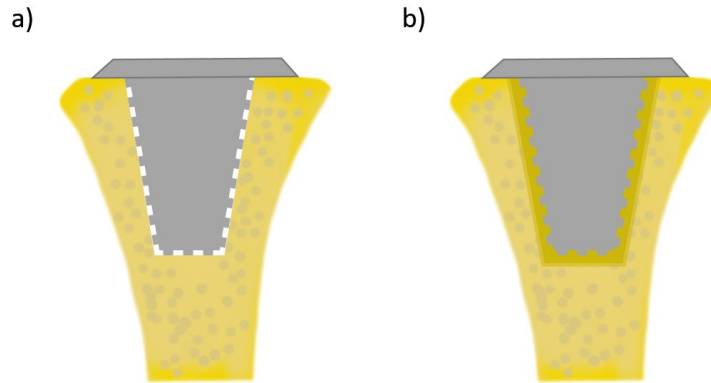


Figure 1.4: The osteointegration process

An implant (grey) right after surgery (a), and after a longer time period (b). Notice how the bone (yellow) grows inside of the implant's surface topography, creating mechanical interlocking. This bone growth is enabled by bone generating cells, i.e. osteoblasts.

promoting factor is dependent on two implant related properties; namely osteoconduction and osteoinduction. According to the definition provided by Albrektsson and Johansson (2001), osteoconduction represents the implant material's ability to support biological activity in the form of bone in-growth on the surface. This is closely related to the material qualities such as toxicity, or biocompatibility. Osteoinduction refers to the process in which the material is capable to stimulate BMSCs to differentiate into osteoblasts.

1.1.2 Specific cell processes

In the field of tissue engineering, scaffolds acting as extracellular matrices (ECMs) are being manufactured to study specific cellular processes in *in vivo*-like conditions. ECMs are here defined as structures that are structurally and chemically able to support cellular processes. In the human body, ECMs are generated by materials secreted by the cells themselves, such as bone.

Once surgically installed, orthopaedic implants act as ECMs for the BMSCs arriving at the surgical site. The implant's osteoconductive and osteoinductive properties will vary with different surface morphologies. Researchers are therefore seeding BMSCs on small scaffolds having similar morphologies as potential implants, enabling them to study the cells response. An understanding of the workings for each stage in the cellular development is imperative in this respect and will be given in the next sections.

Adhesion

The generation of focal adhesion complexes (FAs), commonly referred to as adhesion, is among the first processes to take place once adherent cells such as BMSCs are seeded onto an ECM. Two main FA-types exist, namely cell-to-cell and cell-to-substrate adhesions. The latter are basically contact points between the ventral part of the cell's actin-based cytoskeleton and the ECM. This contact is mediated through integrin receptors inherent in the cells.

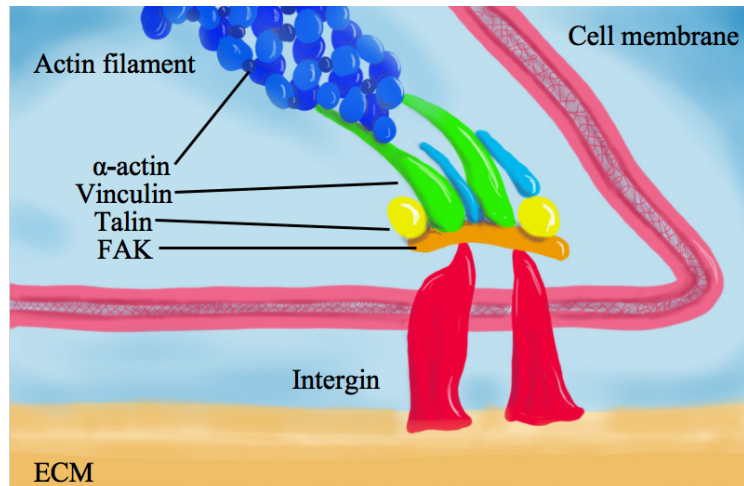


Figure 1.5: Cell's focal adhesion

Integrins (red) form the transmembrane connection to the ECM. These are further connected to the actin cytoskeleton by the action of adaptor proteins, such as vinculin (green) and α -actin (dark blue dots).

Integrins can be described as adhesive molecules and constitutes a family of receptors capable of mediating cell adhesions to fibronectin, laminin and collagen. Integrins are trans-membrane proteins and form a functional extension of the cell's actin cytoskeleton network, thus creating *cell anchoring junctions* to the ECM.

Adaptor proteins, such as e.g. vinculin, and α -actin, form a *actin-to-integrin* transition connection (Lock et al. (2008)). Focal adhesion kinase (FAK), a type of cytoplasmic tyrosine kinase, is important for integrin-mediated signal transduction and play an important role in cellular processes. Figure 1.5 attempts to give a simplified overview of an FA-complex to an ECM.

Geiger et al. (2009) found that a balance between two main factors is influencing the resulting FA type, namely the surface properties and the cell's own sensory capability. Especially the surface chemistry seems to influence the integrin composition. Mechanical perturbations in existing integrins and cytoskeletons seem to promote both the generation of more FAs and to initiate signalling cascades influencing a variety of cell processes. These claims are also supported by Wozniak et al. (2004), who proposes that cells respond to diverse biochemical and physical inputs, provided by the chemical assembly of the focal adhesion in contact with the material. The exact combination of factors will therefore influence the adhesion, proliferation, shape, migration, polarisation and fate of the cells. Cell migration, or *motility*, can be defined as the cells ability to randomly or actively move on top of underlying ECM; a process that is regulated by the surface characteristics, such as topography and chemistry. Integrins have evolved to provide the mechanism for this motility.

Proliferation

Once cells have adhered to the ECM, the proliferative process can initiate. This process is constituted by a growth phase and a division phase, following the natural cell cycle. The previously mentioned integrins play a main role in regulating the proliferation, along with mechanical and chemical signals provided by the ECM (Gattazzo et al. (2014), Schlie-Wolter et al. (2013)). In

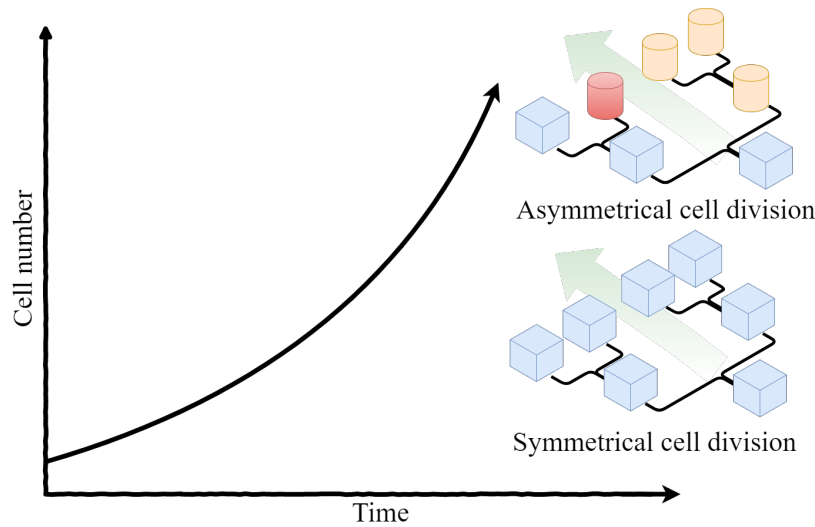


Figure 1.6: Cell's Proliferation

Simplified representation of the proliferation process and its types. Over time, the cell number will expand by cell proliferation (graph). The division of stem cells may happen symmetrically (bottom right) where one stem cell (blue) divides into two new stem cells, or asymmetrically (top right), where one stem cell divides in a new stem cell in addition to either a more specialised cell (orange) or a progenitor cell (red).

most tissues, different cell types are designated to proliferate, for instance stem cells: These can proliferate both symmetrically, generating two new stem cells, and asymmetrically, generating both a new stem cell and a cell with a predefined cell fate such as progenitor cells. Progenitor cells such as osteoblast progenitors, are more specialised cells which may not necessarily proliferate further. They will however end up differentiating towards a final cell function, such as osteoblasts. At the final differentiation stage, some cells lose their capability to proliferate. Figure 1.6 provides a graphical explanation of the proliferation process.

Differentiation

Differentiation is the process where the cells get altered to perform a more specialised function. In an organism, the *gene-regulatory network* is in charge of controlling the differentiation, using both cell signaling and growth factors. The cell signaling mechanism works through signal transduction factors where a ligand originating from a cell, binds to a receptor on the cell to be differentiated, inducing conformational change of the receptor. After a cascade reaction and enzymatic function, an onset of transcription factors lead to differentiation.

Through differentiation, the function of the cells gets altered along with their genetic expression. In the laboratory, the monitoring of secreted proteins and transcription factors are used to determine the state in which the cells are at a given time. The combination of a variety of transcription factors will decide which genes the cell expresses.

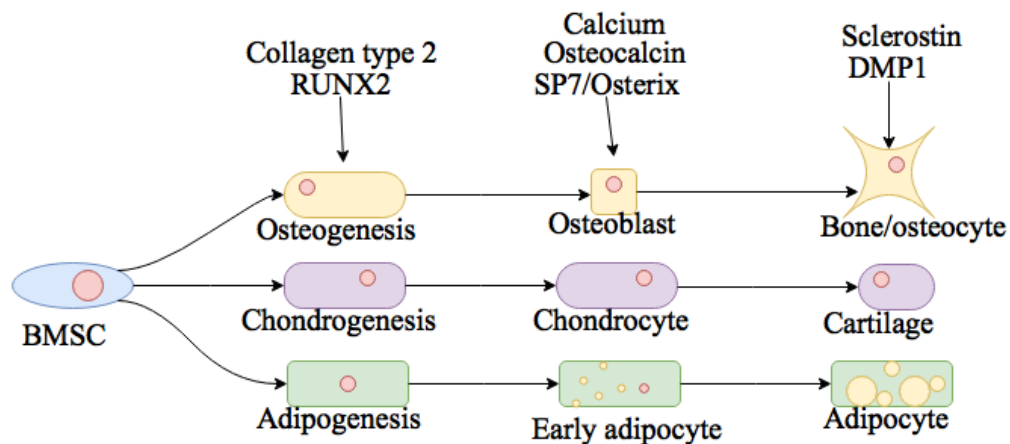


Figure 1.7: BMSC differentiation lineages

Overview of the potential differentiation lineages of BMSCs. This thesis focuses on the osteogenic lineage (first lineage). The genes and expressed at different stages of the osteogenic lineage are placed above their respective time point. The mineral calcium is also reported due to its characteristic expression during bone formation. The expression of Sclerostin at the assigned time point is still being debated.

1.1.3 BMSCs

As there are many different cells in the body with varying characteristics, the focus of this study will be on bone marrow derived mesenchymal stromal cells (BMSCs).

Formerly, these cells were known as mesenchymal stem cells or bone marrow stem cells, but due to their inability to perform certain processes attributed to stemness e.g. complete lineage renewal, the new name description was recently introduced. Officially formalised as multipotent mesenchymal stromal cells in Horwitz et al. (2005), the minimal criteria for defining such cells were defined in Dominici et al. (2006) and consist of a variety of characteristics, mainly:

- The ability to be plastic-adherent under standard culturing conditions.
- The *in vitro* tri-lineage (multipotent) ability, thus being capable to differentiate into chondroblasts (cartilage-generating cells), adipocytes (fat cells) and in our case, the former mentioned osteoblasts. See Figure 1.7 for lineage specification.
- The positive expression of genes CD105, CD73, CD90 and the negative expression of CD45, CD34, CD14, CD19 and HLA-DR (Human Leukocyte Antigen - antigen D Related).

In order to assess osteoblast differentiation *in vitro*, a gene-monitoring combination of Osterix (SP7), runt-related transcription factor 2 (RUNX2), osteocalcin, Collagen type I (COL1), dentin matrix acidic phosphoprotein 1 (DMP1) and Sclerostin may be used. Figure 1.7 provides an overview on where in the differentiation process one can expect an elevated expression onset of the individual genes.

The function of the different monitored genes is still being debated. However, at this point the SP7/Osterix gene is widely associated with cell differentiation into osteoblast. The RUNX2 gene seems to control the early osteoblast differentiation and is also acting as an osteoblast marker. RUNX2 is also a factor in the transactivation of osteocalcin, a gene found in mature osteoblasts. COL1 is found in the osteoid deposited by osteoblasts and is further associated with enhanced bone-deposition (Huang et al. (2007); Chiu et al. (2014)). DMP1 is mainly found osteocytes.

To assess the presence of mature active osteoblasts, the *alizarin-red assay* can be performed. This is an assay which measures the calcium deposition secreted by osteoblasts.

1.2 Platelet lysate

Today, in tissue engineering and in the field of biomaterials, foetal bovine serum (FBS) is the main growth factor being used for cell culturing. For patients receiving some of these cell cultures, the use of FBS poses unwanted risks in regard to immune reactions and animal-to-human transmitted diseases. As the name suggests, FBS is collected from bovine fetuses (potentially causing unnecessary suffering to the calves). New alternatives to FBS are currently being researched.

The articles from Jonsdottir-Buch et al. (2013) and Jonsdottir-Buch et al. (2015) both provide an extended review on the uses of platelet lysate as a substitute to FBS. To summarise: Platelets are small cells without nucleus that circulate in the blood stream for a limited amount of time (7-10 d) before being replaced. Two of their main functions are to contribute to wound healing and to secrete growth factors. Platelets are also among the blood transfusion components and are at shortage in blood banks all over the world, as scarce amounts of blood is donated. Prior to expiry, they are stored at 22 °C, a temperature ideal for the proliferation of bacteria originating from the skin tissues during transfusion. Although different disinfection protocols have been implemented to limit the transmission of bacteria, there is still a certain risk level for contamination. As a consequence, the platelets have a shelf life of 5-7 d. Once the platelets reach expiry date, they are usually discarded, although having been produced by high standards. This is leading to large amounts of valuable platelets, still rich in growth-factors, never being used.

By lysing the platelets, growth factors and other components can be harvested. This platelet lysate (PL) is nowadays increasingly being used for ex-vivo cell-cultures as an alternative serum to FBS. The use of PL in cell cultures destined for human use is still a debated field, since the transfusion of infectious diseases may pose a risk.

Prins et al. (2009) compared the bone forming capacity of BMSCs cultured with PL or FBS *in vitro*. Cells cultured in PL show a sustained trilineage potency, as previously presented in subsection 1.1.3 and finally an increased *in vivo* bone formation capacity compared with cells cultured in FBS. Platelet lysate as a substitute to FBS is therefore a reliable alternative to FBS, when culturing BMSCs.

1.2.1 Biomedical challenges

Today, the main causes of resurgeries in the domain of hip and knee joint implants are: Aseptic loosening, pain, osteolysis and wear/instability (NJR (2016)). Okshevsky et al. (2015) and Chan

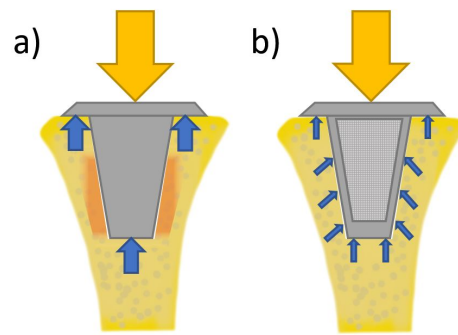


Figure 1.8: Stress shielding

A massive implant (grey, a) will take up most of the mechanical loading (orange arrow), transmitting these only to specific points in the bone (blue reaction forces). This will create partially unloaded zones (red). These unloaded zones may experience a natural onset of bone resorption. An implant having internal structures (b) will have a lower elastic modulus, thus leading to more implant deformation during loading. The implant will transfer a more evenly distributed load to the surrounding bone, hence possibly avoiding the onset of bone resorption.

et al. (2017) study bacterial onset and biofilm control. These are examples of work being performed to improve the success rate of arthroplasties.

Current biomaterials need to express material properties such as long fatigue life and a low Young's modulus, which is a tough combination. If low corrosion characteristics and high cytocompatibility are added to the mix, only a few materials will be able to partially cover these criterias. Stainless steel 316L, CoCr and specific titanium alloys being some of them, but still some qualities are not fulfilled.

As most metallic implants are still being manufactured from massive bulk materials, various challenges emerge. Some challenges are connected to the high elastic moduli inherent in these materials. Medical grade Ti-6Al-4V has a modulus of 110 GPa which is a lot when compared to human bone, having elastic moduli varying from 0.02 GPa to 30 GPa (Rho et al. (1993)). This difference gives rise to phenomena such as *stress shielding*, where the massive implant absorbs a larger share of the mechanical loading during the patient's daily activities. As a result, the bone around the implant is partially unloaded, hence leading to a natural onset of bone resorption. This is a contributing factor to osteopenia, or lysis (Wang et al. (2016a,b)). Figure 1.8 explains the stress shielding phenomena graphically.

By developing implants with elastic moduli resembling those of trabecular bone (~ 1 GPa) or cortical bone (~ 16 GPa), the stress shielding phenomena can be avoided. This would result in the reduction of pain and in a diminished need for resurgeries. Having implants with the same stiffness characteristics as the surrounding bone proves beneficial also according to Bugbee et al. (1997). This brings us to the next section concerning the methods that may be capable to create such implants (Murr (2016)).

Table 1.1: AM processes

Overview of main AM processes used today, sorted categorically with respect to building-strategies employed. Available materials for each process is changing rapidly, as more materials are developed for use in specific machines at a steady pace.

Building strategy	Technology	Materials	Fusing source	Strengths and weaknesses
Powder Bed Fusion	Selective Laser Sintering (SLS)	Atomised metal powder, ceramic powder and polymers	High power laser beam	<ul style="list-style-type: none"> + Fully dense parts + Accuracy and details + Strength and stiffness + Recycling potential - Supports are of same material as base structure - Closed geometries need to be fully dense - Costs
	Direct Metal Laser Sintering (DMLS)			
	Selective Laser Melting (SLM)			
	Electron Beam Melting (EBM)		Electron beam	
Directed Energy Deposition	Laser Engineered Net Shaping (LENS)	Metal powders (can also be atomised)	Laser beam	<ul style="list-style-type: none"> + Component and part repair + Combination of materials - Surface finish
	Electronic Beam Welding (EBW)			
Binder Jetting	Indirect Inkjet Printing (B3DP)	Polymer-, ceramic- and metal powders	Thermal energy	<ul style="list-style-type: none"> + Multicolor parts + Many materials available - Requires post-curing - Porosity
Material Jetting	Polyjet Printing	Photopolymers and waxes	Thermal energy and light	<ul style="list-style-type: none"> + Multiple materials and Surface finish - Low strength
Extrusion-based	Fused Deposition Modelling (FDM)	Thermoplastics, Ceramics, different mixtures and metals	Thermal energy	<ul style="list-style-type: none"> + Many materials available + Inexpensive machine - Resolution and Surface finish
	Contour Crafting			
Vat Photopolymerisation	Stereolithography (SLA) (2-photon or more)	Photopolymers and ceramics	UV laser	<ul style="list-style-type: none"> + Build speed and High resolution - Overcuring and High cost
Sheet lamination	Laminated Object Manufacturing (LOM)	Metallic sheets, plastic- and ceramic films	Laser	<ul style="list-style-type: none"> + Surface finish + Low cost - Part separation issues

1.3 Mechanical background

As mentioned earlier, various AM processes and machines have been developed since the field's introduction in the late seventies. An overview over the main processes is available in Table 1.1.

In order to better understand the AM philosophy, one can look at how different insects and other biological species in nature implement varying building strategies. Honeybees are such an example, since they construct their nest using a strategy closely related to AM, i.e. by secreting a wax-like substance and then depositing it in carefully selected spots. In this way, they are able to generate a honeycomb structure where they later deposit honey. During the past decades, honeycomb structures have found their application in several engineering applications due to their high stiffness-to-weight ratio (Wahl et al. (2012)). Honeycomb is furthermore a prime example of an internal structure easily obtainable by most AM processes.

1.3.1 Selective laser melting (SLM)

One of the earliest AM processes invented is commonly known as selective laser melting (SLM) (Table 1.1). This process is capable to operate with biomaterials such as Ti-6Al-4V, which is widely applied to custom implants. The SLM principle is based on an AM strategy known as powder bed fusion (PBF) which, as the name suggests, consists of a powder bed and a scanning laser. A fine grained metal powder, also known as feedstock, is deposited by a roller over a build platform at a layer thickness of several powder grains. The build platform, which usually maintains a temperature of roughly 90 °C, forms a basis onto which the final component is manufactured on and adhered to.

A focused laser beam with a specific power is then scanned over the build area at a preset speed. By doing so, the area of powder being scanned melts to a depth of more than one layer height and subsequently cools down rapidly, thus forming a solid cross-section of the component at the specific layer height. This layer fuses to the underlying layer. At the end of the scan, the build plate is lowered by one layer height and a new cycle begins. Layer after layer, the component is built, strictly following the pre-designed geometries exported from a 3D computer aided design (CAD-) model (Murr et al. (2012a)). Figure 1.9 (left) explains this process.

1.3.2 Electron beam melting (EBM)

Another process based on PBF, capable of manufacturing components in medical grade metals is commonly referred to as electron beam melting (EBM). At a first glance, this process (Figure 1.9, right) is quite similar to the previously presented SLM process, as both are characterised by the fusion of powders on a build plate. The main distinctions emerge when looking at the energy source which, in the case of EBM, is based on an electron gun. As with all machines involving the use of controlled electron-beams, the process is conducted in at a vacuum state of 10^{-4} Torr, enabling the accurate directionality of the beam. Another positive outcome of having a vacuum, is the elimination of oxidation onset, as minimal quantities of O₂ are present. Due to the poor heat conduction of vacuum, the build chamber atmosphere is usually supplied with helium to a pressure of 10^{-2} Torr, thus enabling heat conduction.

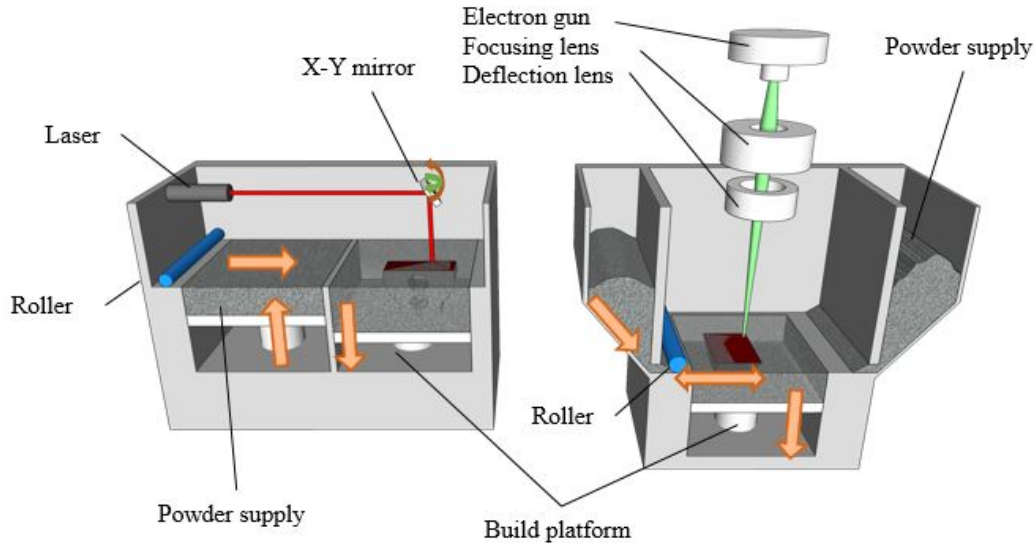


Figure 1.9: The SLM and EBM machines

Left: An SLM process is presented. The laser (red) is scanned by the X-Y mirror, onto the powder bed. A roller distributes the powder from the powder supply onto the build plate. The whole process is performed within an inert atmosphere, with an inert gas constantly flowing into the build chamber. Right: An EBM process is presented. Powder from the containers flows to the roller which distributes it over the build platform. An electron beam (green) originating from the electron gun is deflected towards a specific X-Y coordinate. A focusing lens concentrates the beam on a focal point thus melting the powder. The whole process is conducted in vacuum, with a weak pressure of an inert gas. The arrows indicate the movement of components.

1.3.3 Production and characteristics of PBF powders

The powders used in AM machines such as SLM and EBM ought to combine good relative packing characteristics, ensuring a dense layer empty of voids. Powders should also express easy flow geometries, thus enabling the powder grains to slide over and around each other ensuring homogeneous distributions when a new layer is distributed. Irregular grains and geometries result in poor flow characteristics and packing, which will lead to compromise the final material quality. In order to get best packing and flow characteristics, spherical grains with a varying diametrical distribution are preferred (Herzog et al. (2016)). Murr et al. (2012b) also mentions, among others, Van der Waal forces, cohesive forces and electrostatic forces as being relevant factors in determining the flow properties. In order to produce good quality feedstock powders, processes like atomisation, spherodisation, vacuum induction melting or electrode induction melting gas atomisation (EIGA) are used. Each of these processes have different qualities, lending themselves to the production of powders in varieties of materials (Murr et al. (2012a); Herzog et al. (2016)). The resulting products are fine powders with grain size ranging between 2 μm up to 150 μm . Once the powders are manufactured, a combination of different gratings are used to differentiate the powders into different size ranges. For the SLM process the preferred average particle sizes are in the range of e.g. 45 μm .

1.3.4 SLM and EBM post print material characteristics

The AM processes are characterised by both rapid melting and solidification of the feedstock material. This synergistic effect causes the formation of unique material microstructures in the final components, microstructures that lie at the basis of some unique mechanical characteristics.

Although dependent on the individual process parameters used, scan lines are usually easily distinguishable for SLM materials, maybe with the exception of titanium. Small grain sizes constituting larger parts of these materials are generated by the huge temperature gradients inherent in the process. As the grains are not granted enough high temperature growth time, they remain small and are therefore not able to grow between the layers of the print. Anyhow, SLM version of e.g. Ti-Al6-4V, CoCr and steels, often have more desirable material characteristics than their cast counterpart (Gibson et al. (2010), p.113).

In both Murr et al. (2012a); Murr (2016), different materials available for use in AM are presented and intrinsic material properties are discussed. Of particular interest is Murr et al. (2012b), where different microstructures typically achieved by SLM and EBM are presented, together with strategies for obtaining these. Hardness seems affected by the build direction, where the hardest surfaces are found in the direction of the build planes.

Sun et al. (2016b) investigates build rate optimisation and the achieved microstructures for 316L stainless steel (SS). The main microstructures and phases present in the builds are very complex and grains with different orientations are to be found inside the same build tracks, probably due to the continuous remelting. The different heat directions causes grains to also grow with different orientations. Face centered cubic (FCC), austenite (γ -phase) and body centered cubic ferritic δ -phases are present. The latter are probably present due to the high temperature gradient present during the SLM process. This gradient also generates a columnar microstructure, typical for SLM fabricated components. No martensitic phases are found. Lattice distortions are present, probably due to residual stresses from the build. Spherical inclusions of silicate containing chromium and manganese were also discovered. These inclusions work as dislocation inhibiting particles, thus strengthening the metal. Molybdenum inclusions are also discovered, creating dislocations further strengthening the material. The hardness is found to exceed the one normally obtained in annealed 316L SS.

Composition wise, some material additions such as carbon, may ameliorate the surface qualities and the wetting conditions of 2D-components by binding with oxygen, but will worsen the surface quality of 3D-components. Alloying phosphate in an Fe-melt seems to ameliorate wetting conditions by lowering surface tensions, in addition to lowering the melting point of the metal by almost 500 °C(Kruth et al. (2007)). Other components such as silicon and titanium, seem to worsen surface quality by increasing the irregular porosity and further forming carbides and oxides in addition to ease the formation of balling. Copper on the other hand, may have both positive and negative effects: If added as a powder, the density of the final component is affected, due to the high reflectiveness of the metal. Positive effects are obtained by alloying this metal in the SS powder.

Shunmugavel et al. (2015) describes in detail the microstructures of SLM Ti-Al6-4V, and compares these with the structures of its wrought counterpart. Due to the in-process layer-wise manufacturing and steep temperature gradients, an inhomogeneous structure with epitaxial growth of elongated grains, with the formation of acicular α -grains within β -grain boundaries, takes place in the scanning direction for SLM material. By a post-process heat treatment, the structure becomes

purely lamellar $\alpha + \beta$ -structure. Composition wise, the two materials are similar, but due to differences in microstructure, the SLM material's yield- and ultimate tensile strength (UTS) are higher than for the wrought counterpart. The same difference can be observed for the materials elongation, as the SLM material is stiffer than the wrought one. As a result, the SLM samples experienced more brittle fractures. In all cases, changing the build direction for the SLM metal, yields slightly different results.

As a general rule, the surface roughness's obtainable by SLM can range from a few tens to maybe right above 100 μm , still having densities of over 99.9% (Gibson et al. (2010); Kruth et al. (2007)).

When we look at Ti-6Al-4V manufactured using EBM, a structure of homoepitaxial β -grains growing in the heat-gradient direction constitute a highly anisotropic microstructure, with α -lammellae (hcp) growing in many directions inside the β -grain (bcc) boundaries. These α -structures are individually occurring, indicating the fast transition temperature gradient in the $\beta \Rightarrow \alpha$ -transition, even at the elevated chamber temperatures characteristic for the EBM process (de Formanoir et al. (2016)). However, the α/β microstructure seems to vary with the specimen thickness. Acicular martensitic α -structures are found in thinner sections, while transformed α/β -structures seem to appear in thicker sections (Toh et al. (2016)). These structures express an average Vickers microindentation hardness at 3.6 – 3.9 GPa which is approximately 1 GPa lower than the wrought counterpart, while UTS values for this material have been found to lay around 1.18 GPa (Murr et al. (2009)).

For both SLM and EBM, a large amount of settings and scanning strategies are available, resulting in a wide range of material structures. One possibility enabling the onset of grain growth, is to use a re-scan strategy.

1.3.5 SLM and EBM process related challenges

Having introduced the main material characteristics, some attention will now be directed towards the challenges one might face when manufacturing components using PBF processes, some of which are reported and discussed in more detail in the paper by Rombouts et al. (2006).

Firstly, the narrow spectre of materials available limits the current products to applications favouring these few materials. Some stainless steels are available, but the PBF process has a complex basis, yielding a non-equilibrium result which is inherently difficult to understand and to predict. There are many parameters influencing a PBF process, hence an offset in only one of these can cause defects in the print. Different alloying elements in the powder, or the use of different inert gases in the print-chamber may also play a role in the final properties of the material.

Oxygen and balling

Oxygen and molten metals does not combine well in any application. An effect that still holds true for PBF, as oxygen in the machine's build chamber may compromise the surface quality due to the increased melt pool during the scanning (melting of powder). This effect causes further oxidation of the involved metal atoms in the melt (Kruth et al. (2007)). As a result, an inert gas is used during manufacturing, but small quantities of oxygen might be trapped inside of the powders, resulting in

some defects. The previously mentioned inert gas, used in the EBM chamber also helps displacing the O₂ present in the powder.

Balling, a phenomena where the process influences the metal to create spheres of approximately 500 µm in diameter, which are detrimental to the metal structures, are often initiated by the oxygen content in the chamber atmosphere. Reducing it's quantity is helpful (Li et al. (2012)). Gusarov et al. (2007) is further trying to understand the balling effect by looking at heat transfer in the components during the SLM process. An ideal scanning speed interval is identified. Using faster speeds (over 20 cm/sec), yield in the formation of non-uniform broken melt tracks and result in an onset of the balling effect. This is attributed to the Plateau-Rayleigh capillary instability of the melt pool. One among multiple solutions, is to lower the scanning speed combined with changing in the laser cross section. Rombouts et al. (2006) further analyses the laser scanning speeds; where fast scans yields in lower material density, and slower scans attracts more of the adjacent powder to an enlarged melt pool.

Internal stresses, warping and surface finish

Warping of the print is a prominent issue, especially for SLM. The build plate and environment are kept at low temperatures (~100 °C), while the material fusing (from 50% to nearly 100% material density) is occurring at over 1000 °C. This temperature gradient creates an onset of shrinkage in the material, having a magnitude of ~ 4% (Gibson et al. (2010) p.124 and 141). Strong attachment of the component to the base substrate is imperative, in order to achieve uniform contraction and stable printing conditions. The EBM process has a higher work temperature in the chamber, thus reducing the heat gradient between each passing of the beam. This causes a reduction in the residual stresses present in the finished component.

Residual stresses are at the base of a variety of inaccuracies in the final products. Reducing these enables the possibility to build products with greater tolerances and better inherent mechanical properties. Shiomi et al. (2004) proposes methods for reducing the residual stresses: Heat treatments of the final build of up to 700 °C, reheating strategies by laser scanning during build (600 °C) and the preheating of the powder bed of up to 160 °C are among the researched strategies. These methods have proven to be very effective, and a combination of these may yield even better results.

Thanks to the narrow energy distribution in the laser beam, the SLM process is able to achieve surfaces with roughness's in the range of less than 20 µm (Strano et al. (2013)). Meanwhile, the EBM process is not able to achieve the same surface qualities as SLM due to the wider energy distribution of the electron beam. This drawback is however compensated by the faster build rates and less residual stresses present in the final print. These surface roughness's may not be smooth enough to satisfy the intended application, hence some degree of post-processing of the surfaces may be needed.

Components manufactured by PBF may experience an effect named *growth by sintering*, where neighbouring unmelted powder particles actually attach to the component by sintering, thus roughening the surfaces. This effect is due to the high energy and prolonged heat input inherent in these processes. Positive outcomes can be generated by this "skin formation" as it, combined with grain growth, will reduce the total porosity of the component. Using powders with finer particle grains will, to some degree, enhance the surface characteristics of the final print, but contemporaneously

result in worse flow properties and render the powder prone to self-ignition during handling.

When having the choice between EBM and SLM, it is important to contemplate which material characteristics are most valued in the final product.

Rolling of powders

Slotwinski et al. (2014) discusses an issue occurring during the rolling of new powder layers: The roller seems inclined to deposit the smaller grains first and to transport the larger grains ($>60\ \mu\text{m}$) all the way past the build plate. One can argue that this effect will change the average powder grain size in the final print, hence interfering with material qualities. Another feedstock related challenge, is the compaction of powders in the dispenser. The density of the powders will change the further down in the dispenser they are, due to the gravitational force. For tall components this may influence the final material density, but can easily be solved by lightly compressing the powder before the print is started (Gibson et al. (2010) p.49).

Internal structures

Due to differences in building strategies at the basis of the different AM processes, every process has its strength and weakness. One factor that needs further elaboration (as Table 1.1 only provides a limited overview) is the capability of different processes to manufacture components having enclosed internal structures.

Machines based on fused deposition modelling (FDM) have a building strategy based on the deposition of material only where needed, e.g. by the extrusion of polymer filament. This results in the ability to create closed geometries with internal structures, hence with walls enclosing e.g. a lattice structure (Figure 1.10, b). Between the struts of the internal lattice structure there will hardly be any loose material, apart from some extra filament generated by the movement of the extrusion head and potential support structures.

Meanwhile, machines based on PBF will be heavily limited in this respect. The inherent build strategy creates a complete layer of unmelted powder at every cross-sectional component layer. As a result, components with complete external walls and for instance an internal lattice structure will have sections of "trapped" unmelted powder. This powder is constrained by the external walls after the completion of the manufacturing process (Figure 1.10, a). Finding ways to enable the production of internal structures in closed components using powder based processes, will enable great progression in the world of implants. It's worth mentioning that some manufacturers already have proprietary techniques in this regard.

1.4 Topology optimisation

There are many different lattice geometries to choose from when designing a component with internal structures. Gyroid lattices (Yan et al. (2012)), cubic hatched lattices (Parthasarathy et al. (2010)) or diamond lattices (Heinl et al. (2008b)) are a few examples of geometries previously studied. Different designs have unique inherent structural characteristics, determining the final stiffness of the structure. Let's take a diamond lattice as an example: Due to the struts being tilted at less than 90°

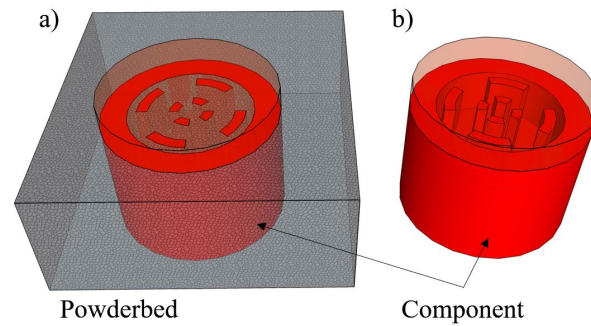


Figure 1.10: Limitations of internal structures

a) Shows a component with internal structures while being manufactured in a PBF machine. At the end of the process there will be trapped unmelted powder between the internal structures. Due to the complete external walls, this powder cannot be removed without breaching the walls. b) Shows a component manufactured using FDM. No residual powders are left behind, since the manufacturing process only deposits material where needed.

in every direction (Figure 1.11, a), this lattice receives its strength from the bending stiffness of the struts. Meanwhile, a hatched cubic lattice oriented normal to a plane (Figure 1.11, b), draws its strength from the compression of the normal struts. Lattices characterised by compression will need thinner struts in order to achieve the same reduced stiffness of a lattice characterised by bending. Other than altering the design, lattice stiffness can also be altered by means of four additional controllable parameters:

The orientation of the lattice itself will influence the direction of maximal stiffness. A cubic lattice is inherently strong in three main directions: Along the struts. By orienting this lattice in space, one can optimise the strength characteristics according to the expected loading directions.

The orientation of the component during printing will influence the material characteristics at a microstructural level. The material will be stronger perpendicular to the build direction (Figure 1.11, c) due to the complete melt pool at each layer in this direction. Conversely, the material will be weaker along the build direction due to poor layer to layer adhesion, defects and/or unmelted spots. A lattice oriented at 45° will have predominantly similar strength characteristics in every main direction (Figure 1.11, d).

Pore and strut diameters will control the final porosity of the scaffold. A variation among these parameters will modify the stiffness characteristics in a scaffold to a large extent, as demonstrated by e.g. Heinl et al. (2008a,b); Tellis et al. (2008).

All the aforementioned is true for all regular lattices. When implementing topology optimisation of the lattice however, all these variables can be adjusted for each individual lattice element. Topology optimisation was defined by Wang et al. (2016b) as: "*A mathematical method capable of rearranging the materials to attain desired properties while satisfying prescribed constraints.*" This method is not bound by the normal geometrical lattices used in the generation of periodical structures. A long series of computational analyses can be run to ensure that the right stiffness is attributed to each element in the lattice. This is done by varying parameters such as the strut thickness, orientation, length and overall size of the individual lattice cell.

If a complete design of an additive manufactured implant is needed, one will have to take into

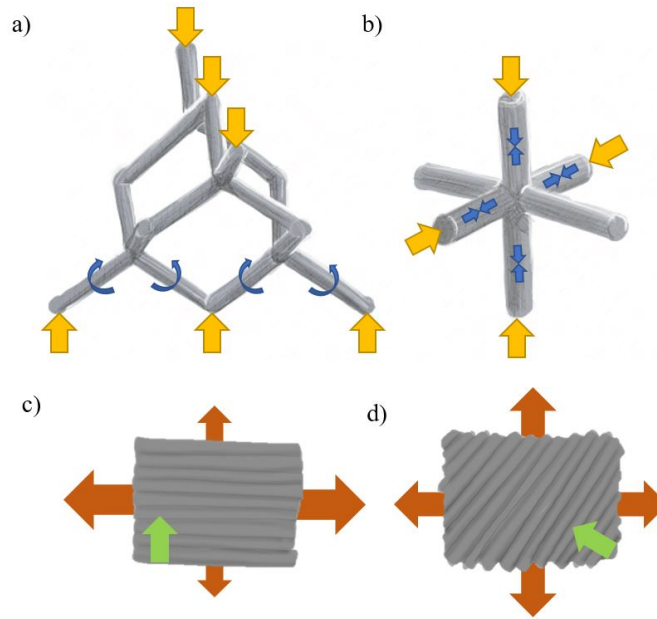


Figure 1.11: Force propagation in lattices

a) Shows how forces (yellow arrows) input to a diamond lattice will propagate through the structure by bending mechanisms (blue, rotational arrows). b) Shows how forces (yellow arrows) input to a cubic hatched structure will propagate through compression mechanisms (blue, counterfacing arrows). c) and d) show the strengths of AM materials with respect to the printed directions (green arrows). The size of the orange arrows indicate the magnitude of the strength in each direction.

account all the stiffness altering parameters, together with the different lattice structure geometries. By doing so, one can take advantage of the complete potential in the AM process.

1.5 State of the art

Some of the relevant studies previously conducted by other authors, will be briefly introduced in this section. We start by looking at cellular processes on 2D scaffolds and subsequently move on to the 3D domain.

Regarding the use of different metals in the manufacturing of implants, it is important to use biocompatible material compositions. These should ideally match the concentration elements already present in the body. New elements having toxic properties should not be introduced. As metals are already in common use in implants, a variety of studies exist regarding the cytocompatibility and osteoconductive properties of bulk biomaterials. Materials such as 316L SS and titanium (e.g. Liu et al. (2006, 2004); Nouri and Wen (2015); Oshida (2013); Singh et al. (2014)). These materials are, with proper (surface-) treatments, deemed safe to use in implants. Anyhow, with the recent implementation of AM into the implant manufacturing, new data may have to be collected regarding the material reactions when introduced to the human body.

1.5.1 2D scaffolds

Interesting work concerning osteogenesis on 2D scaffolds was done by Faia-Torres et al. (2015) (and Faia-Torres et al. (2014)). Both used BMSCs that were cultured on polycaprolactone scaffolds produced with diverse surface gradients. The results suggests that a surface roughness, Ra , between $0.93\ \mu\text{m}$ and $2.1\ \mu\text{m}$ and R_{sm} between $135\ \mu\text{m}$ and $71\ \mu\text{m}$ tend to better support this kind of differentiation in absence of osteogenic supplements. These results are also supported in the review by Metavarayuth et al. (2016).

Kolind et al. (2014) studied the differentiation and mineralisation of dental pulp derived stem cells (DPSC) with and without osteogenic differentiation factors in medium (OM). They found that topological differences between the different micro groove combinations did not seem to influence the FAs. Larger interpillar gap sizes reduced the proliferation of the cells. Lastly, cells cultured with OM demonstrated no difference in mineralisation among the different pillar dimensions, while cells cultured in OM-free conditions seem to favour $4\ \mu\text{m}$ pillars of $1\ \mu\text{m}$ height.

Sun et al. (2016a) studied proliferation and osteogenic differentiation of BMSCs on a polylactic acid (PLA) and hydroxyapatite (HA) composite. By observing the morphology, the cells appeared to favour microstructures combined with HA. Proliferation on the other hand, did not appear to depend on the availability of HA. When looking at the osteogenic differentiation, the cells appeared to favour PLA over HA. Surface coatings prove to have distinct characteristics influencing cellular processes, some of which are reviewed in Raphel et al. (2016). By doping HA with antibacterial agents, good proliferation and differentiation conditions were achieved, with an additional protection against bacterial infestation.

Fiedler et al. (2013) generated nanopillars on Si wafers, subsequently culturing BMSCs and osteoblasts on them. Results show that similar adhesion characteristics are observed between the two cell types and that nanotopography does not affect the adhesion. Osteoblasts on the other hand, seem to prefer $20\ \text{nm}$ pillars with respect to proliferation. Structures of $50\ \text{nm}$ were most potent in inducing osteoblastogenesis.

Abagnale et al. (2015) investigated the influence of topographical cues on adhesion of BMSCs. In particular a connection is found between etched microgrooves and the orientation, migration and elongation of the cells. Grooves of approximately $15\ \mu\text{m}$ showed an upregulation of FAs. Ridges of approximately $2\ \mu\text{m}$, showed increased affinity for supporting osteogenic differentiation. Nanostructures of $650\ \text{nm}$ seem to support differentiation towards both osteogenic and adipogenic lineages, although not being able to induce differentiation without e.g. ODM.

Dalby et al. (2014) explored how adhesions are influenced by nanotopography. Cells have a tendency to orient themselves to underlying nano and microtopography. This mechanism is attributed to filopodia, which are small integrin-containing spikes forming extensions in the cell membrane.

1.5.2 3D scaffolds

When moving towards 3D metal scaffolds, we are also moving closer to the potential application in implants. New challenges and opportunities emerge, some of which are described in the following literature. By employing AM in the production of porous scaffolds, it is worth researching the stiffness characteristics of the scaffolds. By doing so, it is easier to transfer the geometries proving to have the best osteoinductive and osteoconductive properties to implant design.

The author in Niinomi (2008) reviews previously conducted work with a focus on material characteristics suitable for implant production. In particular, the suitable range in Young's modulus is given priority. To avoid stress shielding the implant structure should follow the mechanical characteristics of bone, as previously described. Manufacturing overly soft implants will result in the onset of fibrous tissue formation during osteointegration. The best value of structure stiffness needs to be found.

Sidambe (2014) compared studies of cell processes from different authors. With respect to the specific material properties, it is mentioned that the low electrical conductivity of the Ti-Al6-4V material generates an advantageous passive oxide layer on the surface of implants. Adhesion of cells onto metals usually poses many challenges, but with the formation of an oxide layer, the chemical structure of the material becomes ceramic-like. Generally, ceramics show better adhesion characteristics than metals.

Some challenges related to the skin formation and geometrical deformations which may be experienced when using AM. Yan et al. (2012) manufactured lattice structures by SLM in 316L stainless steel, based on a gyroid unit cell and characterised the manufacturability of such structures. Good geometrical agreement of the structures were found with respect to the CAD model, although many partially melted particles were found on the surfaces. Smaller unit cells resulted in reduced porosity which resulted in both a higher Young's modulus and yield strength. The dimensions of the porous metal scaffolds were 2 mm, 3.5 mm, 4.5 mm, 5.5 mm, 6.5 mm and 8 mm. The dimensions are given in unit cell sizes.

Also Heintz et al. (2008a,b) studied titanium scaffolds, this time manufactured an ASTM-grade biomaterial. The scaffolds were produced by EBM with mechanical properties resembling those of bone. The mechanical properties are analysed and reported. With an increasing porosity and a decreasing electron beam energy during production, the scaffold stiffness was reduced. The pore- and strut-sizes used varied from 68 μm to 182 μm and from 420 μm to 540 μm respectively.

When researching the cellular processes occurring on such porous scaffolds, the ideal porosity leading to osteogenesis needs to be found. Li et al. (2016), manufactured Ti-6Al-4V scaffolds with varying porosity, ranging from 300 μm to 700 μm . Smaller porosities between 300 μm to 400 μm , showed better adhesion and proliferation tendencies compared to the other porosity magnitudes. These were also implanted *in vivo* in goats, yielding positive osteogenic results.

In Sollazzo et al. (2011), highly porous titanium scaffolds were manufactured using a trade-marked method, having pores of approximately 800 μm . The *in vitro* osteoinduction of BMSCs was evaluated, yielding mixed results. In short: Although the tests were conducted over short time periods, the material seemed to positively influence the BMSCs differentiation. The expression of the important osteogenically inducing gene RUNX2 was delayed, meaning the differentiation was onset by other genes (ALP, FOSL1 and SPP1).

Cheng et al. (2014) studied the *in vitro* behaviour of selective laser sintered Ti-6Al-4V differently porous scaffolds. These were designed using a trabecular bone model, and further surface treated with among other acid etching. The scaffolds were seeded with osteoblast-like MG63 cells, showing better osteoinduction with increasing porosity. The pore- and strut-sizes, here ordered with increasing material porosity, were ranging from 177 μm to 653 μm and 628 μm to 305 μm respectively.

The review conducted by Karageorgiou and Kaplan (2005) provides interesting knowledge

about porosity in implant application. *In vitro*, lower porosity will sooner lead to osteogenesis by a mechanism inhibiting proliferation. Meanwhile, *In vivo* tests show that increased porosity lead to a higher in-growth of bone, although simultaneously reducing the mechanical properties of the implant. The minimum pore size for bone generation is identified to be 100 μm due to the size of the seeded cells. Any smaller pores would result in the cells spanning over the pores thus inhibiting in-growth. Larger pores are hence recommended for better bone-formation. The increased vascularisation onset in larger pores, leads to direct bone formation and limits the onset of callous tissue generation.

Lewallen et al. (2015) investigates the techniques and materials available for future implant-manufacturing. They conclude by focusing on the intriguing potential of biologically enhanced porous scaffolds. These scaffolds are not commonly researched at this time, but they may provide the basis for future implants. The cell processes of BMSCs need also to be better understood, as a next step.

1.5.3 Main challenges

As the previous sections show, the influence of roughness is been investigated for the 2D domain, showing that specific surface morphology and chemistry have an effect on the osteoinduction, i.e. the proliferation and differentiation of BMSCs. In the 3D domain, the performed studies mainly investigate the effect of different porosity on the osteoinductive properties, however, scarce contributions are found studying the combined effect of surface morphology and porosity on osteoinduction. This may be rooted in that porous structures proving beneficial for inducing differentiation are on a sub-millimeter scale. It is therefore inherently difficult to perform surface finishing processes on these porous structures. Methods that would enable this, are a topic that need further investigation. Additionally, finding ways to manufacture larger metallic parts having such microstructures will probably constitute a large step towards the development of fully porous implants.

Secondly, it is well known that *in vitro* studies struggle to represent what happens once the implants are used *in vivo*. *In vitro* studies does have an advantage in that they are able to isolate effects by single variables. However, looking at the effects of porosity and surface roughness in more in-vivo like culture conditions may prove beneficial. Conducting animal studies is vastly expensive and a cause of suffering, the development of *ex-vivo* culturing methods having characteristics that mimic *in vivo* conditions, will enable more research to be conducted in this field.

The comparison of osteoinduction in 3D, 2D, osteogenic conditions and non-osteogenic conditions is also needed. Some studies especially in the 3D domain, does not specifically compare the different *in vitro* culture conditions against each other. In order to advance and generate new knowledge, the porosities and roughness previously found to be best suited for osteoinduction need to be compared e.g. 2D conditions. The knowledge gathered will be useful in the development of better scaffolds.

A model needs to be developed, able to predict the surface and porosity effects on the osteoinductive properties. This will require a lot of experiments, as there are many alterable parameters that will need to be connected by appropriate mathematical relations.

Aim of the thesis

The scope of this work was, as introduced in chapter 1, focused on applying additive manufacturing in the next generation of arthroplasty implants. Clearly this scope is closely connected to the field of biomedical engineering. For this Master's Thesis in particular, areas from both mechanical engineering and tissue engineering were of importance.

The overall objective was to study the effect of porous Ti-6Al-4V scaffolds on the osteoblastogenesis of BMSCs. An hypothesis was defined:

Additive manufactured porous Ti-6AL-4V scaffolds are both osteoinductive and osteoconductive.

In order to research the hypothesis, two objectives were set:

The first objective was to design and manufacture 3D porous scaffolds having characteristics suitable to support osteogenesis. It was also important that their design simplified the characterisation process.

The second objective was to perform *in vitro* laboratory tests of BMSCs seeded on the porous additive manufactured scaffolds. Cellular responses connected to osteoblastogenesis including adhesion, proliferation and differentiation were studied.

The overall goal was to generate new knowledge on the porosity effects of AM titanium scaffolds on osteointegration. Knowledge that could be used in the development of future implants.

2.1 Outline

A general introduction and a detailed literature review was compiled in chapter 1, introducing a wide range of topics and theory related to the study.

In chapter 3, the procedures and characterisation methods used during the experiments are explained, together with general background theory of the selected processes. Basic information needed to ensure the repeatability of the conducted tests is provided. This chapter also sheds light on some of the choices made prior to initiating both the manufacturing of scaffolds and the laboratory work.

In chapter 4, experimental results are presented for each of the tests performed during the experimental part of this study.

A discussion will follow in chapter 5. A chapter aimed at trying to evaluate the hypothesis. Results from the experiments will be discussed in light of the knowledge gathered from other literature. The sum of all the indices may yield a final outcome for the hypothesis.

chapter 6 will summarise the results and conclude this Master's Thesis.

2.2 Previous work

During the course of the Project Thesis preceding this Master's Thesis, initial cellular processes of BMSCs seeded on AM scaffolds were studied. 316L stainless steel scaffolds were manufactured using SLM and then surface finished to different surface roughness's using magnetic abrasive finishing. BMSCs were then seeded onto the scaffolds and the adhesion was studied. This work is presented in a conference paper, a poster and a manuscript submitted for peer review in Appendix A (section .1, section .2 and section .3).

Experimental methods

3.1 Scaffold design and manufacturing

The aim of using 3D porous scaffolds was to see if the cells are behaving differently in a ECM-like environment compared to normal 2D-scaffolding. Specifically, the osteoinductive and osteoconductive properties of the scaffolds are examined. To secure a relevant outcome for this study, previous articles using/reviewing porous scaffolds were studied (e.g. Li et al. (2016); Heintl et al. (2008a,b); Yan et al. (2012); Sollazzo et al. (2011)). By combining the geometrical data used in these studies, a general measure of the unit-cell dimensions was set. Two additional criteria were at the basis for the resulting lattice-geometries of the 3D scaffolds manufactured:

Firstly, in order to evaluate the effect of only one pore size, an isometric structure of equidimensional pores was needed. Secondly, due to the limitations inherent in the microscopy characterisation process, a structure displaying 3 unit-cell formations in depth from a normal angle was also needed. One option is graphically explained in Figure 3.1.

The resulting scaffolds are characterised by fully rounded cubic lattices, tilted at a 35° angle (Figure 3.2). To ensure manufacturability, accessibility during microscopy and vascularisation, both the pore diameter and lattice-strut diameter are set to a dimension of 800 µm. The overall thickness of the scaffolds are set to 5 mm, thus providing approximately three lattice layers over the thickness. Since some of the experiments conducted in the laboratory requires a larger number of living cells to be seeded, two scaffold diameters are designed: 6 mm and 14.6 mm, dimensions that fit inside 96-well and 24-well plates respectively. Both standard plates commonly used in cell biology.

3.1.1 Experimental

The unit cell of one lattice, depicted in Figure 3.2 c), was first modelled in SOLIDWORKS (DassaultSystems, France) and exported as a .prt file. An assembly was created where the .prt file was patterned in every direction until enough lattices covering the planned scaffold size were formed. This assembly was then exported as a new .prt file and opened in the modelling area of the software. The different components were united and subsequently cut-extruded to the right geometry

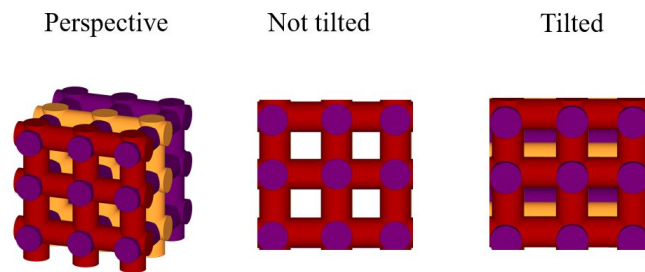


Figure 3.1: Tilted lattice

It may prove difficult to image a scaffold (left) with a vertical oriented lattice (middle). By tilting the lattice by a given angle (right), struts in the underlying layers may be visible for characterisation during optical microscopy.

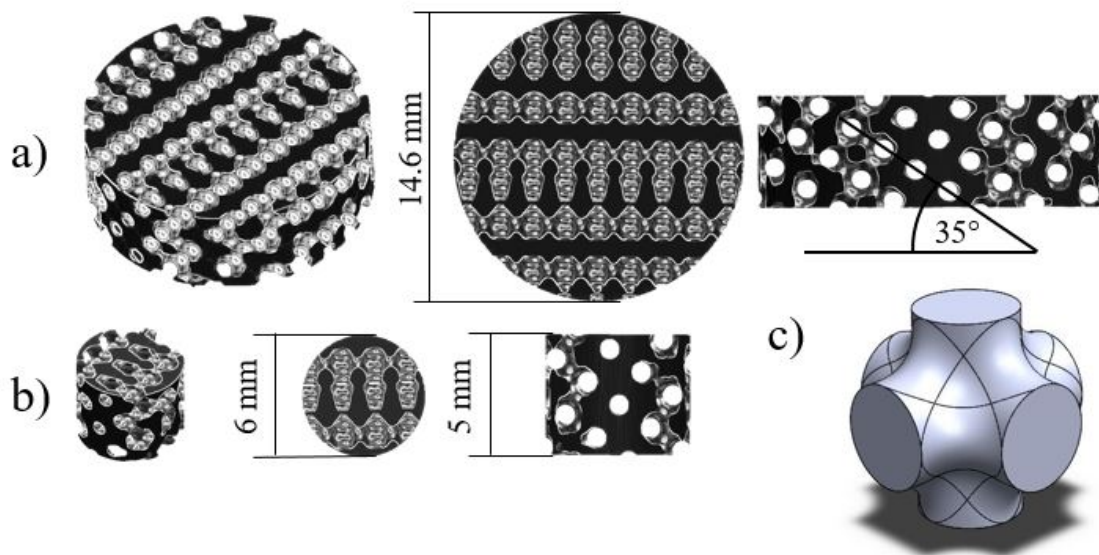


Figure 3.2: 3D porous scaffold geometry

An overview of the 3D porous scaffolds manufactured. a) 14.6 mm diameter scaffold, designed for use in 24-well plates and b) 6 mm diameter scaffold, designed for use in 96-well plates. The lattice is oriented at 35° for characterisation purposes. c) 3D model of the unit cell.

Table 3.1: EBM settings

Some of the settings used during the manufacturing of the porous scaffolds. Data provided by the manufacturer.

Setting	Value
Hatch Line offset	200 μm
Number of contours	4
Power (max, electron gun)	3000 W

and angle. The resulting part was saved as an .stl file and used for printing.

CAD models of the custom porous scaffolds were sent to Germany, where the production of the scaffolds was done by an AM-group (FIT AG, Lupburg, Germany) using EBM technology. Some of the parameter used during manufacturing are reported in Table 3.1.

A selection of 3D porous scaffolds were analysed in a scanning electron microscope (SEM, Quanta SEM, FEI, Thermo Fisher Scientific), with a secondary electron detector and an everhart-thornley detector at both 500X and 100X magnification magnitudes, in order to characterise the scaffold's surface properties.

A finite element analysis (FEA) in compression was performed using SOLIDWORKS, by loading the original CAD model of the small scaffold into the simulation application on SOLIDWORKS. Two massive plates were modelled in contact with the top and bottom surface to distribute the loading evenly. Then, isotropic Ti-4Al-6V was selected as model material before a fixed constraint was defined for the bottom surface of the scaffold. The loading was defined as an orthogonal unit displacement of 0.01 mm applied to the top surface. An FFPlus iterative solver with a standard solid mesh was selected for meshing the component, before the simulation is run and an automatic analysis report is saved. The details of the settings and properties are reported in Table 3.2.

By extracting the reaction force from the post-simulation results, it is possible to calculate the elastic modulus (Young's modulus) of the scaffold in GPa, using Equation 3.1.

$$E_{material} = \frac{F_{reaction} * h_{scaffold}}{A_{scaffold} * \delta_{displacement} * 10^3} \quad (3.1)$$

Where $E_{material}$ [GPa] is the elastic modulus of the scaffold, $F_{reaction}$ [N] is the reaction forces expressed by the scaffold during compression, $h_{scaffold}$ [mm] is the total height of the scaffold, $A_{scaffold}$ [mm²] is the section area of the scaffold and $\delta_{displacement}$ [mm] is the total displacement of the compression.

The results from the simulations were compared to a compression test, run on a large scaffold using a material testing instrument (ElectroPuls, Instron® E10000, Instron, Norwood, USA) and standard analysis software (Bluehill 3 testing software, Instron®). The scaffolds were compressed between two standard compression plates. A displacement over time function was used (0.1 mm/min), resulting in the crossheads moving towards each other until maximum preset load was reached. The principle is graphically depicted in Figure 3.3. Prior to compression, the surfaces of the scaffold were abrasively polished using grit paper (P500), to remove the major surface roughness.

Even after polishing, the surfaces of the scaffolds had some inherent defects and porosity. In order to achieve relevant test results, the scaffold area assumed to be in contact with the crossheads

Table 3.2: FEA settings
Material and mesh settings for the FEA.

Material properties Ti-6Al-4V solution treated and aged	Yield strength (Y_s)	827 MPa
	Elastic modulus (E)	104.8 GPa
	Poissons ratio	0.31
Mesh properties	Mesh type	FFEPlus
	Element size	0.35 mm
	Nodes	45 449
	Elements	28 176

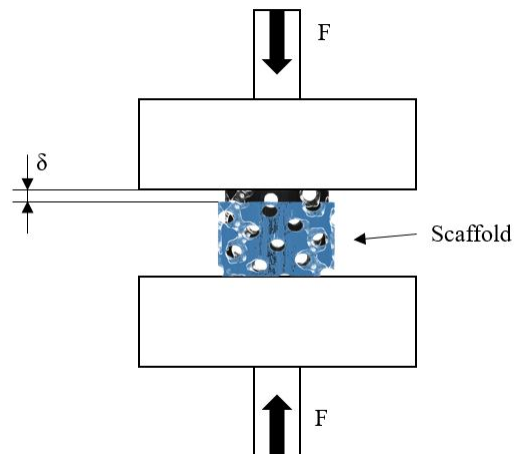


Figure 3.3: Compression test

The scaffold (black) is compressed (blue) between two compression plates, using a force (F). A change in height (δ) is experienced with increasing force and by logging the force versus displacement, the Young's modulus of the scaffold can be calculated using Equation 3.1.

(planar area) was calculated by means of an image analysis performed in a suitable software (ImageJ): Reflection images taken of the scaffolds were colour split, before the threshold was adjusted to only show the planar parts. A particle analysis plugin was used to calculate the total percentage of planar area present on the scaffold surface. The resulting number was used as a scaling factor plugged into Equation 3.1, as shown in Equation 3.2. Where f_{area} is the area scaling factor. This method obviously has some weaknesses and sources of error which will be discussed further in chapter 5.

$$E_{material} = \frac{F_{reaction} * h_{scaffold}}{A_{scaffold} * f_{area} * \delta_{displacement} * 10^3} \quad (3.2)$$

3.2 LAL and cleaning procedure

The LAL (Limulus ameocyte lysate) assay is a test designed to detect bacterial endotoxins in samples. The assay is based on the coagulating characteristics of the blood from the horseshoe crab (*Limulus Polyphemus*). The blood cells (amoebocytes) are separated from the rest of the serum by spinning. These are subsequently lysed before the released substances are harvested. When endotoxines come in contact with the lysate, coagulation is onset, thus creating a quantifiable signal Tsuji et al. (1980).

Prior to being seeded, the scaffolds needed to be free of any contamination. The cleaning procedure described in the following was developed during the project work prior to the master thesis (appendix A).

3.2.1 Experimental

Initial scaffold cleaning was performed with a 5 min ultrasonication in distilled water, thus removing any loose debris from the scaffolds. The scaffolds were subsequently ultrasonicated in acetone for 5 min, to remove any grease-, oil- and wax contamination. Then the samples were ultrasonicated 5 min in 70 % ethanol, thus killing most microbiological life still present on the surfaces. Finally the scaffolds were autoclaved, a step that constituted the final cleaning process before the scaffolds were used in the laboratory.

In order to assess the effectiveness of the cleaning procedure, one of the 316L stainless steel scaffolds used in the pre-master project (Appendix A) was incubated in *Roswell Park Memorial Institute medium* (RPMI, Sigma-Aldrich®, Missouri, USA) for 24 h. The supernatant was harvested and LAL-tested against a medium control.

3.3 Mediums and BMSCs preparations

As reported by Prins et al. (2009) the use of PL in medium seems to enhance the proliferation of BMSCs, hence PL is used as growth factor in the BMSCs cultured in growth medium (GM). FBS was used in the osteogenic medium (OM).

Preceding addition to the GM, the PL was spun (2000 g, 10 min, RT) and subsequently micro filtered using a 45 µm pore size filter, in order to limit fragments in the medium.

Composition of the mediums used during the course of this study was as follows:

Basic medium, composed of Minimum Essential Media Eagle (MEM- α , Thermo Fisher Scientific, Massachusetts, USA), with 5000 IE/mL antibiotics.

Growth medium (GM), based on the basic medium with an addition of 10 U/ml heparin, 3.4 mM glutamine and 5 % PL.

Osteogenic medium (OM), based on the basic medium with an addition of 2 mM glutamine, 0.2 mM vitamine C, 10^{-6} mM dexamethasone and 10 % FBS.

3.3.1 Experimental

A batch of BMSCs (donor 06) containing approximately 10^6 BMSCs at passage five was retrieved from the cryogenic freezer and heated to room temperature (RT). Fresh GM was added before the cells were spun (953 g, 5 min, RT) and the supernatant removed. Next, 55 ml GM was added to the cells and a thorough mixing was performed, before the cells were seeded at a concentration of $\sim 20\,000$ cells/ml in two 175 cm^2 culture flasks (Corning®, Tewksbury, USA). Incubation followed (4 d, 37°C , 5 % CO_2).

After 4 days, the BMSCs were trypsinated in the following way: The GM was removed and the cells were washed with Dulbecco's phosphate buffered saline (Thermo Fisher Scientific), before trypsin was added and BMSC detachment was confirmed under normal light microscopy. Old medium was subsequently reintroduced to the culture-flasks, thus deactivating the trypsin. The suspension was spun (953 g, 8 min, RT), the supernatant poured off and 2 ml basic medium was added prior to cell counting.

10 μl of the suspension was extracted and diluted to 100 μl , then 10 μl of the diluted suspension was transferred to a haemocytometer for cell counting. The average of $n = 6$ counts was used as the significant value.

All cells used in the following experiments were used before passage 7.

After cell counting, the amount of culture medium (either DM or OM) needed for seeding the scaffolds was prepared and subsequently mixed with a pre-calculated amount of cells previously suspended in basic medium. The final suspension had a concentration of $1000\frac{\text{cells}}{\mu\text{l}}$, a concentration determined to fit the seeding of the scaffolds in question. This BMSC concentration was used for all scaffolds seeded during this study.

The scaffolds to be seeded were placed in non-adherent 25-well plates (Replica schalen 25-vaks, Greiner bio), before the cell-suspension was carefully pipetted onto the scaffolds. Then the plates were incubated at 37°C (5 % CO_2). The scaffolds requiring longer incubation time than 48 h, were transferred to normal 24-well plates (Corning® Costar®, Thermo Fisher Scientific) after 3 d and were kept in these for the duration of the experiment.

3.4 Confocal microscopy and adhesion

Confocal microscopy functions basically in the same way as conventional microscopes, but most of the light reflected by the analysed sample is excluded. By doing so, only the light coming from

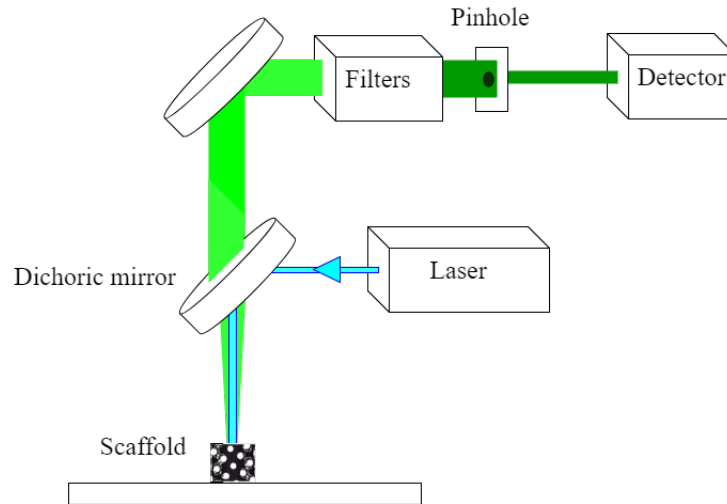


Figure 3.4: The confocal microscopy principle

Light at preset wavelengths (turquoise) depart from the laser and is reflected by the dichoric mirror, towards the scaffold. The fluorophore in the cells is excited and emits light having longer wavelength (green), which is then able to pass unhindered through the dichoric mirror. After a series of filters and reflection stages, the remaining filtered light passes through a pinhole that removes any unwanted reflections and *out-of-focus* signal. The light finally reaches the detector which captures and stores its intensity. Next, the process is repeated for neighbouring points until an entire image is formed.

the desired, in-focus, cross-section of the sample reaches the detector. As a result, samples that would appear blurred and out of focus in conventional light microscopes will appear clear and in focus using the confocal microscope. This filtering process is done by passing the reflected light from the stage through an adjustable pinhole, thus excluding most of the rays. The image is then built point by point, scanning the laser beam across the sample.

By exploiting the fluorescence expressed by fluorophores (dyes), biological materials can easily be imaged. Staining cells (e.g. BMSCs) with a fluorophore and subsequently illuminating the material with the laser source, will excite the electrons in the dye molecules. These electrons will emit light with longer wavelengths (photons with lower energy) when returning back to their normal energy level. This light constitutes the reflected light finally reaching the detector. Different flourophores can be attached to different parts of the cells, and by switching in-between two excitation wavelengths, different parts of a cell can be imaged and further superimposed on each other with different colours.

One of the vital components of such microscopes is the dichroic mirror, which allows light with a certain wavelength to pass, but reflects all other wavelengths. This is used to lead the laser light toward the sample, but at the same time ensuring that the reflected light (with longer wavelength) passes unhindered on the return trip (Semwogerere (2005); Pawley (2006)). A simplified schematic representation is provided in Figure 3.4.

3.4.1 Experimental

Four 96-well metal scaffolds were seeded with BMSCs cultured in GM and incubated as described in subsection 3.3.1. The cells adhered to the scaffolds were fixed at set incubation time points (8 h, 16 h, 24 h, 48 h), according to the following procedure: The scaffolds were washed with phosphate buffered saline (PBS) to remove old medium before being incubated with formalin in PBS (3.7 %, 15 min, RT). Then, three new wash-cycles with PBS were performed before the scaffold was stored in PBS (4 °C) until staining.

Following the fixation of the last scaffold, a staining procedure was conducted, in order to prepare the cells for characterisation. First, the cells were permeabilised and blocked by incubating the scaffolds with human serum in saponin (1 % cons., 15 min, RT). Then the scaffolds were washed with PBS, immersed in Draq5™ 633 in PBS (1 % cons., eBioscience™, Thermo Fisher Scientific) and incubated (10 min, RT, dark), in order to stain DNA. Finally, the scaffolds were washed with PBS, immersed in Alexa Fluor® 488 Phalloidin in PBS (2.5 % cons., Invitrogen™, Thermo Fisher Scientific), in order to stain the actin-cytoskeleton.

Characterisation of the adhered cells on the scaffolds was performed in a confocal laser scanning microscope (LSM 710 Meta, Carl Zeiss Microscopy GmbH, Germany) using a 10X dry objective (N-Achroplan 10x/0.25 M27, Carl Zeiss). Settings and scanning depths were adjusted to values suitable to improve the individual image acquisition. Given the rough nature and the porosity of the scaffolds, Z-stacks were performed on every scaffold. Z-stacks are constituted by multiple 2D images, at different focal lengths, stacked on top of each other thus forming a 3D rendering of the cell morphology. Since this thesis is in 2D-format, top-down projections of the Z-stacks are made using a suitable software, creating a 2D image with a long focal length.

3.5 alamarBlue® and BMSC activity

The metabolic activity of the BMSCs was measured by the well established alamarBlue® staining assay, which workings is enabled by the cell's own reducing capabilities. By introducing a known concentration of resazurin into the medium, the reducing environment in the cell's cytosol is capable of performing a reduction from the latter to resorufin, which is a fluorescent compound. By measuring the resulting fluorescence post-excitation, a quantification of the biological activity is possible. alamarBlue® is a non-toxic assay, which means that the assay can be run at multiple time points throughout the incubation period.

3.5.1 Experimental

Cells were seeded on two 96-well metal scaffolds, one cultured in OM and one in GM, as described in subsection 3.3.1. In addition, two types of controls were used during this experiment: Firstly, an "only medium" control was established, consisting of the two respective mediums in separate wells. Secondly, two separate metal scaffolds were used as additional "metal control", where one was submerged in GM and the other in OM. All the above described wells were incubated and handled equally for the duration of the experiment.

At set time points (6 h, 14 h, 22 h, 46 h, 70 h, 5 d and 7 d), alamarBlue® was added to the suspension (10 % cons., Thermo Fisher Scientific) and incubated (2 h, 37 °C, 5 % CO₂) before the supernatant was harvested. New medium was added to the scaffolds, before incubation was continued until the following assay time point.

Once harvested, 100 µl of the supernatant was transferred to black, solid bottom 96-well plates. The plates were subsequently scanned in a multilabel fluorescence reader (Victor³, PerkinElmer, Waltham, USA), using an alamarBlue®-dedicated analysis setup. All samples were run in triplicates and all plates were scanned at each time point. To limit the evaporation and degradation of stained media between scans, the outermost wells of each plate was filled with PBS in addition to the plates being stored in a refrigerator (4 °C, dark).

The "metal control" results were subtracted from the results obtained from the BMSC seeded scaffolds and the standard deviation of the results was calculated as described in Equation 3.3.

$$SD_{tot} = SD_{metalcontrol} + SD_{BMSC} \quad (3.3)$$

Where SD_{tot} is the total standard deviation, $SD_{metalcontrol}$ is the standard deviation of the "metal control" and SD_{BMSC} is the standard deviation of the scaffolds seeded with BMSCs.

3.6 ALP staining

Alkaline phosphatase (ALP) is a polyfunctional enzyme which regulates cell division and plays an important role in the early mineralisation process during osteogenesis (Kamalia et al. (1992)). Early in the process of osteoblastic differentiation and cartilage growth, ALP is upregulated by complex mechanisms. Then, towards the end of the differentiation process when e.g. Osteocalcin is upregulated, the ALP expression decays. Researchers have also used ALP to discriminate osteogenic lineages in heterogeneous stromal cell populations.

When an ALP stain is used on fixed and permeabilised cells, the stain will connect to the ALP present on the cell's cytoskeleton. By characterisation in a fluorescence microscope, the stained cells will emit green fluorescent light. If a suitable DAPI/Hoechst filter is used, the cells can easily be imaged.

3.6.1 Experimental

Cells at day 10 were fixed in formalin (3.7%), permeabilised and blocked using HS in saponin (1%) and stained with Draq5TM. A batch of ALP staining was prepared (ELF® 97 Endogenous Phosphatase Detection Kit, E6601, InvitrogenTM, Thermo Fisher Scientific) at a 1:20 ratio solution between ELF 97 phosphatase buffer and detection buffer, according to manufacturers instructions. The ALP staining was kept in the dark until characterisation, when it was added to the scaffold right before microscopy as short reaction times were expected (within 90 s).

The scaffolds were characterised in an inverted fluorescence microscope (IX71, Olympus Europa GMBH, Hamburg, Germany), using 10X and 20X magnification dry objectives. 350 nm UV and 630 nm excitation lights were used. A DAPI/Hoechst longpass filter was used to visualise the ALP stain, while a 650 nm longpass filter was used to image the nuclei. Other settings were adjusted to optimise each acquisition.

3.7 PCR analysis

To evaluate the gene expression at different stages of osteogenic differentiation, polymerase chain reaction (PCR) analysis was used, as described in the next sections. This is a test capable of detecting the relative signal of genes expressed at a given stage of cellular development.

3.7.1 Experimental

Six 24-well metal scaffolds were seeded as described in subsection 3.3.1 (these are hereby referred to as "round 1", three were cultured in GM and three in OM, before incubation (37 °C, 5 % CO₂). Medium was changed every 3–4 d, while samples of the old medium were harvested, spun (8 min, 800 G, RT) and the supernatant frozen (–80 °C) for future testing. The BMSCs on two scaffolds, one from the GM group and one from the OM group, were lysed at set time points (7 d, 14 d and 21 d) using Lysis/Binding Buffer (Roche High Pure Isolation Kit, Roche Diagnostics Norge AS, Oslo, Norway) and stored (–80 °C) for RNA isolation and cDNA-synthesis.

Further six large scaffolds were seeded at a later time point (these are hereby referred to as "round 2"). In this second round 2D controls in 6-well plates were also seeded and put through the same treatment as the metal scaffolds.

RNA isolation

RNA from the harvested cell lysates was extracted using a RNA isolation kit (Roche High Pure Isolation Kit) following the standard procedures provided by the manufacturer. After completion, the concentration of RNA was measured using a spectrophotometer (NanoDrop 1000, Thermo Fisher Scientific). RNA was then stored at –80 °C.

cDNA synthesis and PCR

The harvested RNA was used to synthesise cDNA, by reverse transcription (High-Capacity RNA-to-cDNATM Kit, Applied Biosystems, Thermo Fisher Scientific). The standard analysis protocol provided by the manufacturer was used. The RNA concentration was set to 250 ng in 20 µl solution. Reactions were treated using a PCR-block in the following way: 60 min incubation at 37 °C, stop reaction 5 min at 90 °C and then stored at 4 °C.

Quantification of relative gene expressions were conducted using a real time quantitative PCR system (StepOnePlusTM Real-Time PCR System, Thermo Fisher Scientific) and TaqMan Gene Expression Reagents (Applied Biosystems Inc, USA). Experiments were run in duplicates with 20 µl reaction volume and RNA negative controls. Results were normalised to triplicates of GAPDH endogenous controls (Glyceraldehyde 3-phosphate dehydrogenase, Hs99999905_m1 GAPDH). Each reaction tube contained 10 µl 2X TaqMan universal PCR master mix (Applied Biosystems Inc, USA), 1 µl probe solution, 4 µl sterile water and 5 µl cDNA (corresponding to 10 ng RNA). During the first experiment round 5 µl sterile water and 4 µl cDNA (corresponding to 8 ng RNA) were used. The following genes were monitored using apposite probes: Osterix (Hs00541721_m1 SP7), RUNX-2 (Hs00231692_m1 RUNX2), Osteocalcin (Hs01587814_g1 BGLAP), Collagen type

1 (Hs00164004_m1 COL1A1), DMP-1 (Hs01009391_g1 DMP1) and Sclerostin (Hs00228830_m1 SOST). The PCR cycle used is reported in Table 3.3.

Table 3.3: PCR amplification cycle

Incubation stage	2 min	50 °C
	10 min	95 °C
Amplification stage (40 cycles)	15 s	95 °C
	1 min	60 °C

3.8 Alizarin red staining (ARS)

Two 96-well metal scaffolds were seeded, one cultured in GM and one in OM. These were cultured in parallel to and in the same manner as the 24-well metal scaffolds of subsection 3.7.1. At day 21, the cells were fixed with formalin in PBS (3 %, 15 min, on ice). The scaffolds were then washed both with PBS and with H₂O, before being incubated with Alizarin red stain (ARS, 40 mM, pH= 4.2, 1 h, RT). After staining, 10 washes in H₂O were performed before scaffolds were incubated in PBS (15 min, RT). Pictures were taken in an inverted light microscope (Olympus CKX41, Olympus Corporation) with a mounted SLR camera (Olympus E-620, Olympus Imaging Corp).

Scaffolds were subsequently destained using cetylperidinium chloride (CPC, 10 % (*wt/vol*)) in sodium phosphate buffer (10 mM, pH= 7, 1 h, RT). The supernatant was transferred to a 96-well plate and scanned in a Microplate Absorbance Reader (570 nm, iMarkTM, Bio-Rad Laboratories, Hercules, California, USA).

Results

In this chapter, the results and knowledge gained from performing the experimental work described in chapter 3 will be presented. The sections will follow more or less chronologically the sequence in which the experiments were performed. The manufactured scaffolds will first be characterised, then the focus will shift to the cell work and its results. Where relevant, literature pertinent to the results will be cited and compared in order to provide an overview of results achieved by other experiments.

4.1 Scaffold characteristics

4.1.1 Surface characteristics

As expected and mentioned in the introduction, Chapter 1, PBF processes suffer from a weakness where powder particles in the vicinity of the energy beam path will partially melt into the cross section of the components. The scaffolds used in this thesis are no exception, as Figure 4.1 clearly showed the formation of a rough skin constituted by partially melted particles on every surface. The skin formation found on the manufactured scaffolds is further in accordance with other literature, such as Yan et al. (2012). The geometrical agreement between the CAD design and the manufactured scaffolds was simply measured in ImageJ, by extracting the pore diameter of a randomly selected pore. Results show a good geometrical agreement, with a variation of $\sim 80 \mu\text{m}$. The surface roughness was not scientifically characterised in this study, anyhow, a rough calculation using ImageJ yielded values close to $50 \mu\text{m}$. This value is in line with the roughness expected from the EBM process, as extensively elaborated by previous studies (Ek et al. (2016)). The roughness at lower magnitudes ($\ll 50 \mu\text{m}$) did not seem to be particularly pronounced. Figure 4.2 shows surface cues in the range of $1 - 5 \mu\text{m}$.

4.1.2 Mechanical characteristics

A CAD model of the small scaffold was imported into the simulation application on SOLIDWORKS and a static simulation was conducted as described in section 3.1. The scaffold was

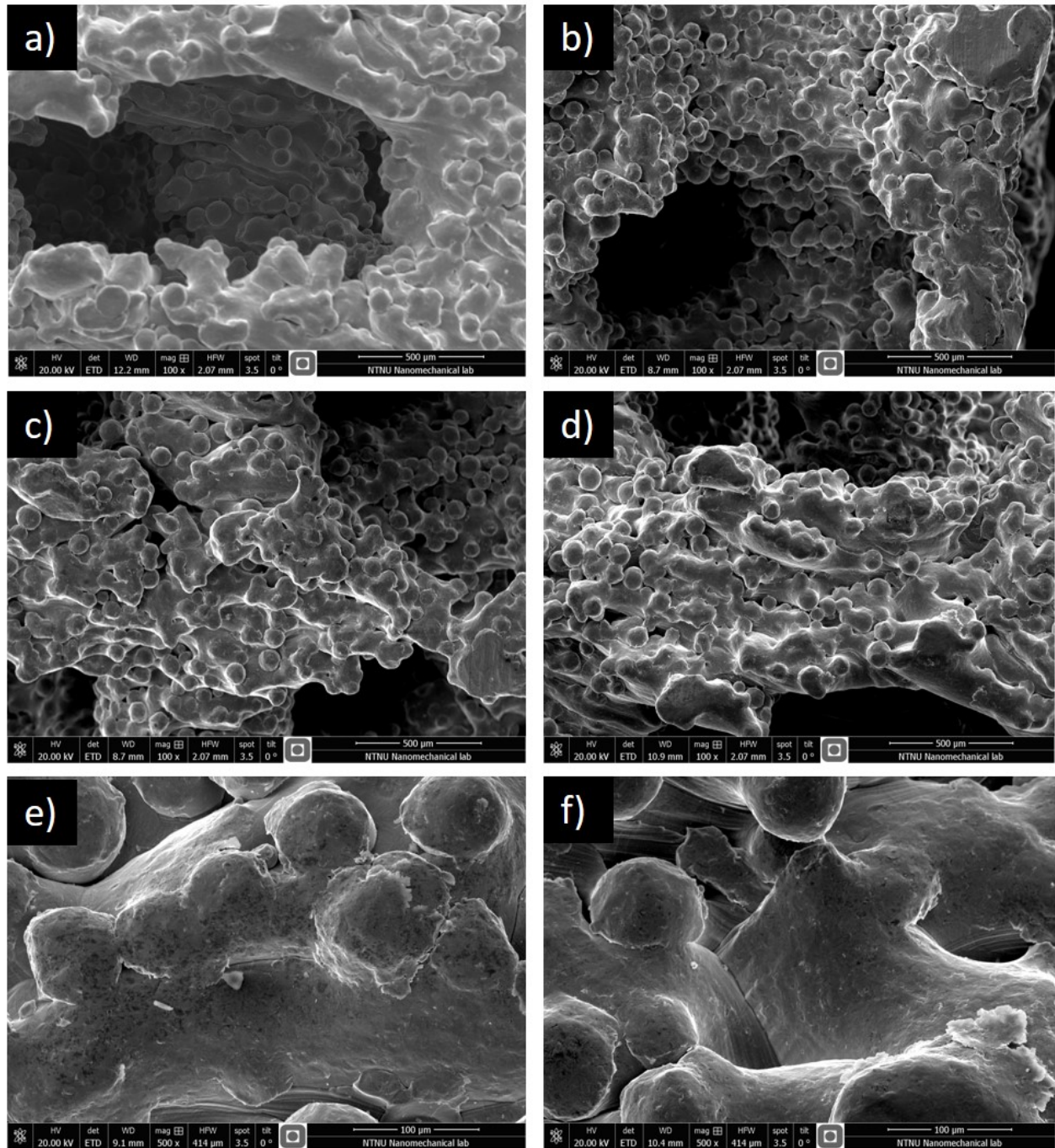


Figure 4.1: Surface characterisation by SEM

Figure showing SEM images of randomly selected scaffolds. Images a) to d) are taken at 100X, while images e) and f) are at 500X. The first row (a)-b) depicts the inherent geometrical porosity in addition to the scaffold's second strut-layer, clearly visible in image a). Second row (c)-d) shows in detail the morphology of the struts, while the third row (e)-f) shows a close-up on the partially melted particles.

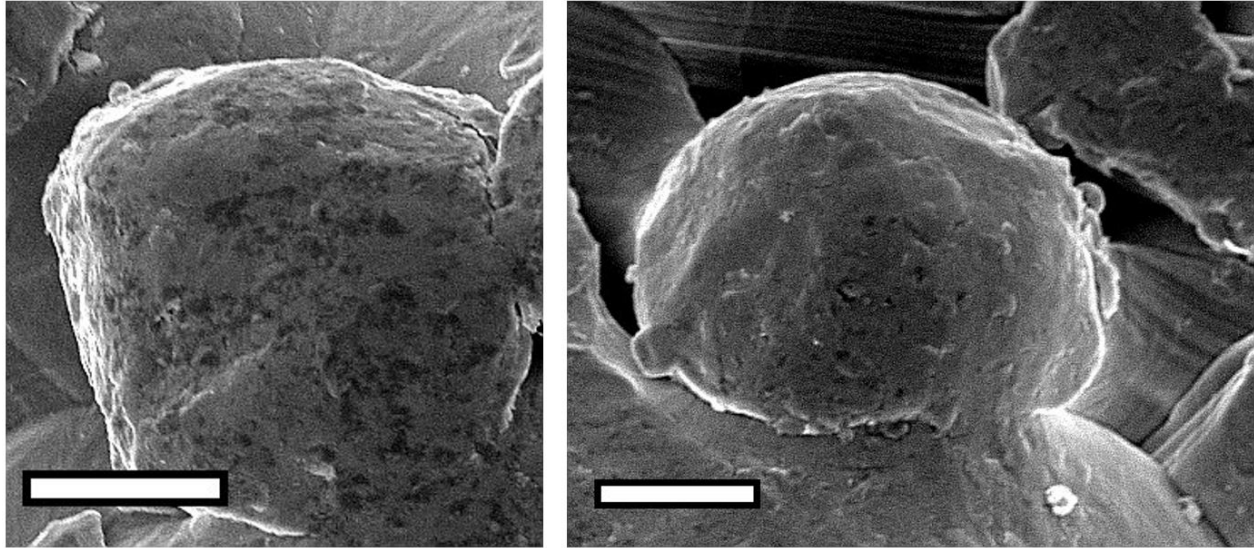


Figure 4.2: Grains close-up

Close up images of powder grains partially melted to the surface. Micro topography on the grain surface seems to be in the scale of a few microns. Scalebars are set to 30 μm , the average size of BMSCs.

modeled between two massive blocks, and them meshed. A displacement of 0.01 mm was applied on one end, while the other was fixed. The simulation setup is shown in Figure 4.3 and simulation details are reported in Appendix B section .5. The reaction force of 930 N was subsequently extracted and input to Equation 3.1, yielding 16.5 GPa as the Young's modulus. Compression tests were run as described in section 3.1. The scaffolds were placed between two compression plates in an apposite material testing machine and a compression ramp was applied of 0.1 mm/min until 3000 N were reached. The raw data (Figure 4.4, black line) reported an elastic modulus of 7.9 GPa, which is much lower than the simulation values. The compression area was calculated by image analysis in ImageJ, here shown in Figure 4.5. The area reduction factor (f_{area}) was found and input to Equation 3.2 together with the reaction force from the compression test. The resulting Young's modulus is plotted in the same figure (red line). The flattening of the curve occurring during the final parts of the test was used as basis for the calculation of a numerical modulus, yielding a stiffness of 12.9 GPa (S.D. 0.35 GPa).

By comparison of the results from the simulation and the compression test, quite a large numerical discrepancy was found, which may be due to various factors. These will be discussed more in detail under chapter 5, as new testing methods need to be defined.

The stiffness of the manufactured scaffolds was nonetheless in the range of trabecular bone, in accordance with the literature, such as Rho et al. (1993).

4.2 Adhesion

BMSCs were seeded and cultured as described in subsection 3.4.1 before they were stained at the preset time points (8 h, 16 h, 24 h, 48 h). Images are shown in Figure 4.6 and Figure 4.7.

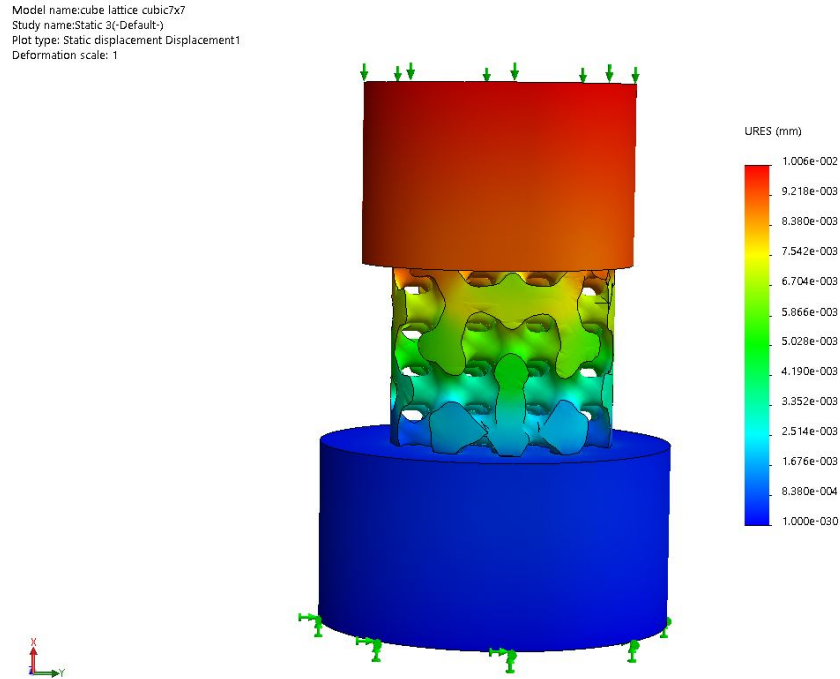


Figure 4.3: FEA static compression setup

The scaffold was modeled between two massive blocks. The geometry is fixed at the bottom (green details) and a compression of 0.01 mm is applied to the top (green arrows).

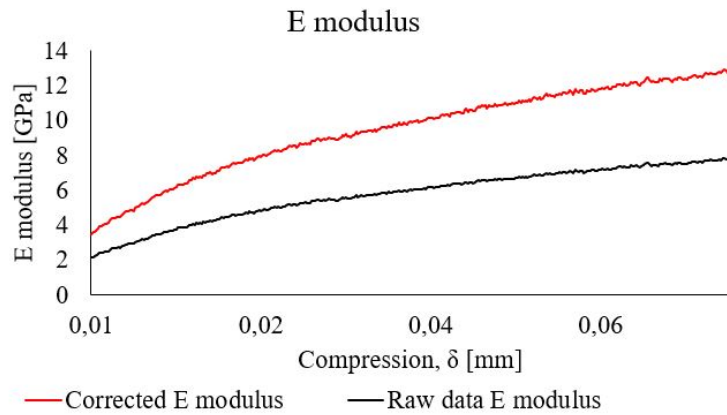


Figure 4.4: Young's modulus of the scaffolds

Graph of the changing E-modulus [GPa] with respect to the displacement [mm]. The final modulus is extracted from the final 50 data points, as the graph seems to flatten out. The black line reports the raw-data values, while the red line shows the corrected results when the area reduction constant is input.

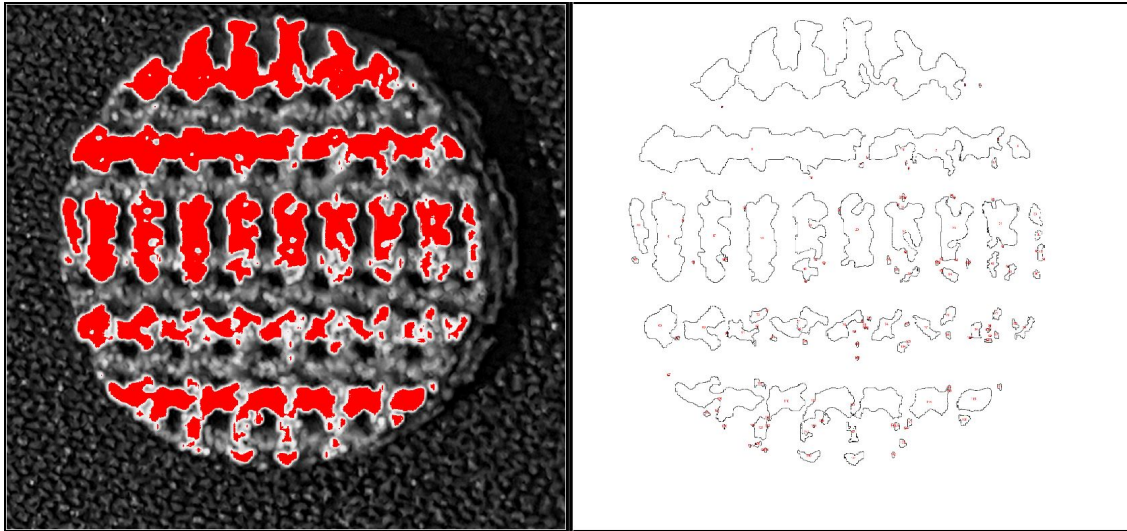


Figure 4.5: Surface contact area reduction

Figure showing a graphical depiction of the area in contact with the crossheads during compression (red, left) and particle analysis result (right).

When looking at the images, it is important to keep in mind the high variation in surface height of the individual scaffold within each image. The image and cell morphology may appear flat, but it is in reality covering rounded struts and other surface formations easily distinguishable in Figure 4.1. The figures were created, as previously described (subsection 3.4.1) by the stacking of several planes of focus over one another. Each image is a representation of the cell morphology several hundred microns in depth. Cells adhered to the vertical parts of the scaffolds are difficult to distinguish, as only a thin cross section may be captured.

The images shown were taken from representative parts of each scaffold and similar cell morphologies were found on the remaining scaffold areas.

As expected, few cells were adherent at the first time point (8 h). Especially the top strut layer is showing a low number of cells with a limited morphological spreading. The second strut layer shows better tendencies, as the cell morphology seems to be more spread with higher cell numbers. The staining of the nuclei seems to be highly concentrated at this time point and constrained to only the cell nucleus, especially when compared to later time points.

At the 16 h mark, more cells were found to be adherent on the surface. Not many differences in cell morphology were found between the top and inner layers. The higher amount of cells present on the top scaffold layer may also be attributed to a higher amount of focal adhesions in each cell, resulting in stronger adhesion. The overall morphologic spreading seems greater compared to the cells fixated at the 8 h mark. The stain seems to have stained some of the RNA as well, commonly known as unspecific staining. This is an effect also present in the previous adhesion experiments (section .3).

The scaffold fixed after 24 h incubation provided a surprising result, as almost no cells were present. The few cells that were visible did not seem to be as spread as in the previous images and the nuclei did not appear to be unspecifically stained. The discussion will provide further insight on the possible causes for this result.

After 48 h of incubation the results appeared to be back on track, with an extensive spreading of the BMSC morphology. Especially the second layer presented vastly spread and interconnected cytoskeletons. The nuclei appear highly pronounced and RNA spread throughout the cells appeared also to be stained, which is again indicative of unspecific staining. The morphology on the uppermost strut layer appeared to have slightly fewer cells compared to the morphology after 16 h incubation, an occurrence that may be connected to the various wash cycles.

Common for all scaffolds was the selective BMSC adhesion to only the top surfaces on each layer. Only a few cells were found to adhere to the backside of the struts (not shown), which may be due to the static culture conditions. All of which will be thoroughly discussed in the next chapter.

4.3 BMSC activity over the course of 9 days

After being seeded with cells, the scaffolds were incubated and alamarBlue® assays were conducted at multiple preset time points. Results are shown in Figure 4.8.

As one would expect, the cell activity was low at the starting point and increased over time.

The sudden spike at day seven was attributed to technical reasons with a longer incubation time during the assay. Due to an inherent assay linearity (Rampersad (2012)) it was possible to scale the results in order to compare it with the other time points. As every cell reduces a constant amount of stain over a set time, the expressed results are linearly dependent only on the incubation time. By scaling the assay time from 2.5 h to 2 h (dotted lines), we get a more realistic curve.

By looking at the curves, it is clear that the cellular activity increased at an earlier time point for the BMSCs cultured in OM. As an increase in cell activity is often associated with the onset of the differentiation process, the stable upregulation may indicate that the BMSCs cultured in OM have an onset of differentiation after 48h. The cells cultured in GM show a similar increase between 72 h and 5 d after seeding. (section 4.4, section 4.5 and section 4.6), it may be possible to postulate a more specific conclusion.

4.4 ALP expression

At day 10 cells were fixed and stained for ALP, Figure 4.9. ALP stains green, whereas the nuclei are shown in red. Where the image is in focus, and the cross section of the cell is imaged (close to the centre of each image) one can clearly see the presence of ALP on the areas surrounding the nuclei. Other cells residing at different distances from the lens, hence out of focus, appear as yellow areas. Here the ALP was probably present on the cytoskeleton covering the underlying nucleus, hence the yellow colour. A stronger ALP signal was found in the cells cultured in OM, however, also the cells cultured in GM displayed an ALP signal.

4.5 PCR analysis

BMSCs were cultured as described in subsection 3.7.1. After lysing the cells, extracting RNA and performing cDNA synthesis, PCR was performed as described in the same section. Table 4.1 shows the RNA concentration present in each sample after RNA extraction.

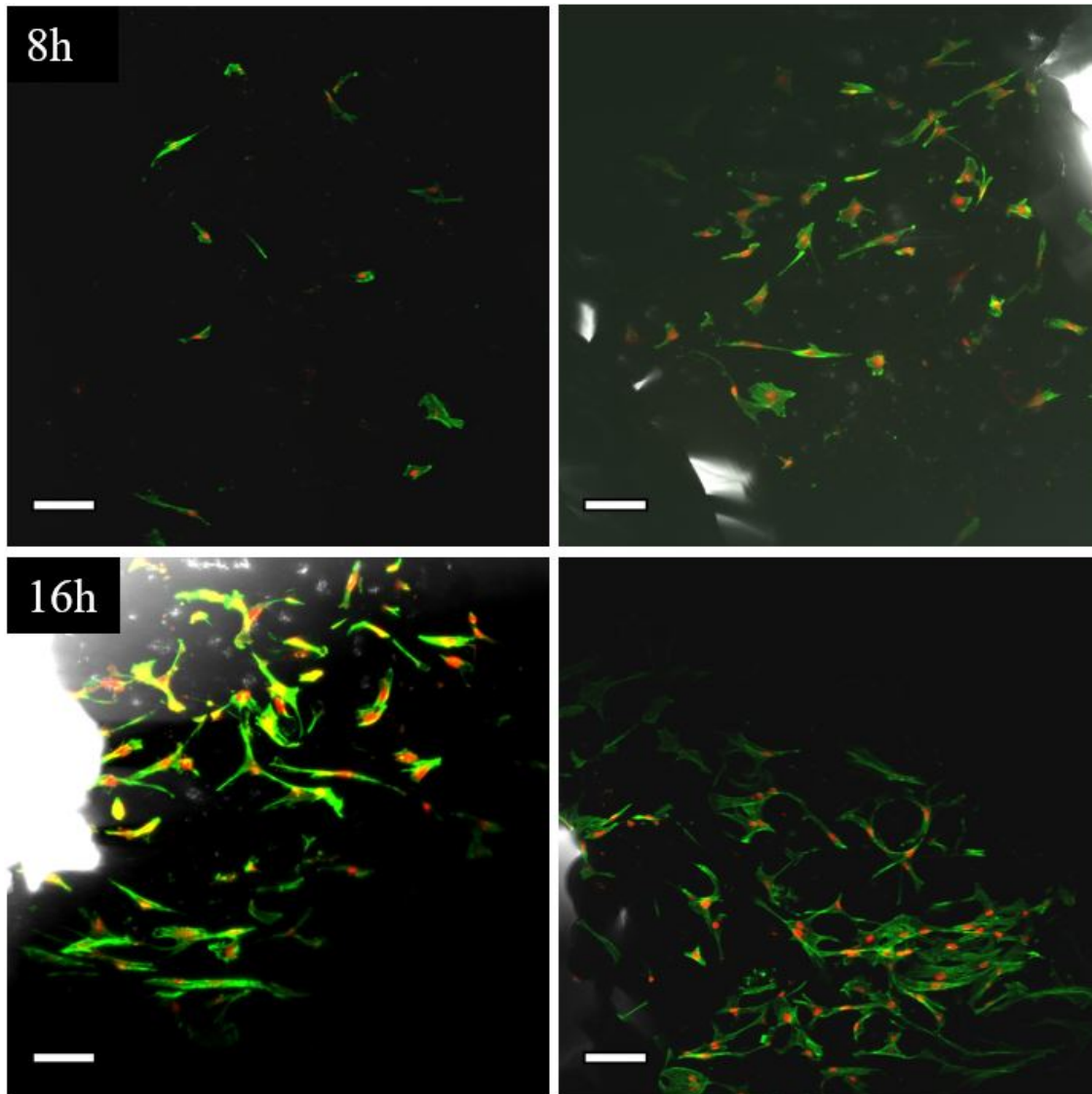


Figure 4.6: 8 h and 16 h adhesion results

BMSCs on scaffolds at 8 h (top) and 16 h (bottom) to a pair of small scaffolds, imaged at the first strut layer (left) and at the second strut layer (right). The cytoskeletons are stained with Alexa Fluor® 488 Phalloidin (green) and the nuclei are stained with Draq5TM 633 (red). White reflections are due to the light passing through the scaffold at the site of a pore. Scalebars are set to 100 μ m.

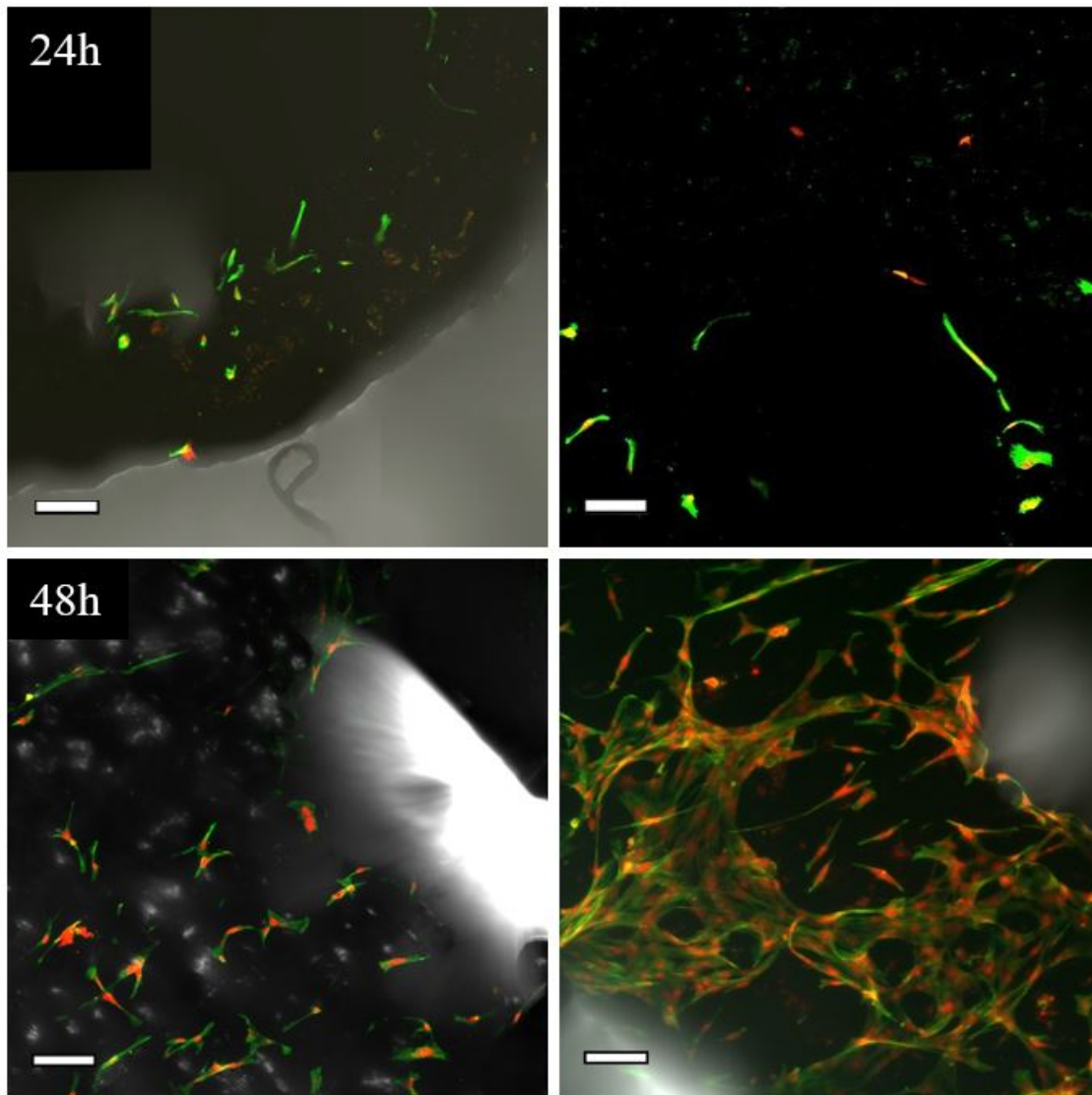


Figure 4.7: 24 h and 48 h adhesion results

BMSCs on scaffolds at 24 h (top) and 48 h (bottom) to a pair of small scaffolds, imaged at the first strut layer (left) and at the second strut layer (right). The cytoskeletons are stained with Alexa Fluor® 488 Phalloidin (green) and the nuclei are stained with Draq5™ 633 (red). White reflections are due to the light passing through the scaffold at the site of a pore. Scalebars are set to 100 μm.

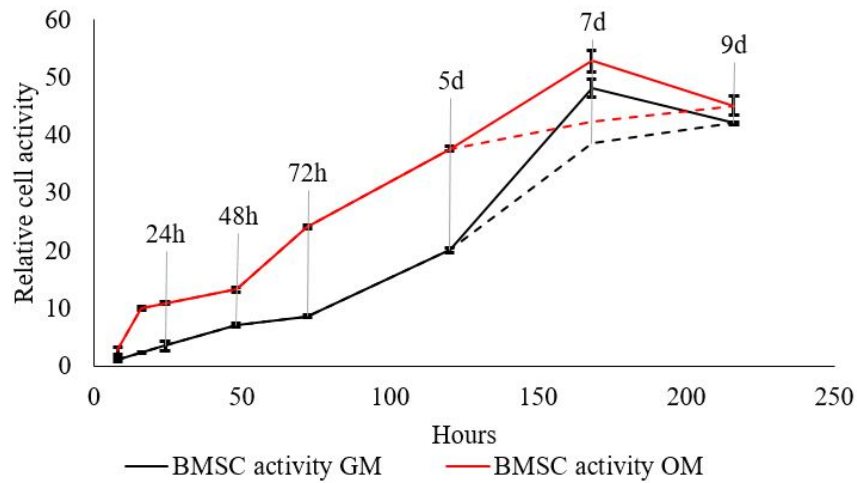


Figure 4.8: alamarBlue® results

Graph showing the alamarBlue® assay results. Adsorption of medium from cells grown in GM (black) and cells grown in OM (red) are normalised with respect to the first reading. Dashed lines show the time corrected curve for the assay at day 7 which was incubated 2.5 h instead of 2 h. Readings from the controls have been subtracted at each reading and standard deviation is calculated using Equation 3.3.

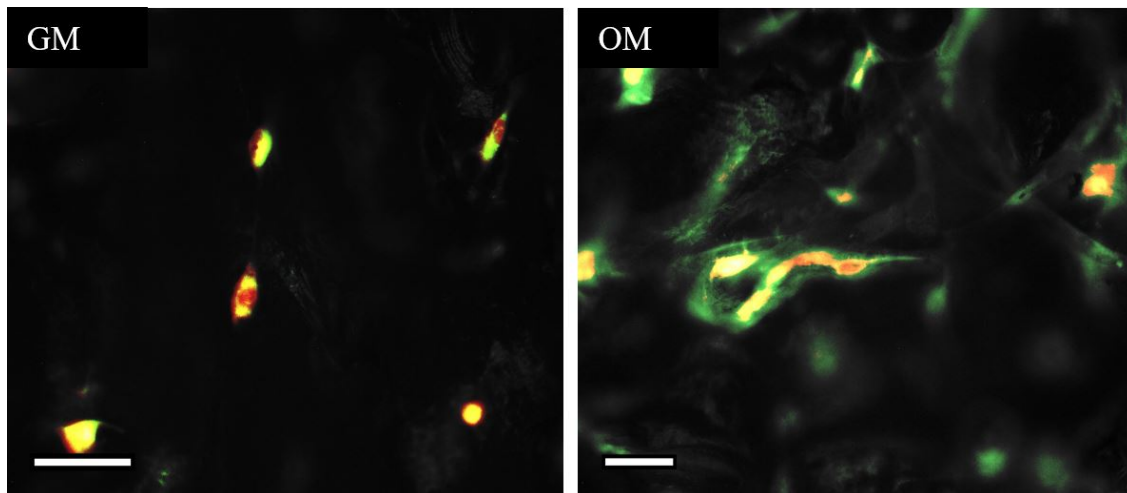


Figure 4.9: ALP staining

Microscopy characterisation of ALP stained (green) cells on scaffolds cultured in GM and OM. Nuclei are stained with Draq5® (red). In the areas where the two channels overlap the colour is yellow. The image on the left is from a scaffold cultured in GM, while the right image is from a scaffold cultured in OM. Scalebars are set to $\sim 100 \mu\text{m}$.

Table 4.1: RNA concentrations retrieved from the spectrophotometer.

	Sample ID	RNA conc. [ng/ul]	Sample ID	RNA conc. [ng/ul]
Round 1	BMSC D0	432	BMSC D0	1345
	OM D7	35.29	GM D7 2D	87
	GM D7	12.8	OM D7 2D	15.2
	OM D14	28.2	GM D7 3D	30
	GM D14	39.8	OM D7 3D	60.1
	OM D21	27.9	GM D14 2D	283.4
	GM D21	37.2	OM D14 2D	269.3
Round 2			GM D14 3D	55.5
			OM D14 3D	36.1
			GM D21 2D	213.5
			OM D21 2D	274.1
			GM D21 3D	85.4
			OM D21 3D	59

The results from PCR are presented in the following subsections. As presented in subsection 1.1.2, the different genes expressed during osteogenesis should be upregulated at different stages in the differentiation process. This means that we expected Collagen type 1 and RUNX2 to be expressed at an early stage, followed by Osteocalcin and Osterix in the osteoblast phase, before Sclerostin and DMP1 should have been expressed at a later stage.

Some data points are missing from the plotted curves in the next graphs. This is due to a couple of reasons: Firstly, if a large standard deviation was present among duplicates it was not possible to extract reliable data. Secondly, due to the 40 amplification cycles used during PCR, the genes would appear at different cycle numbers. If a signal was detected after cycle 35.5, it may not necessarily be because of the probed gene, but rather because of other influencing factors exerting a signal after a long incubation at a high temperature. Genes expressed after cycle 35.5 were hence omitted from the results. Finally, if the gene itself was not present in the reaction volume, no data point could obviously be extracted.

As all figures in this section were formatted equally, a brief explanation on how to interpret the graphs is given in the following: Red lines represent the expression from BMSCs cultured in osteogenic medium (OM), while the black lines indicate the expression of cells cultured in growth medium (GM). Results from BMSCs cultured in round 1 and 2 are respectively labelled as R1 and R2. The graphs from R2, depicting results from 3D and 2D scaffolds, can be compared to each other as they were run in the PCR machine simultaneously on the same plate. Results from R1 were gathered at an earlier time point, and must be regarded as a separate set of results.

4.5.1 Generally higher gene expression for 2D cultured cells

Collagen type 1 (COL1) was described in the introduction to be an osteoblast marker, as these cells secrete a matrix containing this gene. If the BMSCs were differentiating, we would expect an increase in this gene over the 21 days of culture. However, the results given in Figure 4.10 tell

another story: The COL1 expression of cells cultured on the metal scaffolds was found to remain relatively unchanged until day 21. Whereas the cells cultured in OM on 2D scaffolds, had a peak expression the same day and were generally expressing higher values of COL1 throughout the culturing period.

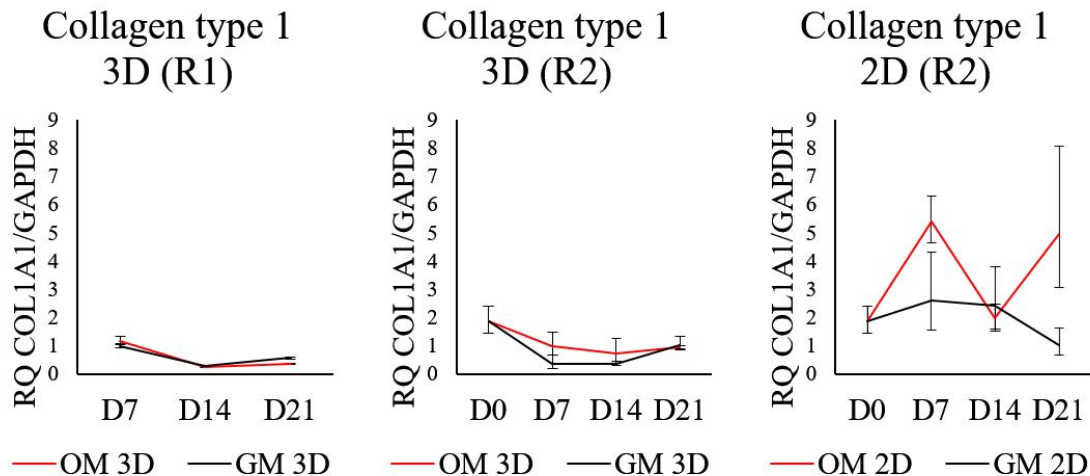


Figure 4.10: Collagen type 1 expression

Left and center: COL1 expression from BMSCs cultured on 3D scaffolds from round one and round two respectively. Right: COL2 expression from cells cultured in 2D conditions. Results from round 1 are normalised with respect to GM 3D D7 while round 2 results are normalised with respect to OM 3D D21.

Bruderer et al. (2014) describes the role of RUNX2 as a transcription factor controlling osteoblast differentiation. It is also acting as an osteoblast marker and is responsible for the regulation of other osteoblast differentiation genes. Finally, it also plays a role in the transactivation of the Osteocalcin gene. Results of the RUNX2 expression are given in Figure 4.11. Again, 2D scaffolds displayed generally higher levels of RUNX2. The only sign possibly suggesting osteoblast activity was seen for GM cultured cells in the first round (R1), as these cells displayed an upregulation of RUNX2 towards day 21.

As previously described, Osteocalcin is activated by the action of among other RUNX2. This is a gene found in mature osteoblasts and its presence is indicative of differentiated BMSCs. Osteocalcin results, presented in Figure 4.12, show higher Osteocalcin expression for 2D cultured cells than for their 3D cultured counterpart. However, an ascending trend was found for GM cultured cells on both the porous metal scaffolds.

Osterix is an osteoblast specific gene highly important to bone formation. In fact no bone generation is found to occur in Osterix deficient mice (Nakashima et al. (2002)). Figure 4.13 shows that Osterix was highly expressed at day 7, for the 2D cultured cells. Lower expressions were found in the porous metal scaffolds, with a slight upregulation towards day 21 for cells cultured in OM.

Sclerostin is regarded as an inhibitor of bone formation regulated by both RUNX2 and Osterix (Prez-Campo et al. (2016)). In our study, the downregulation of this gene is seen as positive for osteoblastogenesis on the scaffolds, while the upregulation indicates the end of this process. Sclerostin expressions were found to be decreasing for cells cultured in GM on 3D scaffolds, while

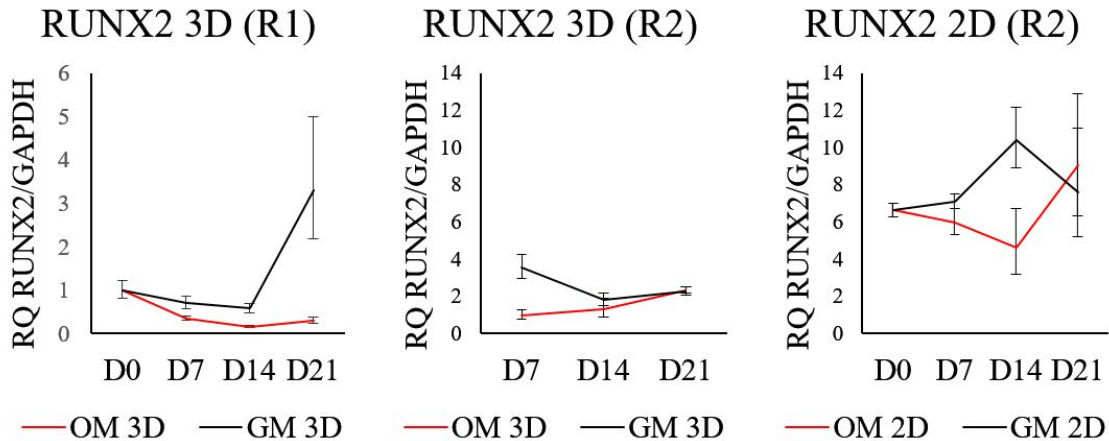


Figure 4.11: Runt related transcription factor 2 expression

Left and center: RUNX2 expression from BMSCs cultured on 3D scaffolds from round one and round two respectively. Right: RUNX2 expression from cells cultured in 2D conditions. Results from round 1 are normalised with respect to D0 while round 2 results are normalised with respect to OM 3D D7.

their 2D GM cultured counterpart showed an increase towards day 14, as shown in Figure 4.14. An increase in Sclerostin expression towards day 21 was further found for cells cultured in OM on the porous scaffolds.

DMP1

The signal from the DMP1 gene did not reach significant results before cycle 35, which is expected if osteocytes were not present after 21 days of culturing.

4.6 Calcium deposition

BMSCs were cultured as described in section 3.8. After 21 d incubation, the cells were fixed and stained with alizarin red and subsequently washed. The results are presented in Figure 4.15.

Microscopy images of the scaffolds shows only a partial calcium deposition on the scaffold cultured in GM. The deposition seems to have been limited to the top layer on each side of the scaffold. A closer look shows a mineralised calcium formation along the edge and partially over the top of the struts. Stained cells were found adhering to the scaffold also internally. Values from the absorbance analysis after destaining with CPC show low concentrations of alizarin red for this scaffold, which is in line with the findings from the optical characterisation.

The scaffold cultured in OM displayed an extensive amount of mineralisation, although not on the top surfaces. Both the overview and the close-up images revealed a strong ARS signal originating from inside the scaffold. This signal originated from cells which were spanning the diameter of the pores. The same tendency was not found to be as strong in the GM cultured scaffold (green arrows). In addition to the displayed mineralisation, the same considerable cell bridging was observed between the OM cultured scaffold and the well, prior to transferring the

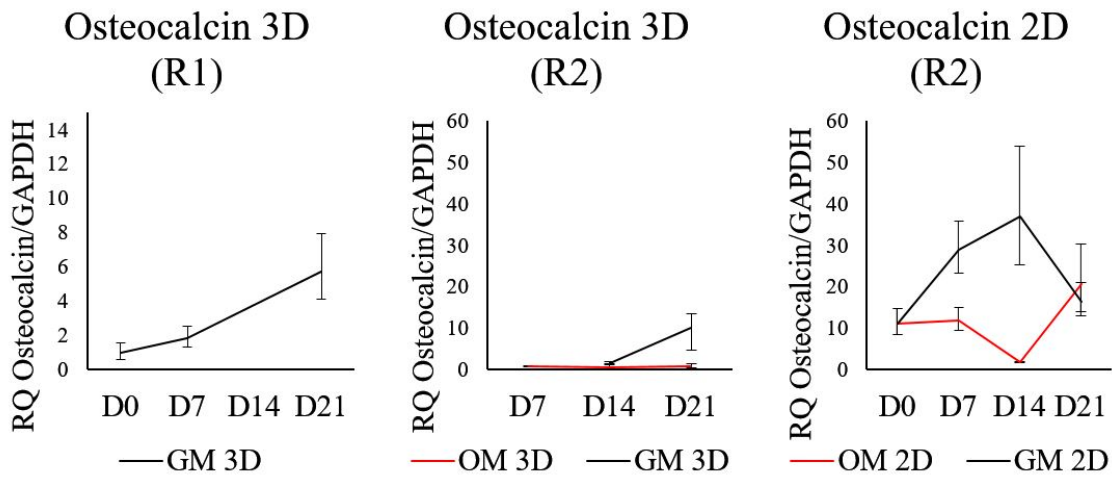


Figure 4.12: Osteocalcin expression

Left and center: Osteocalcin expression from BMSCs cultured on 3D scaffolds from round one and round two respectively. Right: Osteocalcin expression from cells cultured in 2D conditions. Results from round 1 are normalised with respect to D0 while round 2 results are normalised with respect to OM 3D D7.

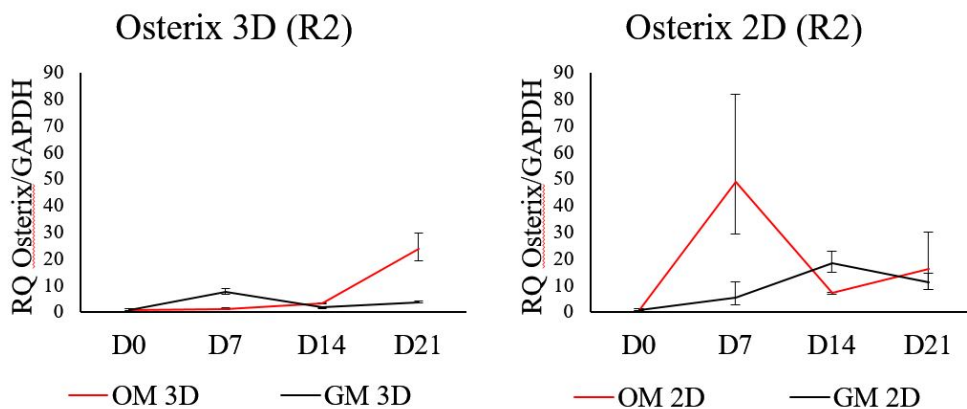


Figure 4.13: Osterix expression

Left and center: Osterix expression from BMSCs cultured on 3D scaffolds from round one and round two respectively. Right: Osterix expression from cells cultured in 2D conditions. Results are normalised with respect to D0.

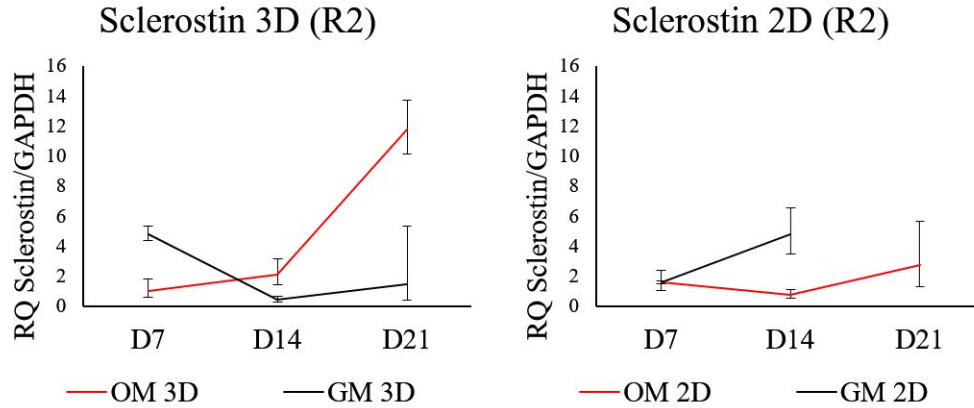


Figure 4.14: Sclerostin expression

Left and center: Sclerostin expression from BMSCs cultured on 3D scaffolds from round one and round two respectively. Right: Sclerostin expression from cells cultured in 2D conditions. Results are normalised with respect to OM 3D D7.

scaffold to a clean well prior to optical characterisation. The top layers did not seem to be stained to the same degree as the scaffold cultured in GM. The absorbance analysis revealed approximately 3 X the amount of mineralisation compared to the GM cultured scaffold, which seems to be in line with the visual findings.

After staining, elevated amounts of ARS were found on the bottom of the OM cultured well indicating mineralisation. The same was not found in the GM cultured well, which resulted completely clear after ARS staining.

As expected, the control scaffold does not display any mineralisation. Only the scaffold top is shown, as no variation was found compared to the scaffold bottom.

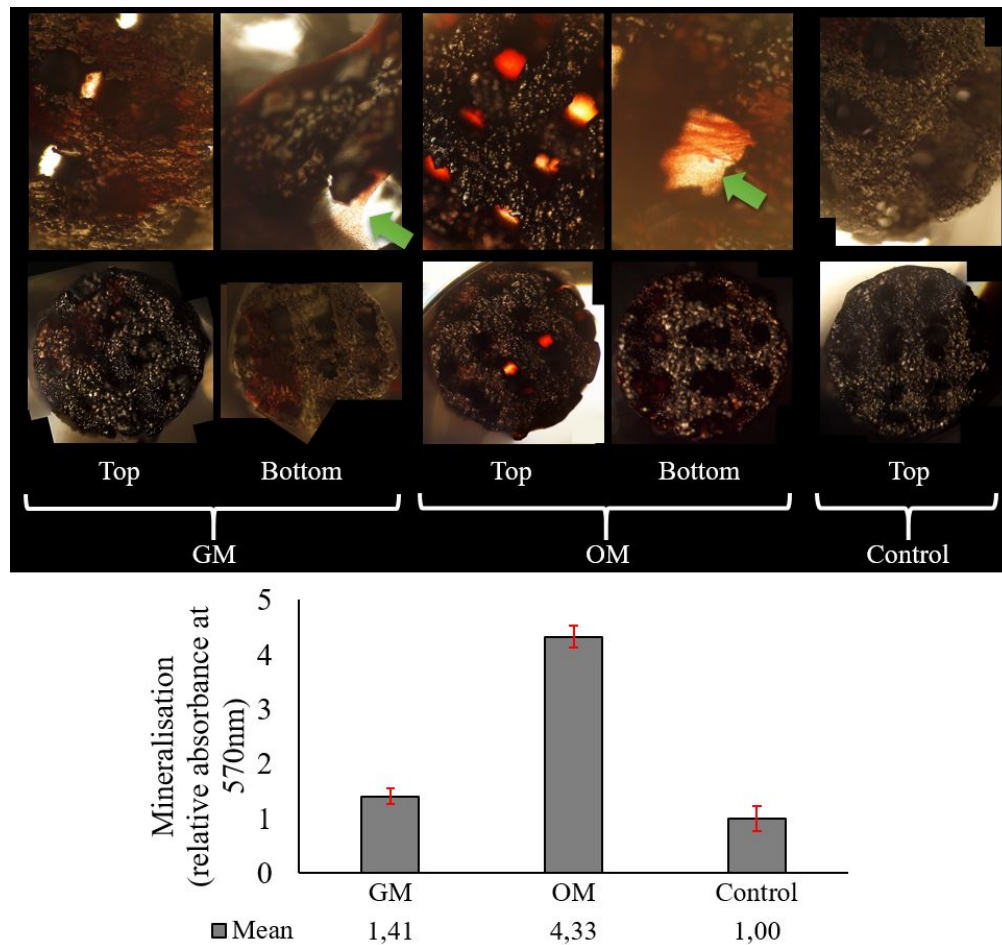


Figure 4.15: Alizarin red

Images: Calcium deposition (red staining) on three 96-well scaffolds. Images on the top row illustrate close-ups of the surfaces, while the second row illustrates composite images of the entire scaffold surface. From left to right: Scaffolds cultured in GM, OM and a BMSC free control. Green arrows indicate the cells spanning the pores.

Graph: Calcium concentration reported as relative absorbance for the three destined scaffolds. Absorbance values are normalised with respect to the control scaffold. Error bars depict standard deviation over quadruple measurements.

Discussion

In this study, porous Ti-6AL-4V scaffolds were designed and manufactured by EBM. These were seeded with BMSCs and *in vitro* cultured in both osteogenic and growth medium. Specific cell processes were characterised to assess the hypothesis presented in chapter 2:

”Additive manufactured porous Ti-6AL-4V scaffolds are both osteoinductive and osteoconductive.”

The motivation behind this study was to generate additional knowledge for future design of arthroplasty implants. As presented in the introduction (chapter 1), the number of bone remodelling surgeries is increasing worldwide due to different factors. Younger patients are receiving these implants, which means that an increased implant lifespan is also required.

Introducing AM in the field of implant manufacturing, enables the production of porous and softer metal implants. Softer implants have the potential to reduce the onset of stress shielding commonly associated with osteopenia, a condition leading to numerous resurgeries (Li et al. (2016)).

Cells responsible for the osteointegration of implants, i.e. BMSCs, prove to be influenced by the surfaces they come in contact with. The introduction of structures and roughness’s resembling the ECM environment commonly expressed by porous bone, can influence these cells to begin bone deposition. Hence, by manufacturing scaffolds with a porous structure and tailored surface roughness suitable to constitute the bone-to-implant interface in future implants, one can assess the osteoinductive and osteoconductive properties of such structures in the laboratory.

5.1 Osteoconductivity of structures

Results presented in chapter 3 show overall good tendencies regarding cell survival. This is an important part of osteoconductivity, which was defined in chapter 1 as *”the implant material’s ability to support biological activity in the form of bone in-growth on the surface.”* In general, Ti-6Al-4V is regarded as a highly biocompatible material. The formation of a passive oxide layer on the

material surface generates a ceramic-like material structure which is beneficial to the cytocompatibility (Mikulewicz and Chojnacka (2011); Sidambe (2014)). The passive oxide layer is easily maintained in in-body pH conditions and results in low formation of ions and low reactivity with other molecules.

Activity of the seeded BMSCs was tested by alamarBlue® staining as described in subsection 3.5.1. Here, two scaffolds were seeded with BMSCs and cultured 9 days in GM and OM while multiple assays were run at preset intervals. The results showed an increased cell activity in both mediums over the course of nine days (Figure 4.8). This is a result that further suggest both the material and the scaffold to be bioactive, favouring cell-matrix interactions. This is a result which is also agreeing with the findings of Cheng et al. (2014): They tested viability of an osteosarcoma derived cell line in porous titanium scaffolds and compared them with viability on 2D scaffolds. High cell survival and no significant viability variation was expressed with the various pore dimensions on the 3D scaffolds.

Another important aspect of osteoconductivity is the capacity to sustain the adhesion of BMSCs. Adhesion to ECMs plays an important role in cell signalling. As presented in the introduction, surface characteristics prove to influence both the proliferation and differentiation process, but not so much the adhesion phase (Kolind et al. (2014)). However, the study conducted during the pre-master project, Appendix section .3, does show surface related tendencies influencing adhesion. Conclusive results were however not obtained during that study. Surface dependent adhesion still needs further studies.

During our experiments, the adhesion was characterised by confocal microscopy of stained BMSCs. The results presented in section 4.2 provide a multifaceted story regarding the adhesion. On the one hand, cells require some time in order to adhere to a substrate, consequently, not many cells have adhered at the 8 h time point. Subsequent time points (16 h and 48 h) show an increased number of adhered cells. These have had more time to generate a higher number FAs to the underlying ECM resulting in the formation of a stronger bond. The time points discussed here are in line with the expectations: showing a wider spread cell morphology and an increasing cell number with an increased incubation time. On the other hand, the scaffold incubated 24 h shows few adhered cells. This can be attributed to a number of causes: Regarding cytocompatibility, one would assume the material to have become toxic. However, the presence of some adhered cells must mean that they were alive at the time of fixation, thus indicating that the material itself may not be the culprit. Additionally, during the fixation, permeabilisation and staining process, multiple wash cycles may be responsible for the removal of cells having fewer/weaker adhesive connections. A combination of the performed wash cycles and difficulties during the seeding process (thoroughly discussed in section 5.3), is believed to have contributed to a lower amount of adhered cells.

When viewing the cell activity results in light of the adhesion results, an important point is raised: The lower amount of adhered cells after 8 h suggests weaker cell-scaffold bonds, which probably lead to cells being detached and removed during the removal of medium and the subsequent wash cycles. During the alamarBlue® the medium was also harvested after 8 h, it is therefore safe to assume that some cells were also forcibly removed due to the perturbations in the medium following this action. This may have influenced the outcome of the subsequent alamarBlue® stainings, if fewer cells remained on the scaffolds for the assay at 16 h. One cannot but wonder if the cell activity would have been higher throughout the 9 d experiment, if the first assay was to be

conducted at 16 h instead of 8 h.

Supporting the notion that scaffolds are cytocompatible, there is a stable cell yield of the remaining seeded scaffolds. These scaffolds supported BMSC development up to 21 days. Furthermore an overwhelming amount of literature supporting the use of Ti-6Al-4V as a biomaterial (e.g. Sidambe (2014)), making the seeding complications a more plausible culprit for the low cell yield after 24 h.

Finally, in order to determine the scaffold's osteoconductive properties, we are looking to find osteoblastogenesis and calcium deposition. These processes are highly related to bone formation and thus to osteoconduction. A combination of the gathered results are taken under consideration to assess the latter:

When looking at the cell activity during alamarBlue® staining in Figure 4.8, a rapid activity increase after 48 h is seen for the cells cultured in OM. Such an increase in activity is often, although not conclusively, attributed to the onset of differentiation.

Secondly, an ALP staining was performed to assess whether BMSCs differentiated towards osteoblasts on the scaffolds. The cells cultured in OM are relevant for this part of the study. These cells expressed a large amount of ALP after 10 days, thus suggesting an onset of differentiation towards osteoblasts. ALP mineralisation nodules typically occurring during ALP staining were however not found, which is probably due to the low magnification objective used during imaging. However, the extensive ALP expression in these cells is an indicator of osteoblastogenesis.

Thirdly, PCR was used to quantify the gene expression from the cells in different culturing environments, i.e. 2D and 3D scaffolds, as described in subsection 3.7.1. In short: cells were seeded on both 24-well scaffolds and normal 2D wells. Two experiments were conducted at different time points to assess the repeatability of this experiment. The cells on selected scaffolds were harvested every seven days over a three week incubation period. The RNA from the cells was extracted and cDNA was synthesised before performing PCR.

An overall lower gene expression of osteogenic genes was found on BMSCs cultured on 3D scaffolds compared to cells cultured in 2D conditions. This is indicative of a lower scaffold conductivity, which is in direct opposition to the tested hypothesis. This may however be attributed to the amount of cells extracted from the scaffolds: The lysing buffer was not able to properly lyse all the cells present on the 3D scaffolds, as microscopy inspection post-lysis revealed remaining adhered cells especially inside the pores. Quantification of RNA concentrations in a spectrophotometer confirms this suspicion (section 4.5, Table 4.1), as the RNA concentrations extracted from 2D scaffolds are several times higher compared to the RNA extracted from 3D scaffolds. Potentially, this means that differentiated cells may have been left in the porous scaffolds. Their genetic expression may therefore be missing in the PCR analysis.

If we isolate the results from the 3D scaffolds presented in section 4.5, thus only comparing the gene expression between OM and GM, we see a slight increase in RUNX2 towards the end of the 21 day culturing period for GM cultured scaffolds. The same effect can be seen for the expression of SP7 (Osteocalcin), which increases throughout the culturing period. Both these results are indicative of osteoblast differentiation. A delayed onset of RUNX2 was also reported by Sollazzo et al. (2011), who cultured BMSCs on trabecular titanium scaffolds in non osteogenic medium. Osteocalcin was also reported to be upregulated after seven days of culturing.

The expression of OSX (Osterix), a highly important bone formation gene, is upregulated for both 2D and 3D scaffolds cultured in OM, indicating the presence of osteoblasts. An upregulation

of Sclerostin, especially for OM cultured 3D scaffolds suggest a possible downregulation of bone deposition towards the end of the 21 day incubation.

In general, the results obtained from the PCR analysis are inconclusive as clear trends pointing towards osteoblastogenesis are not found. The exceptions to this observation are the increasing expressions of RUNX2 and Osteocalcin by the GM cultured 3D scaffolds over the course of 21 days. However, an overall high standard deviation makes a definitive conclusion questionable.

Lastly, final evidence of BMSC differentiation and bone deposition is provided by the alizarin red staining (ARS) results in Figure 4.15. ARS is currently the most used test to prove an onset of differentiation and bone-deposition, as defined by Dominici et al. (2006). Results show a substantial degree of mineralisation for scaffolds cultured in OM. As this is a basic assay that directly binds to the deposited calcium present both on the scaffolds and in the cells and given the fact that no staining is present on the control scaffold, it is clear that osteoblastogenesis to some degree must have occurred on the porous scaffolds. This is an important result which is also supported by the results from the ALP staining and the increase in cell activity. It is however to some degree in contrast with the PCR results, which means that further investigation is needed to understand the result discrepancy between tests.

Having analysed all the results, a multifaceted result landscape emerges: On the one hand, results from the alamarBlue® assays, the ALP staining and the ARS staining unanimously indicate an onset of differentiation and also bone deposition. On the other hand, the PCR results does not provide strong evidence for the osteoconduction of the scaffolds.

5.2 Osteoinductive traits of scaffolds

While having discussed that the scaffolds seem to be osteoconductive, we still haven't reviewed the osteoinductive properties of the structures. Osteoinduction was previously defined in subsection 1.1.1 as *"the process in which the material is capable to stimulate BMSCs to differentiate into osteoblasts."*

When cultured in OM, BMSCs are influenced to differentiate by osteogenic factors present in the medium. This means that whether the scaffolds are osteoinductive or not, the cells will likely still undergo osteoblastogenesis if the right culturing conditions are present. This was also shown in Kolind et al. (2014), as dental pulp stromal cells (DPSCs) cultured in OM did not express significant variation in the mineralisation among different surface topographies. If however the BMSCs are cultured in a non-osteogenic medium, i.e. GM, it is up to the ECM environment to promote the onset of differentiation.

Other authors have previously attributed osteoinductive properties to porous AM titanium structures, as presented during the introduction (chapter 1):

Faia-Torres et al. (2014, 2015) and Kolind et al. (2014) found 2D scaffold roughness in the micrometer scale ($\sim 1 - 2 \mu\text{m}$) to be favourable for inducing osteoblastic differentiation of femur derived mesenchymal stem cells and DPSCs respectively cultured in non-osteogenic mediums (NOM).

Li et al. (2016) and Cheng et al. (2014) studied porosity dependent osteogenesis of namely BMSCs and MG63 cells on 3D scaffolds cultured in NOM. They found pore sizes of respectively $300 - 400 \mu\text{m}$ and $653 \mu\text{m}$ to be best suited for the job.

Sollazzo et al. (2011) also studied osteogenesis of BMSCs cultured in NOM, on porous trabecular additive manufactured scaffolds with 800 μm pores. Their results show an induced osteogenesis with a delayed expression of RUNX2. The author argues that the osteogenesis was induced by other genes, namely FOSL1, SPP1 and ALPL.

The scaffolds used in this thesis were, as previously presented, manufactured having 800 μm pores and cultured in both OM and GM. In order to attribute osteoinductive tendencies to our scaffolds, osteoblastogenesis of the BMSCs has to occur in the absence of osteogenic factors. This means that the BMSCs on the scaffolds cultured in GM would have to differentiate towards osteoblasts.

Adhesion of cells in GM culturing conditions was thoroughly investigated as described in (section 3.4), with promising results presented in section 4.2. We have previously described the scaffold roughness as being in the range of 60 μm (section 4.1), which according to the previously mentioned literature is beyond the suitable range to induce differentiation of BMSCs into osteoblasts. However, comparing the size of the BMSCs (30 μm , Ge et al. (2014)) to the large surface morphology, we find that the cells are only half the size of the reported scaffold roughness. The SEM images from Figure 4.1 show large, rounded surface cues formed by the partial melting of powder grains during the EBM process. If we regard these formations as macro roughness, we see that the micro roughness on the surface of the adhered powder grains actually is in the range of a few microns (Figure 4.2). Micro roughness on the powder grains themselves might provide an influence on the osteoblastogenesis. If the surface roughness of the powder particles is in the osteoinductive range of 1 μm as presented by Faia-Torres et al. (2014, 2015) and Kolind et al. (2014), it might be favourable for the differentiation of the BMSCs. On a side note, one might argue that partially adhered particles on the surfaces poses a risk with regards to particle detachment. If metal particles were to detach from an implant inside the body, inflammation and immune reactions could be onset. It is therefore important to ensure that the partially adhered particles having weak connections are removed. Especially when AM is applied in the manufacturing of implants. This is however beyond the scope of our investigation.

When the cell activity is investigated (section 4.3) the BMSCs cultured in GM show a reduced activity when compared to the cells cultured in OM (Figure 4.8). This lower activity expression seems to take place until day 5 when it finally increases. By day 9 the activity has almost reached the level of the cells cultured in OM. As previously mentioned, an increase in activity may be due to the onset of differentiation.

Given the increased proliferation expected in GM, however, a larger quantity of BMSCs should be present after 9 d. If the cells had differentiated to the same extent as the OM cultured cells, we would expect a higher signal. This leads us to think that the cells cultured in GM may have started differentiation, but not to the same extent as the cells cultured in OM. This indication is further supported by the results of the ALP staining presented in section 4.4: Expression of ALP is found in GM cultured BMSCs suggesting the, at least imminent, onset of cell differentiation. A weaker signal compared to cells cultured in OM however, supports the assumption that a lower BMSC percentage is differentiating in GM. As previously presented, Faia-Torres et al. (2015) obtained similar results for their scaffolds having roughness gradients. The cultured cells that were in the 1 μm range showed an upregulation of ALP already at day 4.

The previously discussed results from the PCR analysis showed a slight upregulation of RUNX2

late in the culturing of the 3D scaffold in GM (between day 14 and day 21). The late expression of RUNX2 was, as previously mentioned, also reported by Sollazzo et al. (2011). The increased RUNX2 expression for the 3D scaffold cultured in GM is indicative of osteoinductive properties. These indications are further supported by the upregulation of Osteocalcin expressed by GM cultured cells.

Results from the ARS presented in section 4.6 provides some intriguing insight: The cells cultured in OM seem to have a morphology spanning the pores of the scaffolds (Figure 4.15). The presence of calcium found on these cells is a strong indication of osteoblastogenesis. In contrast, the morphology of cells cultured in GM does not appear to be extensively spanning the pores. The cells seem to be found primarily on the scaffold surfaces inside the pores. However, calcium deposition is also found in these scaffolds which suggests that also these cells have differentiated.

Calcium was found on the bottom of the OM cultured well, which implies that the activity signal measured during the alamarBlue® assays also originated from the cells adhered to the well and not only from the scaffold. This may have contributed to an over estimation of the cell activity. The increased ARS signal expressed by the scaffold cultured in OM may also be attributed to insufficient wash cycles: After destaining, the scaffolds were stored some days in PBS. When re-examined, the PBS solution containing the OM cultured scaffold expressed a red colour, suggesting that trapped stain may still have been residing inside the scaffold. This indicates that trapped stain may also have leaked into the solution during destaining, thus increasing absorbance of the tested solution. Similar outflow of trapped stain was not found for neither the GM cultured scaffold nor the control scaffold.

Meanwhile, no mineralisation was found on the bottom of the GM cultured well. If in fact the activity increase during the alamarBlue® assays is due to an onset of differentiation, the measured activity increase in the GM cultured cells seems to be originating to a large extent from the cells adhered to the porous scaffold.

The signal quantification performed after destaining, presented in the bar diagram in Figure 4.15, shows much lower mineralisation values for the scaffold cultured in GM. This result is strengthening the theory that more cells are on the verge of undergoing osteoblastogenesis.

To summarise the results, some trends are found pointing towards a possible porosity effect on the differentiation of BMSCs. However, the generally reduced signal expression over multiple tests, compared both to the cells cultured in OM and the 2D controls in the PCR, is suggesting that the scaffolds are not expressing strong osteoinducing tendencies.

The hypothesis that Ti-6Al-4V porous scaffolds are osteoconductive and -inductive has been discussed. Conclusive evidence was however not found, especially concerning the osteoinductive properties. The inductive factors of surface roughness and porosity, as well as the interplay of these properties remains to be discovered.

5.3 Challenges

Thus far, we have discussed the main points of interest of this thesis regarding the osteoinductive and osteoconductive properties of porous scaffolds.

Now the focus will be directed at describing and discussing the faced challenges during this work. Some of the main choices done will be and evaluated and possible solutions presented. This

will hopefully give some advise to future researchers.

5.3.1 Geometrical considerations

The scaffolds manufactured used in this study were designed using a simple cubic, fully rounded structure of equidimensional 800 μm struts and pores. This ensured both a uniform porosity distribution and a simpler manufacturing. By tilting the structure 35°, as described in section 4.1, the scaffolds lent themselves to be easily characterised in the confocal microscope. Another positive, although unexpected outcome of this inclination, was that the BMSCs were able to easily adhere to multiple strut layers. If the struts had been directly covering each other on the vertical plane, the static culturing conditions would have proven an obstacle for the cell adhesion on internal geometries.

5.3.2 Large porosity dimensions

The chosen lattices were dimensionally on the upper side of the scale compared to the ones found in e.g. Heintz et al. (2008a,b); Li et al. (2016) and Cheng et al. (2014). There are several reasons for this choice:

Firstly, Grunsven (2014) found that the minimal strut sizes achievable by EBM were in the range of 550 μm (although later optimisation achieved even smaller sizes). As reported in Table 3.1, the set 200 μm hatch would at best generate struts of $>200 \mu\text{m}$. Not accounting for the inherent partially melted particles covering every surface. The same investigator also reported difficulties in the removal of unmelted powder for pores smaller than 700 μm . Pores of 500 μm would only be cleaned to a depth of 1 mm.

Secondly, the adhered cells were to be characterised at a depth of more than 2 mm. A lens with a long focal length and lower magnification had to be used. In order to obtain the best images by allowing more light to penetrate the scaffold, large enough pores were needed.

Finally, due to the inherent static culture conditions, the vascularisation of the scaffolds could have become an issue. The flow of media through the scaffolds was limited to the few times the medium got changed, in addition to possible vascular permeability provided by temperature gradients. It was imperative to secure that new medium reached all cells at a steady pace. Larger pores help in this respect.

5.3.3 Consistency of seeding

The seeding of the cells proved to be a source of uncertainty. Even with pores of 800 μm , the suspension tended to form droplets covering the top surface of the scaffolds, instead of populating the interconnected porosity. This was probably due to the viscosity of the cell suspension combined with the poor capillary permeability of the scaffold material. Grunsven (2014) used a similar seeding technique in his work, although in his case, the scaffolds were able to keep the cell suspension inside the pores simply by capillary attraction.

Our study attempts a remedy by immersing the scaffolds in medium prior to seeding of BMSCs. With the permeability increased, however, the capillary forces were not able to keep the suspension

inside the scaffold. The entire well was filled with medium at each seeding, which meant that not all seeded BMSCs would adhere to the scaffolds.

A control experiment that may prove useful for future studies is to assess the *seeding efficacy*, as reported by Kasten et al. (2003). By transferring seeded scaffolds to new wells after a short incubation of e.g. 24 h (instead of 3 days as described in subsection 3.3.1), the seeding efficacy can be determined by trypsinating and counting the remaining cells in the well. Subtracting this number from the known seeding number would provide insight in how many cells adheres to the 3D scaffolds. This would enable a better understanding of the results and provide the opportunity to scale i.e. the activity graph resulting from alamarBlue® against an estimated cell concentration in the start of the experiment.

5.3.4 Computer capacity and scaffold design

When designing a component in a CAD software, the model size increases with the amount of faces present in the model. For the design of the scaffolds used in this thesis, this effect posed a challenge. Although relatively small in size, the scaffolds had a lot of distinct faces resulting from all the rounded features. Being especially true for the larger 24-well scaffolds, a lot of processor and RAM capacity was needed.

In order to handle the large CAD files, a powerful stationary computer was used. Even this computer struggled with the modelling. After some research and tips from colleagues, some *workarounds* were implemented. The computationally reduced design procedures are described in section 3.1.

By exporting the unit cell to an assembly, the computational requirements during assembly of the large structure was greatly reduced. Once re-imported as a component and cut-extruded, the final model was easier to handle.

Residing in the previous computational argument, challenges related to the FEA of the scaffolds was also found. The 96-well scaffold model was used to perform a FEA compression simulation as described in section 3.1. The 24-well scaffold model file resulted very complex to mesh properly. By using a selection of modifications and symmetry considerations the meshing of the large scaffold could however have been simplified. Although considering that both the 96-well scaffold and the 24-well scaffold are composed by the same unit cell, it was decided to directly mesh the smaller 96-well scaffold model.

5.3.5 Reliability of compression results

During the physical compression tests, the scaffolds needed to be surface finished in order to remove the inherent surface roughness. The micro-scale protrusions would otherwise easily deform prior to the main scaffold structure. The smaller 96-well scaffolds proved difficult to abrasively finish to close tolerances and flatness. Simultaneously, the larger amount of lattice cells present in the larger 24-well scaffold are beneficial to obtain reliable average stiffness values. The 24-well scaffolds were therefore selected for physical compression testing.

As shown in Figure 4.4, the boundary conditions set during the compression ended the test when ~ 3 kN was reached. The Young's modulus was not yet stabilised at this point, which meant

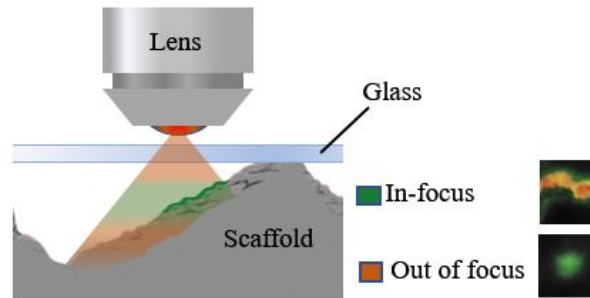


Figure 5.1: In-focus range during microscopy

During microscopy characterisation, the DOF will be a limitation when having large surface variations. The green range represents the in-focus range (DOF) of a given lens. The objects residing in this range (green band) will appear detailed, while the ones residing outside this range (orange), will not appear as clear. When adjusting the focus, the central part of the images is often used as reference.

only an approximate value was obtained. This value is much smaller than the one predicted by the simulation (7.9 GPa). To solve this issue it was postulated that, although having been abrasively finished, only a fraction of the scaffold was actually in contact with the compression crossheads. When finding an area reduction factor by image analysis (Figure 4.5), the stiffness was adjusted to 12.9 GPa, a value closer to the predicted stiffness of 16.5 GPa. This is nonetheless an imprecise result, as the image analysis may be regarded as an *ad hoc* method.

Figure 4.1 provides another interesting clue as to why the stiffness was reduced: The thickness of the struts is not constant, as thinner sections, cracks and defects are present. Protrusions such as partially melted particles do not participate in the stiffness of the scaffold, while cracks can greatly reduce the strength of the struts. Combined, the effects may severely reduce the stiffness of the scaffold.

The purpose of conducting the compression tests was to show that the manufactured scaffolds were in the stiffness range of bone (0.02 – 30 GPa). Although the methods used to obtain the compression stiffness results can be subjected to further scrutiny, the stiffness values are undoubtedly in the prescribed range.

5.3.6 Microscopy challenges

As mentioned in section 4.4 and section 4.2, the large geometric variance in our scaffolds is a challenge. For microscopes having the possibility to perform z-stacks of a predefined depth range, in-focus images can be taken of a deep section of the scaffold. The only drawback is a time consuming imaging. While for microscopes not capable to perform such stacks, the image quality will suffer. As described by Figure 5.1, only a section of the entire surface will be in-focus in each image, often referred to as the depth-of-field (DOF). When performing z-stacks the focus is shifted between each capture thus expanding the DOF (green range). When we imaged the ALP staining, it was not possible to perform a stacking of the images. Hence, only the central part of each image appear in-focus.

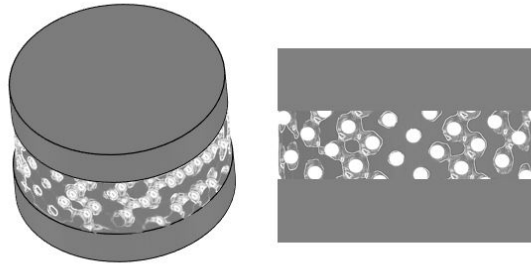


Figure 5.2: Proposed compression test scaffolds

By manufacturing compression test scaffolds having stiff, massive sections in contact with the testing apparatus (top and bottom) the stiffness characteristics may be investigated properly.

5.4 Future work

To sum up, there are four main topics the author retains as most interesting for future studies:

Firstly, it would be beneficial to manufacture own compression scaffolds having massive plates at either end of the scaffold as depicted in Figure 5.2, it will be possible to assess with greater precision the scaffold stiffness.

Secondly, the *in vitro* culturing of scaffolds in dynamic conditions, i.e. with the use of a bioreactor, would generate results more similar to in-body conditions. As 3D scaffolds have faces oriented in every direction, dynamic conditions in the medium would possibly enable BMSCs to adhere to every side of the scaffolds. In our study they only adhered to the up-facing surfaces.

Thirdly, special attention to the stiffness and also topological optimisation is an important topic for future studies. Developing an algorithm able to predict the cell's *in vivo* responses in lattices of different geometry and size, would be an important tool to be used in the design of the next generation of implants. Especially if integrated with topological optimisation.

Finally, a surface roughness study would enable the cross application of known cell influencing roughness factors together with the porosity effects. Results would potentially be highly osteoinductive implants designed to minimise stress shielding. In connection to this study, it would be interesting to find ways to manufacture AM powders having $1\ \mu\text{m}$ surface roughness. As this roughness values already has proven to induce osteoblastogenesis, powder having this surface roughness would potentially enable manufacturers to draw strength from the inherent skin formation of the PBF AM processes, and utilise it as a tool for obtaining better osteoinduction capabilities in implants.

Conclusions

In this Master's Thesis I have investigated the osteoconductive and osteoinductive potential of additive manufactured porous Ti-6Al-4v structures. This was done in three main steps: First, a broad literature study was conducted aimed at introducing important concepts from both the mechanical and the biomedical fields that would prove influential to the conducted experimental work.

Then, a porous scaffold geometry was designed in relation to the findings previously discovered by other researchers. These scaffolds had pores of 800 μm and were further developed to enable the easy characterisation during the planned experiments.

After being manufactured, the scaffolds were seeded with BMSCs and cultured with and without the addition of osteogenic factors. A variety of assays and experiments were conducted to assess both their osteoconductivity and osteoinductivity: The adhesion of BMSCs was characterised by confocal microscopy, which showed increasing cell adhesion over time and a cell morphology covering the struts of the porous structures. The BMSC activity measured over 9 days culture, showed a steady activity increase for cells cultured in both mediums. ALP expression was characterised after 10 days culture, showing higher ALP expression in cells cultured in osteoinductive medium. Gene expression as monitored using real-time PCR over the course of 21 days of culture, resulted inconclusive. However, BMSCs cultured in GM expressed a slight increase of RUNX2 and Osteocalcin during this period possibly suggesting an onset of differentiation. Lastly, mineralisation was found in scaffolds cultured in both mediums indicating that the BMSCs had differentiated and started the deposition of osteoid.

The sum of the results suggest that porous EBM Ti-6Al-4V structures seem to be osteoconductive. The same scaffolds also show a limited capability to induce the differentiation of the BMSCs when cultured without osteogenic factors in medium.

A large knowledge base already exist concerning the impact of surface roughness on the induction of osteoblastogenesis. Future work in this field should focus on applying this knowledge in the 3D domain, by exploring the interplay of surface roughness and porosity. Perhaps also researching ways to directly manufacture porous structures by EBM having ideal surface roughness characteristics. This research may pave the way towards highly bioactive implant design having tailored material and osteogenic properties for prolonging implant lifetime and shortening patient recovery phases.

Bibliography

- Abagnale, G., Steger, M., Nguyen, V. H., Hersch, N., Sechi, A., Joussen, S., Denecke, B., Merkel, R., Hoffmann, B., Dreser, A., Schnakenberg, U., Gillner, A., and Wagner, W. (2015). Surface topography enhances differentiation of mesenchymal stem cells towards osteogenic and adipogenic lineages. *Biomaterials*, 61:316–326.
- Albrektsson, T., Brnemark, P.-I., Hansson, H.-A., and Lindström, J. (1981). Osseointegrated titanium implants: Requirements for ensuring a long-lasting, direct bone-to-implant anchorage in man. *Acta Orthopaedica Scandinavica*, 52(2):155–170.
- Albrektsson, T. and Johansson, C. (2001). Osteoinduction, osteoconduction and osseointegration. *European Spine Journal*, 10(2):S96–S101.
- Bayliss, L., Mahoney, D. J., and Monk, P. (2012). Normal bone physiology, remodelling and its hormonal regulation. *Surgery (Oxford)*, 30(2):47 – 53. Orthopaedics I: General Principles.
- Bruderer, M., Richards, R. G., Alini, M., and Stoddart, M. J. (2014). Role and regulation of runx2 in osteogenesis. *Eur Cell Mater*, 28:269–86.
- Bugbee, W. D., Culpepper, W. J., Engh, C. A., and Engh, C. A. (1997). Long-term clinical consequences of stress-shielding after total hip arthroplasty without cement*. *JBJS*, 79(7):1007–12.
- Chan, C.-W., Carson, L., Smith, G. C., Morelli, A., and Lee, S. (2017). Enhancing the antibacterial performance of orthopaedic implant materials by fibre laser surface engineering. *Applied Surface Science*, 404:67–81.
- Cheng, A., Humayun, A., Cohen, D. J., Boyan, B. D., and Schwartz, Z. (2014). Additively manufactured 3d porous ti-6al-4v constructs mimic trabecular bone structure and regulate osteoblast proliferation, differentiation and local factor production in a porosity and surface roughness dependent manner. *Biofabrication*, 6(4):045007–045007.
- Chiu, L.-H., Lai, W.-F. T., Chang, S.-F., Wong, C.-C., Fan, C.-Y., Fang, C.-L., and Tsai, Y.-H. (2014). The effect of type ii collagen on msc osteogenic differentiation and bone defect repair. *Biomaterials*, 35(9):2680–2691.

-
- Dalby, M. J., Gadegaard, N., and Oreffo, R. O. C. (2014). Harnessing nanotopography and integrin-matrix interactions to influence stem cell fate. *Nat Mater*, 13(6):558–569.
- de Formanoir, C., Michotte, S., Rigo, O., Germain, L., and Godet, S. (2016). Electron beam melted ti6al4v: Microstructure, texture and mechanical behavior of the as-built and heat-treated material. *Materials Science and Engineering: A*, 652:105 – 119.
- Dominici, M., Le Blanc, K., Mueller, I., Slaper-Cortenbach, I., Marini, F. C., Krause, D. S., Deans, R. J., Keating, A., Prockop, D. J., and Horwitz, E. M. (2006). Minimal criteria for defining multipotent mesenchymal stromal cells. the international society for cellular therapy position statement. *Cytotherapy*, 8(4):315–317.
- Ek, R. K., Rnnar, L.-E., Bckstm, M., and Carlsson, P. (2016). The effect of ebm process parameters upon surface roughness. *Rapid Prototyping Journal*, 22(3):495–503.
- Faia-Torres, A. B., Charnley, M., Goren, T., Guimond-Lischer, S., Rottmar, M., Maniura-Weber, K., Spencer, N. D., Reis, R. L., Textor, M., and Neves, N. M. (2015). Osteogenic differentiation of human mesenchymal stem cells in the absence of osteogenic supplements: A surface-roughness gradient study. *Acta Biomaterialia*, 28:64–75.
- Faia-Torres, A. B., Guimond-Lischer, S., Rottmar, M., Charnley, M., Goren, T., Maniura-Weber, K., Spencer, N. D., Reis, R. L., Textor, M., and Neves, N. M. (2014). Differential regulation of osteogenic differentiation of stem cells on surface roughness gradients. *Biomaterials*, 35(33):9023–9032.
- FDA, U. (2016). Cfr - code of federal regulations title 21–food and drugs, chapter i–food and drug administration, department of health and human services, subchapter h–medical devices, part 888 - orthopedic devices. 21(14.05.2017).
- Fiedler, J., zdemir, B., Bartholom, J., Plettl, A., Brenner, R. E., and Ziemann, P. (2013). The effect of substrate surface nanotopography on the behavior of multipotent mesenchymal stromal cells and osteoblasts. *Biomaterials*, 34(35):8851–8859.
- Frost, H. M. (2004). A 2003 update of bone physiology and wolff’s law for clinicians. *The Angle Orthodontist*, 74(1):3–15. PMID: 15038485.
- Gattazzo, F., Urciuolo, A., and Bonaldo, P. (2014). Extracellular matrix: A dynamic microenvironment for stem cell niche(). *Biochimica et Biophysica Acta*, 1840(8):2506–2519.
- Ge, J., Guo, L., Wang, S., Zhang, Y., Cai, T., Zhao, R. C. H., and Wu, Y. (2014). The size of mesenchymal stem cells is a significant cause of vascular obstructions and stroke. *Stem Cell Reviews and Reports*, 10(2):295–303.
- Geiger, B., Spatz, J. P., and Bershadsky, A. D. (2009). Environmental sensing through focal adhesions. *Nat Rev Mol Cell Biol*, 10(1):21–33.
- Gibson, I., Rosen, D. W., and Stucker, B. (2010). *Design for Additive Manufacturing*, pages 299–332. Springer US, Boston, MA.

-
- Grunsven, W. v. (2014). *Porous metal implants for enhanced bone ingrowth and stability*. PhD thesis, The University Of Sheffield.
- Gusarov, A., Yadroitsev, I., Bertrand, P., and Smurov, I. (2007). Heat transfer modelling and stability analysis of selective laser melting. *Applied Surface Science*, 254(4):975 – 979. Laser synthesis and processing of advanced materialsE-MRS-P Symposium.
- Heinl, P., Krner, C., and Singer, R. F. (2008a). Selective electron beam melting of cellular titanium: Mechanical properties. *Advanced Engineering Materials*, 10(9):882–888.
- Heinl, P., Miller, L., Krner, C., Singer, R. F., and Miller, F. A. (2008b). Cellular ti6al4v structures with interconnected macro porosity for bone implants fabricated by selective electron beam melting. *Acta Biomaterialia*, 4(5):1536–1544.
- Herzog, D., Seyda, V., Wycisk, E., and Emmelmann, C. (2016). Additive manufacturing of metals. *Acta Materialia*, 117:371 – 392.
- Horwitz, E. M., Le Blanc, K., Dominici, M., Mueller, I., Slaper-Cortenbach, I., Marini, F. C., Deans, R. J., Krause, D. S., and Keating, A. (2005). Clarification of the nomenclature for msc: The international society for cellular therapy position statement. *Cytotherapy*, 7(5):393–395.
- Huang, W., Yang, S., Shao, J., and Li, Y.-P. (2007). Signaling and transcriptional regulation in osteoblast commitment and differentiation. *Frontiers in bioscience : a journal and virtual library*, 12:3068–3092.
- Jonsdottir-Buch, S. M., Lieder, R., and Sigurjonsson, O. E. (2013). Platelet lysates produced from expired platelet concentrates support growth and osteogenic differentiation of mesenchymal stem cells. *PLoS One*, 8(7):e68984.
- Jonsdottir-Buch, S. M., Sigurgrimsdottir, H., Lieder, R., and Sigurjonsson, O. E. (2015). Expired and pathogen-inactivated platelet concentrates support differentiation and immunomodulation of mesenchymal stromal cells in culture. *Cell Transplant*, 24(8):1545–54.
- Kamalia, N., McCulloch, C. A., Tenenbaum, H. C., and Limeback, H. (1992). Direct flow cytometric quantification of alkaline phosphatase activity in rat bone marrow stromal cells. *Journal of Histochemistry & Cytochemistry*, 40(7):1059–1065. PMID: 1376742.
- Karageorgiou, V. and Kaplan, D. (2005). Porosity of 3d biomaterial scaffolds and osteogenesis. *Biomaterials*, 26(27):5474 – 5491.
- Kasten, P., Luginbhl, R., van Griensven, M., Barkhausen, T., Krettek, C., Bohner, M., and Bosch, U. (2003). Comparison of human bone marrow stromal cells seeded on calcium-deficient hydroxyapatite, -tricalcium phosphate and demineralized bone matrix. *Biomaterials*, 24(15):2593 – 2603.

-
- Kolind, K., Kraft, D., Bggild, T., Duch, M., Lovmand, J., Pedersen, F. S., Bindslev, D. A., Bnger, C. E., Foss, M., and Besenbacher, F. (2014). Control of proliferation and osteogenic differentiation of human dental-pulp-derived stem cells by distinct surface structures. *Acta Biomaterialia*, 10(2):641–650.
- Kruth, J. P., Levy, G., Klocke, F., and Childs, T. H. C. (2007). Consolidation phenomena in laser and powder-bed based layered manufacturing. *CIRP Annals - Manufacturing Technology*, 56(2):730–759.
- Lee, K. and Goodman, S. B. (2008). Current state and future of joint replacements in the hip and knee. *Expert Review of Medical Devices*, 5(3):383–393. PMID: 18452388.
- Levy, G. N., Schindel, R., and Kruth, J. (2003). Rapid manufacturing and rapid tooling with layer manufacturing (lm) technologies, state of the art and future perspectives. *CIRP Annals - Manufacturing Technology*, 52(2):589 – 609.
- Lewallen, E. A., Riester, S. M., Bonin, C. A., Kremers, H. M., Dudakovic, A., Kakar, S., Cohen, R. C., Westendorf, J. J., Lewallen, D. G., and van Wijnen, A. J. (2015). Biological strategies for improved osseointegration and osteoinduction of porous metal orthopedic implants. *Tissue Engineering. Part B, Reviews*, 21(2):218–230.
- Li, G., Wang, L., Pan, W., Yang, F., Jiang, W., Wu, X., Kong, X., Dai, K., and Hao, Y. (2016). In vitro and in vivo study of additive manufactured porous ti6al4v scaffolds for repairing bone defects. *Scientific Reports*, 6:34072.
- Li, R., Liu, J., Shi, Y., Wang, L., and Jiang, W. (2012). Balling behavior of stainless steel and nickel powder during selective laser melting process. *The International Journal of Advanced Manufacturing Technology*, 59(9):1025–1035.
- Little, N., Rogers, B., and Flannery, M. (2011). Bone formation, remodelling and healing. *Surgery (Oxford)*, 29(4):141 – 145. Orthopaedics V: Paediatrics.
- Liu, C., Lin, G., Yang, D., and Qi, M. (2006). In vitro corrosion behavior of multilayered ti/tin coating on biomedical aisi 316l stainless steel. *Surface and Coatings Technology*, 200(1213):4011–4016.
- Liu, X., Chu, P. K., and Ding, C. (2004). Surface modification of titanium, titanium alloys, and related materials for biomedical applications. *Materials Science and Engineering: R: Reports*, 47(34):49–121.
- Lock, J. G., Wehrle-Haller, B., and Strmblad, S. (2008). Cellmatrix adhesion complexes: Master control machinery of cell migration. *Seminars in Cancer Biology*, 18(1):65–76.
- Martin, T. J., Ng, K. W., and Nicholson, G. C. (1988). 1 cell biology of bone. *Baillire's Clinical Endocrinology and Metabolism*, 2(1):1 – 29.

-
- Martin, T. J., Ng, K. W., and Sims, N. A. (2013). Chapter 2 - basic principles of bone cell biology. In Karsenty, G., editor, *Translational Endocrinology of Bone*, pages 5 – 26. Academic Press, San Diego.
- Metavarayuth, K., Sitasuwan, P., Zhao, X., Lin, Y., and Wang, Q. (2016). Influence of surface topographical cues on the differentiation of mesenchymal stem cells in vitro. *ACS Biomaterials Science and Engineering*, 2(2):142–151.
- Mikulewicz, M. and Chojnacka, K. (2011). Cytocompatibility of medical biomaterials containing nickel by osteoblasts: a systematic literature review. *Biological Trace Element Research*, 142(3):865–889.
- Murr, L., Esquivel, E., Quinones, S., Gaytan, S., Lopez, M., Martinez, E., Medina, F., Hernandez, D., Martinez, E., Martinez, J., Stafford, S., Brown, D., Hoppe, T., Meyers, W., Lindhe, U., and Wicker, R. (2009). Microstructures and mechanical properties of electron beam-rapid manufactured ti6al4v biomedical prototypes compared to wrought ti6al4v. *Materials Characterization*, 60(2):96 – 105.
- Murr, L. E. (2016). Frontiers of 3d printing/additive manufacturing: from human organs to aircraft fabrication. *Journal of Materials Science & Technology*, 32(10):987 – 995.
- Murr, L. E., Gaytan, S. M., Ramirez, D. A., Martinez, E., Hernandez, J., Amato, K. N., Shindo, P. W., Medina, F. R., and Wicker, R. B. (2012a). Metal fabrication by additive manufacturing using laser and electron beam melting technologies. *Journal of Materials Science & Technology*, 28(1):1 – 14.
- Murr, L. E., Martinez, E., Amato, K. N., Gaytan, S. M., Hernandez, J., Ramirez, D. A., Shindo, P. W., Medina, F., and Wicker, R. B. (2012b). Fabrication of metal and alloy components by additive manufacturing: Examples of 3d materials science. *Journal of Materials Research and Technology*, 1(1):42 – 54.
- Naddeo, P., Laino, L., Noce, M. L., Piattelli, A., Rosa, A. D., Iezzi, G., Laino, G., Paino, F., Papaccio, G., and Tirino, V. (2015). Surface biocompatibility of differently textured titanium implants with mesenchymal stem cells. *Dental Materials*, 31(3):235 – 243.
- Nakashima, K., Zhou, X., Kunkel, G., Zhang, Z., Deng, J. M., Behringer, R. R., and de Crombrughe, B. (2002). The novel zinc finger-containing transcription factor osterix is required for osteoblast differentiation and bone formation. *Cell*, 108(1):17–29.
- Ninomi, M. (2008). Mechanical biocompatibilities of titanium alloys for biomedical applications. *Journal of the Mechanical Behavior of Biomedical Materials*, 1(1):30–42.
- NJR, T. N. E. B. (2016). 13th annual report, national joint registry for england, wales, northern ireland and the isle of man. *National Joint Registry*.
- Nouri, A. and Wen, C. (2015). *1 - Introduction to surface coating and modification for metallic biomaterials*, pages 3–60. Woodhead Publishing.
-

-
- Okshevsky, M., Regina, V. R., and Meyer, R. L. (2015). Extracellular dna as a target for biofilm control. *Current Opinion in Biotechnology*, 33:73–80.
- Oshida, Y. (2013). 7 - *Implant-Related Biological Reactions*, pages 169–223. Elsevier, Oxford.
- Parthasarathy, J., Starly, B., Raman, S., and Christensen, A. (2010). Mechanical evaluation of porous titanium (ti6al4v) structures with electron beam melting (ebm). *Journal of the Mechanical Behavior of Biomedical Materials*, 3(3):249–259.
- Pawley, J. B. (2006). Handbook of biological confocal microscopy.
- Prins, H.-J., Rozemuller, H., Vonk-Griffioen, S., Verweij, V. G., Dhert, W. J., Slaper-Cortenbach, I. C., and Martens, A. C. (2009). Bone-forming capacity of mesenchymal stromal cells when cultured in the presence of human platelet lysate as substitute for fetal bovine serum. *Tissue Engineering Part A*, 15(12):3741–3751.
- Prez-Campo, F. M., Santurtn, A., Garca-Ibarbia, C., Pascual, M. A., Valero, C., Garcs, C., Saudo, C., Zarrabeitia, M. T., and Riancho, J. A. (2016). Osterix and runx2 are transcriptional regulators of sclerostin in human bone. *Calcified Tissue International*, 99(3):302–309.
- Rampersad, S. N. (2012). Multiple applications of alamar blue as an indicator of metabolic function and cellular health in cell viability bioassays. *Sensors*, 12(9):12347–12360.
- Raphel, J., Holodniy, M., Goodman, S. B., and Heilshorn, S. C. (2016). Multifunctional coatings to simultaneously promote osseointegration and prevent infection of orthopaedic implants. *Biomaterials*, 84:301–314.
- Rho, J. Y., Ashman, R. B., and Turner, C. H. (1993). Young's modulus of trabecular and cortical bone material: Ultrasonic and microtensile measurements. *Journal of Biomechanics*, 26(2):111–119.
- Rombouts, M., Kruth, J., Froyen, L., and Mercelis, P. (2006). Fundamentals of selective laser melting of alloyed steel powders. *CIRP Annals - Manufacturing Technology*, 55(1):187 – 192.
- Schlie-Wolter, S., Ngezahayo, A., and Chichkov, B. N. (2013). The selective role of ecm components on cell adhesion, morphology, proliferation and communication in vitro. *Experimental Cell Research*, 319(10):1553–1561.
- Semwogerere, D. (2005). Confocal microscopy. *Encyclopedia of Biomaterials and Biochemical Engineering*.
- Shiomi, M., Osakada, K., Nakamura, K., Yamashita, T., and Abe, F. (2004). Residual stress within metallic model made by selective laser melting process. *CIRP Annals - Manufacturing Technology*, 53(1):195 – 198.
- Shunmugavel, M., Polishetty, A., and Littlefair, G. (2015). Microstructure and mechanical properties of wrought and additive manufactured ti-6al-4v cylindrical bars. *Procedia Technology*, 20:231–236.

-
- Sidambe, A. (2014). Biocompatibility of advanced manufactured titanium implants a review. *Materials*, 7(12):8168.
- Singh, S. K., Mohammed, M. T., Khan, Z. A., and Siddiquee, A. N. (2014). 3rd international conference on materials processing and characterisation (icmpc 2014) surface modifications of titanium materials for developing corrosion behavior in human body environment: A review. *Procedia Materials Science*, 6:1610–1618.
- Slotwinski, J. A., Garboczi, E. J., Stutzman, P. E., Ferraris, C. F., Watson, S. S., and Peltz, M. A. (2014). Characterization of metal powders used for additive manufacturing. *Journal of Research of the National Institute of Standards and Technology*, 119:460–493.
- Sollazzo, V., Palmieri, A., Girardi, A., Farinella, F., and Carinci, F. (2011). Trabecular titanium induces osteoblastic bone marrow stem cells differentiation. *Journal of Biotechnology & Biomaterials*, 2011.
- Strano, G., Hao, L., Everson, R. M., and Evans, K. E. (2013). Surface roughness analysis, modelling and prediction in selective laser melting. *Journal of Materials Processing Technology*, 213(4):589 – 597.
- Sun, L., Danoux, C. B., Wang, Q., Pereira, D., Barata, D., Zhang, J., LaPointe, V., Truckenmiller, R., Bao, C., Xu, X., and Habibovic, P. (2016a). Independent effects of the chemical and microstructural surface properties of polymer/ceramic composites on proliferation and osteogenic differentiation of human mscs. *Acta Biomaterialia*.
- Sun, Z., Tan, X., Tor, S. B., and Yeong, W. Y. (2016b). Selective laser melting of stainless steel 316L with low porosity and high build rates. *Materials & Design*, 104:197–204.
- Tellis, B. C., Szivek, J. A., Bliss, C. L., Margolis, D. S., Vaidyanathan, R. K., and Calvert, P. (2008). Trabecular scaffolds created using micro ct guided fused deposition modeling. *Materials Science and Engineering: C*, 28(1):171–178.
- Toh, W. Q., Wang, P., Tan, X., Nai, M. L. S., Liu, E., and Tor, S. B. (2016). Microstructure and wear properties of electron beam melted ti-6al-4v parts: A comparison study against as-cast form. *Metals*, 6(11):284.
- Tran, P., Ngo, T. D., Ghazlan, A., and Hui, D. (2017). Bimaterial 3d printing and numerical analysis of bio-inspired composite structures under in-plane and transverse loadings. *Composites Part B: Engineering*, 108:210 – 223.
- Trešše, R. and Miheli, A. (2012). *Joint Replacement: Historical Overview*, pages 7–11. Springer London, London.
- Tsuji, K., Steindler, K. A., and Harrison, S. J. (1980). Limulus amoebocyte lysate assay for detection and quantitation of endotoxin in a small-volume parenteral product. *APPLIED AND ENVIRONMENTAL MICROBIOLOGY*, 40(3):533–538.
-

-
- van Eck, C. F., Chen, A. F., Klatt, B. A., D'Antonio, J., and Fu, F. (2009). The classification of implants: Class i, ii, iii. *Journal of Long-Term Effects of Medical Implants*, 19(3):185–193.
- Wahl, L., Maas, S., Waldmann, D., Zrbes, A., and Frres, P. (2012). Shear stresses in honeycomb sandwich plates: Analytical solution, finite element method and experimental verification. *Journal of Sandwich Structures & Materials*, 14(4):449–468.
- Wang, X., Xu, S., Zhou, S., Xu, W., Leary, M., Choong, P., Qian, M., Brandt, M., and Xie, Y. M. (2016a). Topological design and additive manufacturing of porous metals for bone scaffolds and orthopaedic implants: A review. *Biomaterials*, 83:127 – 141.
- Wang, X., Xu, S., Zhou, S., Xu, W., Leary, M., Choong, P., Qian, M., Brandt, M., and Xie, Y. M. (2016b). Topological design and additive manufacturing of porous metals for bone scaffolds and orthopaedic implants: A review. *Biomaterials*, 83:127–141.
- Williams SN, Wolford ML, B. A. (2015). Hospitalization for total knee replacement among inpatients aged 45 and over: United states, 20002010. *NCHS Data Brief, U.S. DEPARTMENT OF HEALTH & HUMAN SERVICES*, (210).
- Wozniak, M. A., Modzelewska, K., Kwong, L., and Keely, P. J. (2004). Focal adhesion regulation of cell behavior. *Biochimica et Biophysica Acta (BBA) - Molecular Cell Research*, 1692(23):103–119.
- Yan, C., Hao, L., Hussein, A., and Raymont, D. (2012). Evaluations of cellular lattice structures manufactured using selective laser melting. *International Journal of Machine Tools and Manufacture*, 62:32–38.

Appendix A - Articles

.1 Scandinavian society for biomaterials- (SCSB-) abstract submission

Biocompatibility and mesenchymal stem cells adhesion on additively manufactured and magnetically assisted finished 316L stainless steel

T. Jøraholmen, M. Westrin and O. Fergani

Abstract accepted for poster-presentation and subsequently published on Cells & Materials volume no. 33, supplement 1, 2017.

Biocompatibility and mesenchymal stem cells adhesion on additively manufactured and magnetically assisted finished 316L stainless steel

T. Jøraholmen¹, M. Westrin² and O. Fergani³

¹ [NTNU](#), Faculty of Engineering Science and Technology, Dept. of Mechanical and industrial Engineering

² [NTNU](#), Faculty of Medicine, Dept. of Cancer Research and Molecular Medicine

³ [NTNU](#), Faculty of Engineering Science and Technology, Dept. of Mechanical and industrial Engineering

INTRODUCTION: Orthopaedic implant-technology nowadays, has come a long way in enhancing patient's life after surgery but there still are some issues regarding the osteointegration of implants, leading to infections and experienced pain. Additive manufacturing (AM) creates the basis for this research, being able to produce highly customizable implants. Lawrence E. Murr describes the forefront of additive manufacturing and its potential uses in orthopedy in his article from 2012 [1]. Indicating the positive factors of bone ingrowth on 3D AM scaffolds using cells of the osteoblastic lineage. To our knowledge however, there aren't any studies looking at MSC adhesion and proliferation, on AM 316L steel. This will be important to study, in order to gain insight on AM orthopaedic applications, as the first cells to be recruited at the implant site are the MSCs [2]. Hence, the scope of this research is to study AM 316L stainless steel samples, finished by magnetic assisted finishing (MAF) and look at the effects of the surface topography on the adhesion of MSCs.

METHODS: Samples are additively manufactured using M2-Concept based on powder-bed fusion technology and 316L metallic powder and subsequently surface finished using MAF. Biocompatibility of the metallic material is being assessed using enzyme-linked immunosorbent assay (ELISA) and Limulus amoebocyte lysate (LAL) assay. Mesenchymal stem cells (MSC) are then cultured on the samples for 48h, fixated and subsequently marked using Phalloidin 488 and Draq5 633. Confocal microscopy is then used to assess MSC adhesion.

RESULTS: ELISA and LAL tests both resulted clean and the first MSC adhesion test-results show good adhesion-conditions for surfaces roughness's in the low micrometre range. The control samples, which are not subject to any surface finishing, show low adhesion characteristics, thus suggesting

the beneficial impact of the MAF-finishing process on the samples.

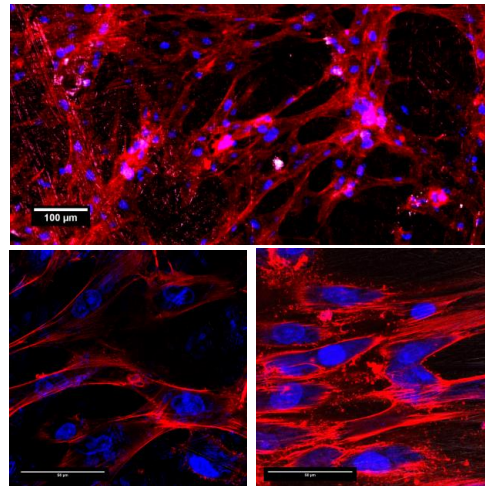


Figure 1: Top shows a 10X magnification of adhered MSC onto a sample with a surface roughness of 0.62 μ m. Bottom left and right images show a 63X magnification of two separate samples with roughness's corresponding to 0.25 μ m and 0.62 μ m respectively. Scale bars on bottom images are 50 μ m.

DISCUSSION & CONCLUSIONS: Preliminary results suggests the beneficial impact of MAF on the test-samples. The 3D-printing process does not seem to have an impact on the toxicity of the metal, as both ELISA and LAL tests resulted clean and given the cell survival during performed tests.

REFERENCES:

- Murr, L.E., et al., *Metal Fabrication by Additive Manufacturing Using Laser and Electron Beam Melting Technologies*. Journal of Materials Science & Technology, 2012. **28**(1): p. 1-14.
- Davies, J.E., *In vitro modeling of the bone/implant interface*. The Anatomical Record, 1996. **245**(2): p. 426-445.

.2 SCSB poster

Human Mesenchymal Stromal-Cells Adhesion on Additively-Manufactured
316L Stainless Steel

T. Jøraholmen, M. Westrin and O. Fergani

Poster presented by Timothy J. at the 10th annual SCSB meeting, held at Hafjell March 15 to 17, 2017.

Human Mesenchymal Stromal-Cells Adhesion on Additively-Manufactured 316L Stainless Steel

T. Jørholm¹, M. Westhrin², H. Yamaguchi³ and O. Fergani¹

¹ NTNU, Faculty of Engineering Science and Technology, Dept. of Mechanical and Industrial Engineering

² NTNU, Faculty of Medicine, Dept. of Cancer Research and Molecular Medicine

³ Department of Mechanical and Aerospace Engineering, University of Florida, Gainesville, USA

1. Introduction

Increasing world population and prolonged lifetime are two of many factors contributing to an increase in **number of total arthroplasties** being performed today[1]. Differences in **elastic moduli** and inherent **material behaviors** of current massive metallic implants lead to a number of conditions.

Additive manufacturing (AM) is the future of implant manufacturing. This process is capable of generating **complex** metallic structures having mechanical properties resembling those of bone, however some **challenges** still need solving:

- **Surface-morphology** of AM-produced parts may not be ideal. Positive effects on **bone-ingrowth** from the AM's inherent porosity, needs to be evaluated in a comprehensive study, with respect to the need for **topographically induced cell-processes** enabled by surface finishing.

2. Experimental

- AM-scaffolds in 316L stainless steel were manufactured by selective laser melting (SLM) in an M2-Concept 3D printer.
- Magneto assisted finishing was used to obtain different surface-roughness's. Surfaces were subsequently characterized using profilometry.

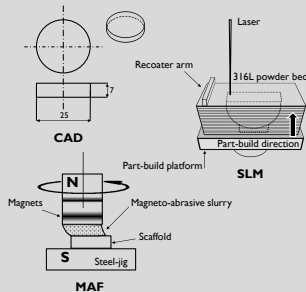


Fig. 1. Scaffold production presented in simplified steps. A CAD-file is generated of the scaffolds to be manufactured (top-left), before an SLM-printer (middle-right) is set to produce the scaffolds, before eight of the scaffolds are surface-finished using MAF (bottom-left).

- Cleanliness of the scaffold-material was evaluated by limulus amoebocyte lysate (LAL) assay.
- Bone marrow derived mesenchymal stem cells (BMSC) were seeded on scaffolds and fixated after 48h. Nuclei and cytoskeletons were stained with Draq5 633 and Phalloidin 488 respectively. Scaffolds were imaged using confocal laser scanning microscopy (LSM).

3. Results

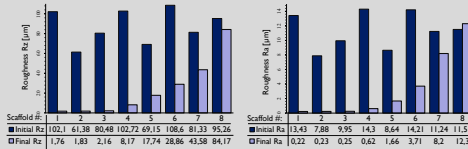


Fig. 2. Rz values (left) and Ra values (right) exhibited by the eight surface-finished samples pre- and post-MAF. Notice the gradient increase in roughness from sample 1 to 8.

3.1 Different surface topographies were obtained by MAF. Resulting Ra- and Rz-values are **increasing** **gradientally** from sub-micrometer to super-micrometer ranges. Distribution of the scaffold-roughness's are shown in Figure 2. Scaffolds 1, 2, 7 and 8 and scaffolds 3, 4, 5, and 6 are grouped in two different test rounds as duplicates.

3.2 The cleanliness of the scaffolds seem to be positively impacted by the thorough cleaning-process adopted. As the results of the LAL assay in Table 1 show, there is no endotoxins both in the 316L metal-sample and in the control-well.

Tab. 1. Endotoxin concentrations from LAL-assay given in endotoxin-units per milliliter. Both reported values are characterized as negative results.

Well contents	Endotoxin concentration
316L metal and RPMI	0.359 EU/ml
RPMI only	0.212 EU/ml

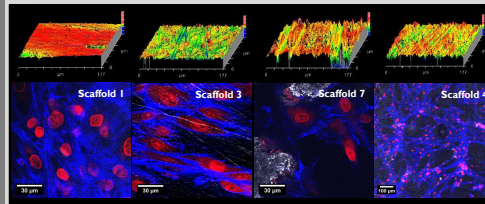


Fig. 3. Adhesion of BMSCs imaged in a Zeiss 510L META LSM. 63X Oil immersion and 10X water immersion lenses were used to characterize the scaffolds. From left to right: Scaffolds 1, 3 and 7 imaged at 63X and finally scaffold 4 imaged at 10X. All BMSCs were stained with Phalloidin 488 (blue) and Draq5 633 (red), prior to characterization.

3.3 Representative results from the adhesion tests are shown in Figure 3, the low micrometer-scale seem better suited for adhesion than the rougher scaffolds. Uniform adhesion can be observed for both scaffold 1, 3 and 4, while the BMSCs tend to adhere inside the larger topographic cues, on the rough scaffolds, as can be observed on scaffold 7. The grayscale channel, visible especially on scaffold 3 and 7, depicts the underlying metal-scaffold. Notice how the BMSCs on scaffold 3 seem to orient the cytoskeleton to underlying topographic cues. Literature reviewed on this subject seem to attribute higher cell adhesion to surface roughness's of roughly 1 µm [2]. Optimal conditions for adhesion, proliferation and differentiation needs to be evaluated further.

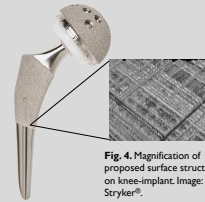


Fig. 4. Magnification of proposed surface structure on knee-implant. Image: Stryker®.

4. Research directions

- The presented results on the **MAF** performed on the scaffolds show just how versatile this surface finishing process can be. Given the potential complexity of AM-structures, there is a need to further develop MAF
- Reviewed literature studying topography induced cell fate, suggests roughness's in the micrometer scale to be better suited for **adhesion** and also to **induce osteogenic differentiation** [2]. Meanwhile, the porosity inherently present in AM 3D scaffolds is often regarded as a positive factor for achieving good bone-ingrowth conditions, hence better **osteointegration** [3]. A study focusing on the relationship between **porosity** and **surface roughness** would generate new and interesting knowledge that may be implemented in the development of future implants.
- When manufacturing implants, some surfaces with better **osteointegrative properties** are desired, while other surfaces are important to keep from facilitating the generation of bony-structures. Combining different surface-topographies will possibly enable the generation of such surfaces.

5. Summary

- MAF was used to produce different surface-roughnesses on AM-scaffolds.
- LAL assay yielded negative test result, thus inferring that the scaffold was clean.
- BMSCs were seeded on scaffolds and stained for LSM confocal investigation. Smooth surfaces seem better suited to support adhesion.

6. References

1. Lee, K. and S.B. Goodman, *Current state and future of joint replacements in the hip and knee*. Expert Review of Medical Devices, 2008. 5(3): p. 383-393.
2. Faia-Torres, A.B., et al., *Osteogenic differentiation of human mesenchymal stem cells in the absence of osteogenic supplements: A surface-roughness gradient study*. Acta Biomaterialia, 2015. 28: p. 64-75.
3. Tan, X.P., et al., *Metallic powder-bed based 3D printing of cellular scaffolds for orthopaedic implants: A state-of-the-art review on manufacturing, topological design, mechanical properties and biocompatibility*. Materials Science and Engineering, C.

7. Acknowledgements

- This study is part of an ongoing master-thesis project by the main author, at the Norwegian University for Science and Technology, 2017, Trondheim
- Portions of this study have been submitted for future presentation in article form at the 3rd CIRP Conference on BioManufacturing 2017 July 11-14, 2017, Chicago, IL, U.S.

.3 CIRP manuscript

Human Cells Growth and Adhesion on Additively-Manufactured
Medical Implants

Timothy Jøraholmen, Marita Westrin, Therese Standal, Hitomi Yamaguchi, Omar Fergani

Manuscript submitted for peer review (march 2017) for the 3rd annual conference on biomanufacturing to be held july 11 to 14, 2017.



3rd CIRP Conference on BioManufacturing

Human Cells Growth and Adhesion on Additively-Manufactured Medical Implants

Timothy Jøraholmen^a, Marita Westhrin^c, Therese Standal^c, Hitomi Yamaguchi^b, Omar Fergani^{a,*}

^aNTNU- Department of Mechanical and Industrial Engineering, Trondheim, Norway

^bDepartment of Mechanical and Aerospace Engineering, University of Florida, Gainesville, USA

^cNTNU-Department of Cancer Research and Molecular Medecine, Trondheim, Norway

* Corresponding author. Tel.: +4792032386, o.fergani@ntnu.no

Abstract

Additive manufacturing (AM) has recently been accepted for the production of various types of medical implants. However, the material structures inherent in AM-processed parts often make such parts difficult to machine. Furthermore, the surface finishing of AM-processed implants likely holds the key to further advance the state of AM-processed implants. This study uses AM-processed scaffolds with various surface morphologies obtained using magneto-abrasive-finishing (MAF) to study the effects of surface morphology on adhesion of bone marrow derived stem cells. Adhesion is the first step towards the implant-osseointegration, which is often required when using medical implants. The effects of surface morphology are detected using fluorescence microscopy.

© 2017 The Authors. Published by Elsevier B.V.

Peer-review under responsibility of the scientific committee of the 3rd CIRP Conference on BioManufacturing 2017.

Keywords: Adhesion; AM; MAF; MSC; Toxicity

1. Introduction

The prolonged life-expectancy and increasing world-population are two factors, among others, influencing the rate of implant surgeries worldwide. Research show that from 2000 to 2010, almost a doubling in the rate of total knee replacements was registered, in the U.S. alone [1]. Today, most joint-implants are standardized and some studies have been conducted on the osseointegration of these [2-6]. Most of these implants are manufactured using massive wrought materials, which have high elastic moduli.

In general, bone has an elastic moduli around 0.2-30 GPa, which is soft compared to common materials used in e.g. hip-implants, e.g. Ti-6Al-4V (110 Gpa), this difference in moduli may be involved in the generation of the stress-shielding phenomena at the basis of osteopenia [7].

A field that is in constant development is the field of additive manufacturing (AM), where intricate components in a variety of materials, including steels and titanium, can be

manufactured using a layer-based approach [8]. Selective laser melting (SLM), is one such AM process. By implementing SLM in the manufacturing of joint-implants, it is possible to manufacture parts with internal structures and lattices, enabling intrinsic mechanical properties resembling those of bony-structures. This approach may support the reduction of stress-shielding onset.

One of the main factors in determining the success of an implant surgery is to which extent the implant undergoes osseointegration. The latter term is here defined as the contact between living bone and implant, as initially phrased by Albrektsson [9]. After an arthroplasty, mesenchymal stem cells (MSCs) migrate to the site of surgery. These cells will, with time, differentiate into osteoblasts and start depositing new osteoid, thus integrating the implant with the surrounding bone [10]. Research show that the implant surface and chemistry plays a major role in the processes associated with MSC adhesion, proliferation and differentiation [11]. When studying

Nomenclature	
ALP	Alkaline phosphatase
AM	Additive manufacturing
BMSC	Bone marrow derived stem cell
FA	Focal adhesions
HBSS	Hank's balanced salt solution
MSC	Mesenchymal stem cell
HS	Human serum
LAL	Limulous amoebocyte lysate
LSM	Laser Scanning Microscope
PBS	Phosphate buffered saline
PFA	Paraformaldehyde
RPMI	Roswell Park Memorial Institute (media)
RT	Room Temperature
SLM	Selective Laser Melting
SS	Stainless steel

the surface chemistry, toxicity is a main factor affecting the survival of the cells near the implant.

Various research has been conducted investigating the connection between surface-roughness and adhesion onto a variety of materials [12-17] and although SLM is capable of producing components to a near-net-shape, some defects and inclusions are inherently present. This influences the surface-topography which ends up being relatively rough, compared to finely machined components.

Given both the geometrical complexities obtainable by SLM and the strong influence of surface topography on the cell processes, a versatile finishing technique is needed. Magneto abrasive finishing (MAF) is one such process, able to surface finish components with complex geometries, to close morphologic tolerances.

Metallic scaffolds in 316L stainless steel (SS) were produced using SLM and the adopted material was tested for toxicity with a limulous amoebocyte lysate (LAL) assay. Different surface roughness values were achieved by MAF and

finally, human bone marrow derived MSCs (BMSCs) were adhered to the scaffolds. The adhesion of the BMSCs was imaged using confocal fluorescence laser scanning microscopy (LSM). A detailed description of the process is given before the toxicity results are presented, followed by an investigative overview of the MAF finished scaffold-surfaces. Lastly, representative results from the adhesion of the BMSCs are given and compared with other literature.

The scope of this paper is to present preliminary results of the work conducted, and the main objective is to lay a foundation for future investigation of these topics.

2. Scaffold preparation and experimental protocol

2.1 Materials

A graphical overview of the SLM process is given in figure 1b. A fine, spherical metallic powder, with grain-distributions varying from 2 μm -150 μm , is distributed onto a build-platform in an inert atmosphere. Subsequently a high-power laser scans the powder layer according to the shape of the component's cross section at the specific layer-height, thus melting and solidifying the powder particles in a melt-pool. A new powder-layer is then distributed and the process starts over, melting a new cross-sectional layer of material on top of the previously solidified layer. The distribution of powder-grain diameters present in the powder secure both good packing characteristics and optimal final material density [18].

All scaffolds used, were manufactured in an M2-Concept SLM printer using 316L stainless steel powder. The machine was equipped with a 180W Nd:YAG laser with a focus area of 150 μm , following a Gaussian distribution of 3 σ . The hatch and scanning speed was set to 105 μm and 800mm/s respectively. Figure 1a depicts the geometry of each of the ten manufactured scaffolds. Out of these ten, two were randomly chosen to be used as control-samples, hence no surface-finishing was conducted on these.

The remaining 8 scaffolds underwent MAF to achieve different surface roughness's. MAF exploits the magnetic

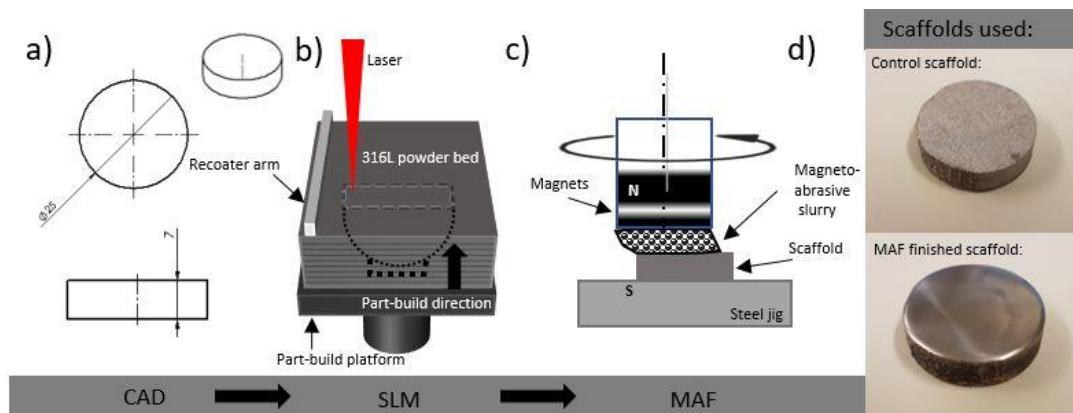


Fig. 1. Scaffold production method, starting with the geometry and dimensions (a), the SLM process (b), MAF method (c) and finally a visual comparison of scaffolds finished using MAF (d).

characteristics of e.g. 316L SS. Rotating magnets, combined with an abrasive slurry containing magnetic particles, are spun over the specimen surface, thus creating an abrasive force, as depicted in figure 1c. Prior to seeding, the scaffolds were cleaned in four steps. The first three steps consisted of three separate 5 min ultrasound baths in distilled water, acetone and 70% ethanol respectively. In the fourth and last step, all scaffolds were autoclaved.

2.2 Toxicity

A LAL assay was performed prior to seeding of the samples, in order to determine whether the material demonstrated toxic tendencies. A sample of the scaffold material was incubated 24h in RPMI at 37°C (5% CO₂), the supernatant from both the well containing the metal sample and a control-well only containing RPMI was subsequently LAL-tested.

2.3 Preparation of cells

BMSCs were cultured in MEM- α with platelet lysate (5%) and heparin (cons). Cells were subsequently cultured at 37°C (5% CO₂). BMSCs were used before passage 7.

2.4 Seeding

In order to ensure a proper seeding-location of the BMSCs, a wax-border was applied along the scaffold edges, as depicted in figure 2, thus avoiding the overflow of cell-suspension over the scaffold edge. After applying the wax border, each scaffold was placed in a well on a 6-well board and BMSCs were seeded onto each scaffold at a concentration of 85.000/ml. Scaffolds with seeded cells were incubated for 48h.

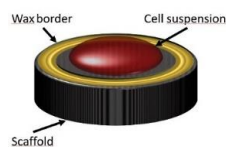


Fig. 2. Scaffold seeding set-up.

2.5 Fixation and staining

Following adhesion of the BMSCs, the medium was removed and the scaffolds were carefully washed two times with phosphate buffered saline (PBS). The cells were subsequently fixated with PFA in PBS (3.7%, 15 min, RT) before the cells were washed with PBS. Next, the cells were permeabilized and blocked in saponin (conc, 10% HS, 10 min, RT). Cells were subsequently washed with PBS before being stained with Phalloidin 488 in PBS (2.5%, 10 min, RT). Lastly, the nuclei were stained with Draq5 633 in PBS (0.1%, 10 min, RT). All staining was performed in the dark.

2.6 Characterization

The roughness of each scaffold was analyzed using a profilometer. In addition, a selection of the scaffolds was further analyzed with an optical profiler.

Images of adhesion were obtained with a Zeiss LSM 510 confocal microscope, using 63X and 10X objectives. The general settings are summarized in table 2. Light-paths used were suitable to the set-up and staining reflection properties. Images obtained in the LSM were further processed and fitted with scalebars using ImageJ software.

Table 2. General settings of LSM confocal microscope.

Lens	63X/1.4			10X/0.45w		
	Plan-Apochromat oil			C-Apochromat water		
	DIC			M27		
Channel	1	2	3	1	2	3
Wavelength [nm]	633	488	458	633	488	458
Power	20.0	6.5	5.0	20.0	6.5	5.0
Pinhole [μ m]	0.8	0.8	0.8	1.1	1.1	1.1
Gain	575	534	362	470	488	523

3. Results and discussion

3.1 The scaffolds were non-toxic

Results from the LAL assay conducted on the 316L metal, as previously described, are shown in table 3. These concentrations are classified as non-toxic, which is in accordance with the wrought 316L steel counterpart.

Table 1. LAL assay results

Well contents:	Endotoxin concentration
316L metal sample and RPMI	0.359 EU/ml
RPMI only	0.212 EU/ml

3.2 Different micro roughness's obtained with MAF

Figure 3a presents an overview on the scaffold roughness's pre- and post-MAF, obtained using a profilometer. The initial Ra is varying from around 7 μ m to around 14 μ m, while the Rz is in the range of 60 μ m-110 μ m. After MAF, both Ra and Rz show a gradient increase steadily from scaffold 1 to 8. The final Ra of scaffold 1-4 is clearly on the sub-micrometer scale, while the remaining four scaffolds display an Ra increase from 1.66 μ m to 12.3 μ m. The final Rz display a similar increase in magnitude, starting off discretely for the first three scaffolds at around 2 μ m, and then ending up at 84.2 μ m for scaffold 8. Scaffolds 1 to 4 are selected for further characterization in an optical profiler due to their surface characteristics. Results from this analysis collaborates the results previously presented.

3.3 Expected variation in adhesion

Two experimental rounds were conducted testing adhesion, the scaffolds used in each round are listed in figure 3c and representative results are presented in figure 4. After 48 h incubation, the BMSC show overall good attachment to the underlying scaffolds on the finer group. Furthermore, the adhesion of cells on these scaffolds seem to be evenly distributed, as shown in the 10X magnification image of scaffold 4. There are no apparent differences in adhesion

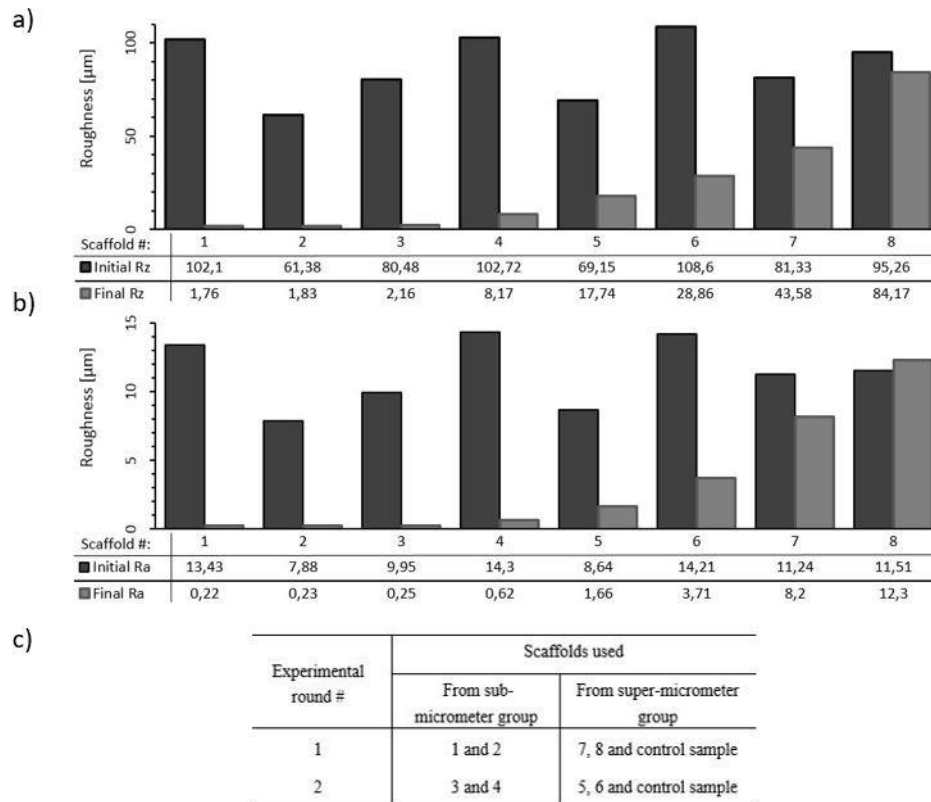


Fig. 3. Results from the MAF process: a) Rz results from the profilometer analysis, b) Ra results from the profilometer analysis, c) distribution of scaffolds between the two test-rounds.

between scaffolds 1 and 2. The surface topography is clearly visible on scaffold 3, here represented as the grayscale channel. The cells seem to be orienting themselves with underlying topography, which is in accordance with reviewed literature [12].

Comparing the scaffolds from the finer group to the rougher scaffolds (6-8), cells seem not to be as uniformly distributed. The BMSCs tend to adhere inside the larger topographic groves, easily observable on scaffold 7. Takeda et. al. [16], found 1 μm topographies to be ideal for adhesion of rat phenochromocytoma (PC12), which seem to resonate well with

other work performed with hMSCs on bone-specific activity. For differentiation into osteoblast, Faia-Torres et. al. [14] found the ideal surface topography having Ra between 0.93 μm - 2.1 μm and Rz between 71 μm -135 μm . Dalby et. al. [13] and Fiedler et. al. [15], investigated the limits of the sensing capabilities of MSC filopodia, which seem to be in the range of 35nm, well below the roughness of the smoothest scaffold used in this work. Anyhow, it's worth mentioning the work of Kolind et. al. [17], which supports the previously mentioned work regarding proliferation and differentiation, but couldn't

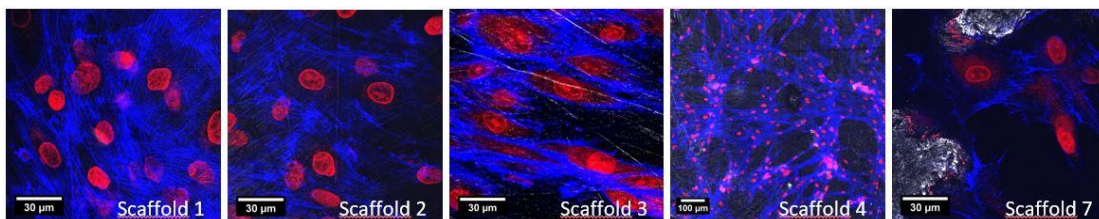


Fig. 4. Representative adhesion results. Scaffold 1 imaged at 63X, scaffold 2 imaged at 63X, scaffold 3 imaged at 63X, scaffold 4 imaged at 10X and finally, scaffold 7 imaged at 63X

identify any connection between adhesion and surface roughness.

3.4 Future work

As presented in this study, AM 316L scaffolds seem to be well suited to support adhesion of BMSCs. The scaffolds are produced in an inert atmosphere and should thereby not contain more toxic alloying elements than its wrought counterpart. More work on this topic will nonetheless be beneficial.

Steels usually present some issues with respect to corrosion, hence to this date, 316L is mostly being used in short-term implants [19]. But, since SLM material result in different microstructural properties compared to wrought material, a study on the corrosion behavior in-vitro may be worth conducting, to ascertain whether AM 316L is suitable for long-term implant use.

Further, more tests are needed to obtain conclusive quantifiable results regarding adhesion, e.g. staining for focal adhesions (FA). Proliferation tests and differentiation analysis are also important topics to study in future works on this material.

3.5 Summary

In this study, scaffolds were manufactured by SLM using a widely used biomedical material, 316L stainless steel. The material was tested for toxicity, yielding negative results.

Different surface gradients were generated onto each scaffold using MAF. As the results are expressing, this process seems to be highly versatile and well suited for the surface finishing of implants.

BMSCs were adhered onto the scaffolds. The results obtained were generally expected and for the most part supported by reviewed literature. In general, a more comprehensive test both investigating proliferation and differentiation as well as adhesion, is needed to ascertain the potential of additively manufactured steel.

Acknowledgements

References

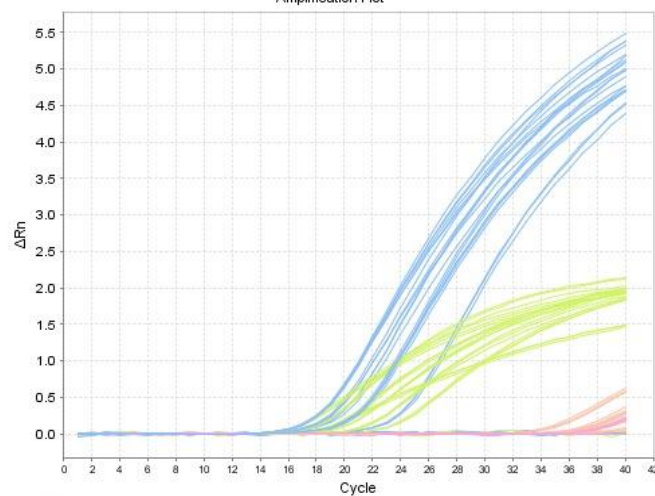
- Williams SN, W.M., Bercovitz A. , *Hospitalization for Total Knee Replacement Among Inpatients Aged 45 and Over: United States, 2000–2010*. NCHS Data Brief, U.S. DEPARTMENT OF HEALTH & HUMAN SERVICES, 2015(210).
- Liu, X., P.K. Chu, and C. Ding, *Surface modification of titanium, titanium alloys, and related materials for biomedical applications*. Materials Science and Engineering: R: Reports, 2004. **47**(3–4): p. 49-121.
- Liu, C., et al., *In vitro corrosion behavior of multilayered Ti/TiN coating on biomedical AISI 316L stainless steel*. Surface and Coatings Technology, 2006. **200**(12–13): p. 4011-4016.
- Nouri, A. and C. Wen, *1 - Introduction to surface coating and modification for metallic biomaterials*, in *Surface Coating and Modification of Metallic Biomaterials*. 2015, Woodhead Publishing. p. 3-60.
- Oshida, Y., *7 - Implant-Related Biological Reactions*, in *Bioscience and Bioengineering of Titanium Materials (Second Edition)*. 2013, Elsevier: Oxford. p. 169-223.
- Singh, S.K., et al., *3rd International Conference on Materials Processing and Characterisation (ICMPC 2014) Surface Modifications of Titanium Materials for developing Corrosion Behavior in Human Body Environment: A Review*. Procedia Materials Science, 2014. **6**: p. 1610-1618.
- Wang, X., et al., *Topological design and additive manufacturing of porous metals for bone scaffolds and orthopaedic implants: A review*. Biomaterials, 2016. **83**: p. 127-141.
- Murr, L.E., *Frontiers of 3D Printing/Additive Manufacturing: from Human Organs to Aircraft Fabrication?*. Journal of Materials Science & Technology, 2016. **32**(10): p. 987-995.
- Albrektsson, T. and C. Johansson, *Osteoinduction, osteoconduction and osseointegration*. European Spine Journal, 2001. **10**(SUPPL. 2): p. S96-S101.
- Naddeo, P., et al., *Surface biocompatibility of differently textured titanium implants with mesenchymal stem cells*. Dental Materials, 2015. **31**(3): p. 235-243.
- Wozniak, M.A., et al., *Focal adhesion regulation of cell behavior*. Biochimica et Biophysica Acta (BBA) - Molecular Cell Research, 2004. **1692**(2–3): p. 103-119.
- Abagnale, G., et al., *Surface topography enhances differentiation of mesenchymal stem cells towards osteogenic and adipogenic lineages*. Biomaterials, 2015. **61**: p. 316-326.
- Dalby, M.J., N. Gadegaard, and R.O.C. Oreffo, *Harnessing nanotopography and integrin-matrix interactions to influence stem cell fate*. Nat Mater, 2014. **13**(6): p. 558-569.
- Faia-Torres, A.B., et al., *Osteogenic differentiation of human mesenchymal stem cells in the absence of osteogenic supplements: A surface-roughness gradient study*. Acta Biomaterialia, 2015. **28**: p. 64-75.
- Fiedler, J., et al., *The effect of substrate surface nanotopography on the behavior of multipotent mesenchymal stromal cells and osteoblasts*. Biomaterials, 2013. **34**(35): p. 8851-8859.
- Takeda, I., M. Kawanabe, and A. Kaneko, *An investigation of cell adhesion and growth on micro/nano-scale structured surface—Self-assembled micro particles as a scaffold*. Precision Engineering, 2016. **43**: p. 294-298.
- Kolind, K., et al., *Control of proliferation and osteogenic differentiation of human dental-pulp-derived stem cells by distinct surface structures*. Acta Biomaterialia, 2014. **10**(2): p. 641-650.
- Herzog, D., et al., *Additive manufacturing of metals*. Acta Materialia, 2016. **117**: p. 371-392.
- Chen, Q. and G.A. Thouas, *Metallic implant biomaterials*. Materials Science and Engineering: R: Reports, 2015. **87**: p. 1-57.

Appendix B - Procedures and extra forms

.4 PCR amplification and run-outs

During PCR amplification of the cDNA, amplification curves are obtained from the tested samples. The x-axis represent the number of cycles, while the curves represent the expression of the researched genes. The further out on the x-axis the curve rises, the more amplification used to obtain an expression. Once the expression of a target gene is rising, the cycle number is recorded and is given a Ct value (table). During the PCR analysis our set-up performed 40 amplification cycles. However if a gene is expressed after 35.5 cycles, the possibility arises that the measured signal is generated by other compounds in solution. Hence, only measurements expressed before Ct 35.5 are used in the PCR graphs in chapter 4.

Well	Sample Name	Target Name	RQ	RQ Min	RQ Max	Ct	Ct Mean	Ct SD
D1	BMSC D0	Osterix	0,64	0,37	1,08	35,98	36,52	0,77
D2	GM D7 2D	Osterix	5,31	2,50	11,26	35,27	34,51	1,08
D3	OM D7 2D	Osterix	48,86	29,26	81,61	31,90	31,38	0,74
D4	GM D7 3D	Osterix	7,56	6,52	8,76	33,98	33,84	0,21
D5	OM D7 3D	Osterix	1,00	0,76	1,31	35,10	34,83	0,39
D6	GM D14 2D	Osterix	18,35	14,80	22,74	32,28	32,50	0,31



.5 Automatically generated FEA report of static compression analysis.

Figure colours disappeared during export due to some technical issues with the software. For detailed model figure, please refer to subsection 4.1.2.



Description

No Data

Simulation of cube lattice cubic7x7

Date: mandag 5. juni 2017
Designer: Solidworks
Study name: Static 3
Analysis type: Static

Table of Contents

Description	1
Assumptions	2
Model Information	2
Study Properties	3
Units	4
Material Properties	4
Loads and Fixtures.....	5
Connector Definitions.....	5
Contact Information.....	6
Mesh information	7
Sensor Details	8
Resultant Forces	8
Beams.....	9
Study Results	10
Conclusion	14



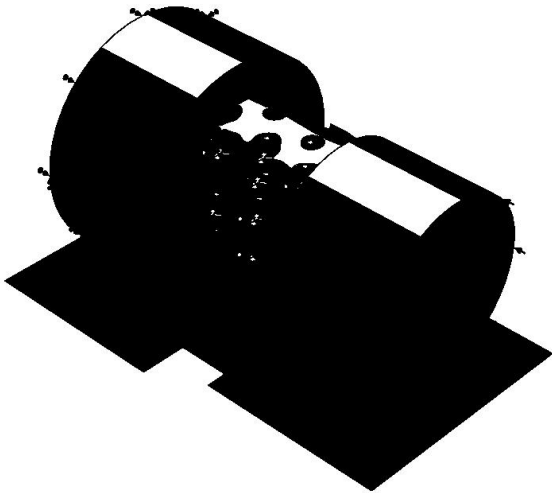
SOLIDWORKS

Analyzed with SOLIDWORKS Simulation

Simulation of cube lattice cubic7x7 1

Assumptions

Model Information



A 3D CAD model of a cube lattice structure, rendered in black. The model consists of a central cube with a lattice of smaller cubes attached to its faces. The model is shown in a perspective view, tilted to show its three-dimensional structure. A small coordinate system icon is visible in the bottom left corner of the model area.

Model name: cube lattice cubic7x7
Current Configuration: Default

Solid Bodies			
Document Name and Reference	Treated As	Volumetric Properties	Document Path/Date Modified

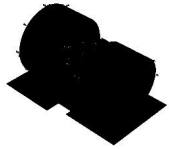


SOLIDWORKS

Analyzed with SOLIDWORKS Simulation

Simulation of cube lattice cubic7x7

2

<p>Boss-Extrude2</p> 	<p>Solid Body</p>	<p>Mass:0.00296342 kg Volume:6.69127e-007 m³ Density:4428.78 kg/m³ Weight:0.0290415 N</p>	<p>C:\Users\Timothy\Desktop \cube lattice cubic7x7.SLDPRT Jun 05 13:17:00 2017</p>
--	-------------------	--	---

Study Properties

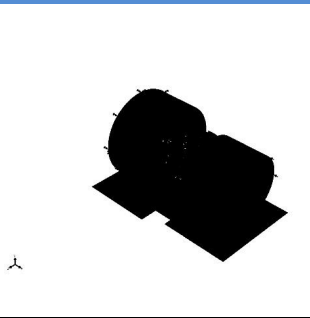
Study name	Static 3
Analysis type	Static
Mesh type	Solid Mesh
Thermal Effect:	On
Thermal option	Include temperature loads
Zero strain temperature	298 Kelvin
Include fluid pressure effects from SOLIDWORKS Flow Simulation	Off
Solver type	FFEPlus
Inplane Effect:	Off
Soft Spring:	Off
Inertial Relief:	Off
Incompatible bonding options	Automatic
Large displacement	Off
Compute free body forces	On
Friction	Off
Use Adaptive Method:	Off
Result folder	SOLIDWORKS document (C:\Users\Timothy\Desktop)



Units

Unit system:	SI (MKS)
Length/Displacement	mm
Temperature	Kelvin
Angular velocity	Rad/sec
Pressure/Stress	N/m ²

Material Properties

Model Reference	Properties	Components
	<p>Name: Ti-6Al-4VSolution treated and aged (SS)</p> <p>Model type: Linear Elastic Isotropic</p> <p>Default failure criterion: Max von Mises Stress</p> <p>Yield strength: 8.27371e+008 N/m²</p> <p>Tensile strength: 1.05e+009 N/m²</p> <p>Elastic modulus: 1.048e+011 N/m²</p> <p>Poisson's ratio: 0.31</p> <p>Mass density: 4428.78 kg/m³</p> <p>Shear modulus: 4.10238e+010 N/m²</p> <p>Thermal expansion coefficient: 9e-006 /Kelvin</p>	SolidBody 1(Boss-Extrude2)(cube lattice cubic7x7)
Curve Data:N/A		



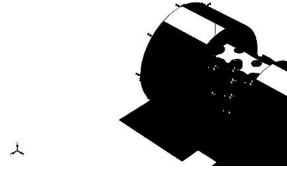

SOLIDWORKS

Analyzed with SOLIDWORKS Simulation

Simulation of cube lattice cubic7x7

4

Loads and Fixtures

Fixture name	Fixture Image	Fixture Details		
Fixed-1		Entities: 1 face(s) Type: Fixed Geometry		
Resultant Forces				
Components	X	Y	Z	Resultant
Reaction force(N)	930.248	2.26498e-006	2.92063e-006	930.248
Reaction Moment(N.m)	0	0	0	0
Reference Geometry-1		Entities: 1 face(s) Type: Use reference geometry Translation: ---, ---, -0.01 Units: mm		
Resultant Forces				
Components	X	Y	Z	Resultant
Reaction force(N)	-930.248	0	0	930.248
Reaction Moment(N.m)	0	0	0	0

Connector Definitions

No Data



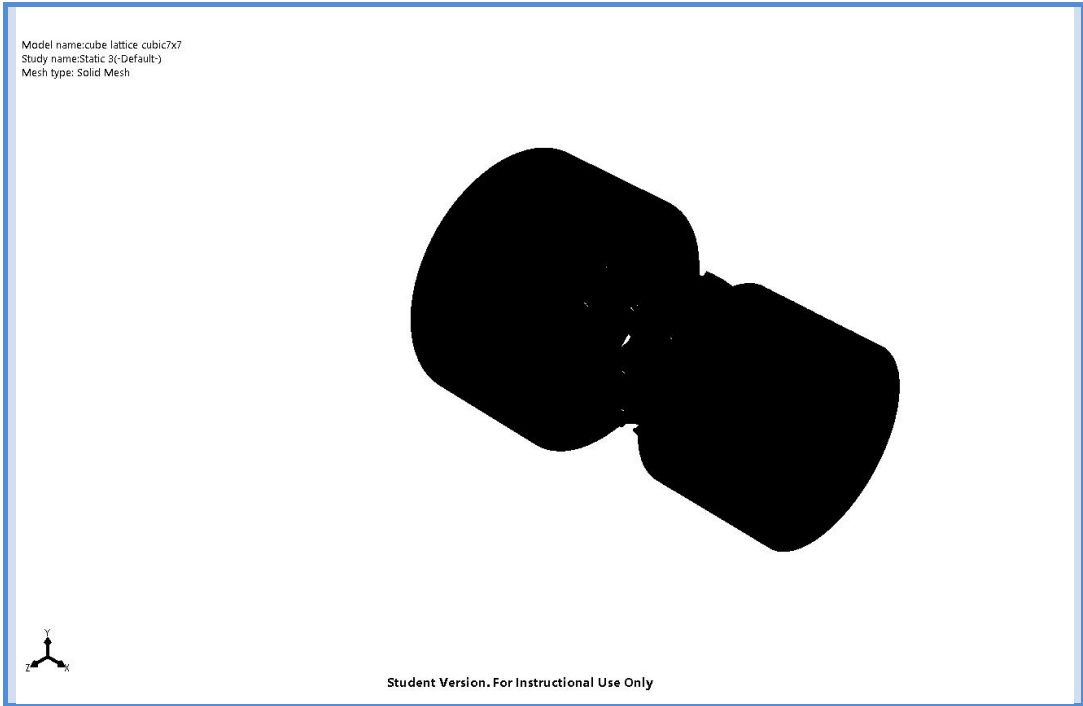
Mesh information

Mesh type	Solid Mesh
Mesher Used:	Standard mesh
Automatic Transition:	Off
Include Mesh Auto Loops:	Off
Jacobian points	4 Points
Element Size	0.875069 mm
Tolerance	0.0437534 mm
Mesh Quality	High

Mesh information - Details

Total Nodes	76057
Total Elements	48922
Maximum Aspect Ratio	2439.9
% of elements with Aspect Ratio < 3	88.6
% of elements with Aspect Ratio > 10	0.352
% of distorted elements(Jacobian)	0
Time to complete mesh(hh:mm:ss):	00:00:50
Computer name:	





Sensor Details

No Data

Resultant Forces

Reaction forces

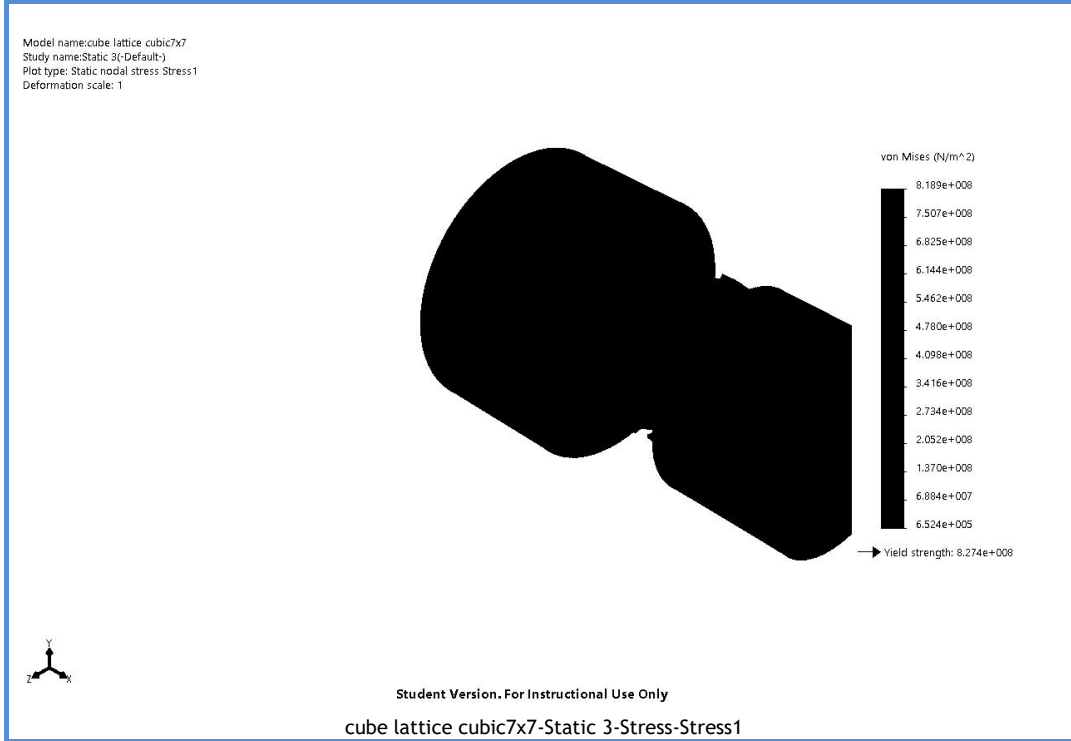
Selection set	Units	Sum X	Sum Y	Sum Z	Resultant
Entire Model	N	-0.000122547	2.26498e-006	2.92063e-006	0.000122603

Reaction Moments

Selection set	Units	Sum X	Sum Y	Sum Z	Resultant
Entire Model	N.m	0	0	0	0

Study Results

Name	Type	Min	Max
Stress1	VON: von Mises Stress	652394 N/m ² Node: 5041	8.18923e+008 N/m ² Node: 75921



Name	Type	Min	Max
Displacement1	URES: Resultant Displacement	0 mm Node: 145	0.0100555 mm Node: 73973



SOLIDWORKS

Analyzed with SOLIDWORKS Simulation

Simulation of cube lattice cubic7x7 10

.6 Risk assessment

NTNU		Kartlegging av risikofylt aktivitet		Utarbeidet av		Nummer		Dato	
				HMS-avd.		HMSRV2601		22.03.2011	
				Godkjent av				Erstatter	
				Rektor				01.12.2006	

Dato: 13.03.2017

Enhet: Institutt for produktutvikling og materialer og Institutt for kreftforskning og molekylær medisin

Linjeleder: Torgeir Welo Deltakere ved kartleggingen:

Jan Torgersen (veileder, MTP)

Marita Westhrin (medveileder, IKM)

Therese Standal (Kontakt- og kompetanseperson, IKM)

Timothy Jørholm (Masterstudent)

Kort beskrivelse av hovedaktivitet/hovedprosess: Masteroppgave, student Timothy Jørholm. «Osteoinduction vs ingrowth of bMSCs on additive manufactured Ti Alloys». Er oppgaven rent teoretisk? (JANEI): NEI

Signaturer: Ansvarlig veileder:

Jan Torgersen

Student: Timothy Jørholm

ID nr.	Aktivitet/prosess	Ansvarlig	Eksisterende dokumentasjon	Eksisterende sikringstiltak	Lov, forskrift o.l.	Kommentar
14563	ELISA	Berit Fladvad Størdal	Avvik.ntnu.no	Ansatte bruker frakk og hansker, og vernebriller ved tilsetning av svovelsyra. Svovelsyra og TMB-substratet tilsettes i avtrekk. Platevaskeren brukes til vask av elisabrettene, og dette er et lukket system under vasking. Ansatte får opplæring i prosedyren. Bruk av frakk og vernebriller. Prosedyren utføres i avtrekkskap med forsikthet. Samt opplæring i prosedyren		
1.1	Para form Aldehyd (PFA) til fiksering av celler	Therese Standal	Not found			

NTNU		Utarbeidet av		Nummer		Dato	
		HMS-avd.		HMSRV2601		22.03.2011	
HMS		Godkjent av		Erstatter			
		Rektor				01.12.2006	

Risikovurdering

Dato: 13.03.2017

Enhet: Institutt for produktutvikling og materialer og Institutt for kreftforskning og molekylær medisin

Linjeleder: Torgeir Welo Deltakere ved kartleggingen:

Jan Torgersen (veileder, MTP)
 Marita Westrin (medveileder, IKM)
 Therese Standal (Kontakt- og kompetanseperson, IKM)
 Timothy Jørholm (Masterstudent)

Kort beskrivelse av hovedaktivitet/hovedprosess: Masteroppgave, student Timothy Jørholm. «Osteoinduction vs ingrowth of bMSCs on additive manufactured Ti Alloys». Er oppgaven rent teoretisk? (JA/NEI): NEI

Signaturer: Ansvarlig veileder: 

Student: 

ID nr	Aktivitet fra kartleggings-skjemaet	Mulig uønsket hendelse/belastning	Vurdering av sannsynlighet (1-5)	Vurdering av konsekvens:				Risiko-Verdi (menneske)	Kommentarer/status Forslag til tiltak
				Menneske (A-E)	Ytre miljø (A-E)	Øk/ materiel (A-E)	Om-dømme (A-E)		
14563	ELISA	Fortynning av konsentrert svovelsyre til 1M	3	B	-	A	A	B3	Bruk av vernebriller og frakk
14563	ELISA	Uønsket hendelse svovelsyre	3	B	-	A	A	B3	Bruk av vernebriller og frakk
1.1	PFA for fiksering av celler	Uønsket hendelse PFA	2	D	-	A	B	D1	Bruk av vernebriller, frakk og avtrekkskap

NTNU		Utarbeidet av		Dato	
 HMS		HMS-avd.		22.03.2011	
		Godkjent av		Erstatter	
		Rektor		01.12.2006	
Risikovurdering					
					

Sannsynlighet vurderes etter følgende kriterier:

Svært liten 1	Liten 2	Middels 3	Stor 4	Svært stor 5
1 gang pr 50 år eller sjeldnere	1 gang pr 10 år eller sjeldnere	1 gang pr år eller sjeldnere	1 gang pr måned eller sjeldnere	Skjer ukentlig

Konsekvens vurderes etter følgende kriterier:

Gradering	Menneske	Ytre miljø Vann, jord og luft	Øk/materiell	Omdømme
E Svært Alvorlig	Død	Svært langvarig og ikke reversibel skade	Drifts- eller aktivitetstans > 1 år.	Troverdighet og respekt betydelig og varig svekket
D Alvorlig	Alvorlig personskade. Mulig uføret.	Langvarig skade. Lang restitusjonstid	Driftstans > ½ år Aktivitetstans i opp til 1 år	Troverdighet og respekt betydelig svekket
C Moderat	Alvorlig personskade.	Mindre skade og lang restitusjonstid	Drifts- eller aktivitetstans < 1 mnd	Troverdighet og respekt svekket
B Liten	Skade som krever medisinsk behandling	Mindre skade og kort restitusjonstid	Drifts- eller aktivitetstans < 1 uke	Negativ påvirkning på troverdighet og respekt
A Svært liten	Skade som krever førstehjelp	Ubetydelig skade og kort restitusjonstid	Drifts- eller aktivitetstans < 1 dag	Liten påvirkning på troverdighet og respekt

Risikoverdi = Sannsynlighet x Konsekvens

Beregn risikoverdi for Menneske. Enheten vurderer selv om de i tillegg vil beregne risikoverdi for Ytre miljø, Økonomi/materiell og Omdømme. I så fall beregnes disse hver for seg.

Til kolonnen "Kommentarer/status, forslag til forebyggende og korrigerende tiltak":

Tiltak kan påvirke både sannsynlighet og konsekvens. Prioriter tiltak som kan forhindre at hendelsen inntreffer, dvs. sannsynlighetsreducerende tiltak foran skjærpet beredskap, dvs. konsekvensreducerende tiltak.




NTNU		Risikomatrixe		Dato	
				08.03.2010	
		utarbeidet av		Nummer	
		HMS-avd.		HMSRV2604	
		godkjent av		Erstatter	
		Rektor		09.02.2010	



MATRISSE FOR RISIKOVURDERINGER ved NTNU

KONSEKVENSENS		Svært alvorlig	E1	E2	E3	E4	E5
		Alvorlig	D1	D2	D3	D4	D5
	Moderat	C1	C2	C3	C4	C5	
	Liten	B1	B2	B3	B4	B5	
	Svært liten	A1	A2	A3	A4	A5	
		Svært liten	Liten	Middels	Stor	Svært stor	
SANNSYNLIGHET							

Prinsipp over akseptkriterium. Forklaring av fargene som er brukt i risikomatrixen.

Farge	Beskrivelse
	Uakseptabel risiko. Tiltak skal gjennomføres for å redusere risikoen.
	Vurderingsområde. Tiltak skal vurderes.
	Akseptabel risiko. Tiltak kan vurderes ut fra andre hensyn.